UNIVERSITAT POLITÈCNICA DE CATALUNYA
BARCELONATECH
Escola d'Enginyeria de Telecomunicació
i Aeroespacial de Castelldefels

UCI Samueli School of Engineering
Department of Mechanical and Aerospace Engineering

Bachelor's Degree in Air Navigation Engineering
Final Thesis

Novel airplane roll mechanism implementation in a wind tunnel

University *of* California, Irvine

Jordi Ventura Siches

Advisors: Haithem E. Taha (UCI),
Eduard Bertran (UPC)

July 17, 2019

Abstract

Key words: wind tunnel testing, geometric nonlinear control, LIBRA mechanism

- ENGLISH -

According to recent research conducted by professor Haithem E. Taha and Ahmed M. Hasan, there is a loss in the control capabilities of the ailerons when flying at stall regime. Not only the sensitivity of this control surface decreases in its ability to generate roll moment but it produces the opposite effect, making the aircraft unpredictable. In order to overcome this situation, an unconventional method, called LIBRA, has been devised, involving geometric nonlinear control tools such as Lie brackets. In the numerical simulations, this mechanism would generate up to 4 times more rolling moment than the conventional procedure.

The first stage of the experimental research on the LIBRA mechanism consists of finding out the aerodynamic characteristics of a small-scaled aircraft model in which the mechanism will be implemented as well as determining if there really exists a loss in the control capabilities when flying at stall. This experiments will be performed in a wind tunnel and both the forces and moments acting on an aircraft will have to be measured.

Currently there exist in the market multi-axis load cells that can measure moments and forces in all directions. However, they have fixed capacities and they are very expensive and delicate. One of the main goals of this thesis will be the design and manufacturing of a modular load cell system able to measure forces and moments in four different axis.

Besides, the unconventional method will be thoroughly described from a differential geometry perspective. Finally, by means of the 4-axis load cell system, forces and moments will be measured in different control configurations at stall, in order to test the rolling generating capabilities of the ailerons.

- CATALÀ -

Segons un estudi recent dut a terme pel professor Haithem E. Taha i Ahmed M. Hasan, es perd la capacitat de control en els alerons quan l'avió entra en règim de pèrdues. No només la sensibilitat d'aquesta superfície de control decreix en la seva habilitat de generar moment de balanç sinó que a més arriba a produir l'efecte contrari al desitjat, convertint el comportament de l'aeronau en impredictible. Per tal de fer front a aquest problema, un mètode nou, anomenat LIBRA, ha estat ideat, utilitzant eines del control geomètric no lineal com el producte de Lie. En les simulacions numèriques, aquest mecanisme genera fins a 4 cops més moment de balanç que el procediment convencional.

La primera fase de la recerca experimental del mètode LIBRA consisteix a trobar les característiques aerodinàmiques d'un model d'aeronau a petita escala en el qual s'implementarà el mecanisme, així com determinar si realment hi ha una pèrdua en el control. L'experiment es farà en un túnel de vent i tant les forces com els moments que actuen en una aeronau hauran de ser mesurats.

Actualment, existeixen en el mercat galgues extensiomètriques multi-axials capaces de mesurar forces i moments en totes direccions. Tanmateix, tenen capacitats fixades i són molt cares i delicades. Un dels principals objectius d'aquest treball és dissenyar i fabricar un sistema de sensors que pugui mesurar forces i moments en quatre eixos diferents.

A més, el nou mètode serà descrit en detall des de la perspectiva de la geometria diferencial. Finalment, fent ús del sistema de galgues extensiomètriques, es mesuraran les diferents forces i moments en diferents configuracions de control en un avió volant en pèrdues, per tal d'avaluar la capacitat de generar moment de balanç dels alerons.

Acknowledgements

First of all, I'd like to thank very much professor Haithem E. Taha for having given me the opportunity of working in his lab. Attending his lectures has not only allowed me to learn fascinating concepts about geometric nonlinear control, but has also inspired me to continue my graduate studies. Also, I appreciate a lot having met Moatasem Fouda, that has been a source of practical knowledge during the last months as well as a good friend. I would like to thank the work of the rest of undergraduate students that have taken part in this project as well, particularly of Mahmoud Rashad.

This project wouldn't have been possible without the economic support of the Balsells Fellowship. I'd like to acknowledge this gratitude to all the people that have worked to make it possible, and specially to professor Roger Rangel.

A special mention goes to my friends. From the one hand, the rest of Balsells fellows from Irvine who, during these months, have shared lunch with me as well as very interesting discussions and some roadtrips. On the other hand, to my friends in Barcelona, that I've missed very much.

Last, but not least, I have to thank my family for all the support they have been giving me since the very beginning of my studies, they've always trusted me and given me strength. Also, to my American relatives from San Diego and Phoenix, with whom I've had the chance to share some weekends of leisure and fun. *Thank you all!*

Contents

List of Figures

List of Tables

Chapter 1

Introduction

1.1 Mission statement and objectives

Almost half of all loss of control events in commercial aircraft occur at stall, when the aileron sensitivity decreases dramatically. This is the starting point of the late research conducted by professor Haithem E. Taha and Ahmed M. Hassan concerning an unconventional roll mechanism at this flight regime. Their approach is based on nonlinear motion planning and uses differential geometry and Lie algebra to reach what they have called the LIBRA mechanism, that has been proven to generate four times more roll than the conventional constant aileron deflection, in numerical simulations.

This novel mechanism works theoretically, but has never been applied experimentally, as it requires both the ailerons and the elevators to deflect following high frequency oscillations. The present thesis concerns the first stages of the experimental part of the LIBRA mechanism research, and aims to show whether or not this tool would significantly improve the control capabilities of an aircraft flying at stall. Within the experimental part, the following phases have been devised:

- Phase 1: measurement of lift and drag forces and pitch and roll moments of a small-scaled aircraft at positive stall in the wind tunnel as well as measurement of aileron sensitivity for the same range of angles of attack using the conventional deflection mechanism.
- Phase 2: measurement of aileron sensitivity using the LIBRA mechanism for the same aircraft and range in the wind tunnel.
- Phase 3: measurement of aileron sensitivity using the LIBRA mechanism in a regular life-size aircraft.

Unfortunately, the present thesis only covers Phase 1, as this project has only been conducted for six months. Phases 2 and 3 will be discussed in the section concerning future work of the conclusions. The main objectives of this work can be summarized in the following points:

1. Design, fabrication an assembly of a modular 4-axis load cell system, that will be used to measure the two forces and two moments in Phase 1.
2. Development of the LabView interface that will monitor the measurements and will compute forces and moments, as well as taring and calibration of the load cell system.
3. Obtainment and discussion of experimental results to show whether there is or not a loss of the control capabilities when flying at stall.

1.2 Project scope

Currently, there exist multi-axis load cell systems that are able to measure forces and moments in all three axes. However, they are very expensive and have a particular capacity and sensitivity which is fixed and, when submitted to excessive stresses, they stop working properly in all directions.

One of the motivations of the present thesis is to design and catalogue an integrated multi-axis load cell system, able to measure forces and moments in different directions and with adjustable capacities. To this end, several aspects regarding manufacturing techniques and material characteristics will be considered.

In order to be able to measure the different forces acting on an aircraft, some key aspects of flight dynamics will be reviewed. Besides, a simple mathematical model will be built in order to convert the load cell reading into

aerodynamic forces and moments, taking into consideration all the correction that will be made. The display of the readings and the different signals processing will also be part of the work.

Finally, in order to measure the role of the control surfaces of an airplane, we will make us of a small-scaled aircraft model that can deflect its ailerons and elevators. Such model has already been designed, and its manufacturing and testing will also be part of this project.

1.3 Project structure

This project is divided into three main parts: the theoretical framework, the practical framework and the discussion of results. An appendix is included to compliment the previous chapters. The theoretical framework presents the main aspects of control theory, differential geometry and flight dynamics that are needed to have a good understanding of the LIBRA mechanism, which is also thoroughly discussed. The results of the simulations are also presented.

The practical framework consists of two main topics: the design, fabrication and assembly of the modular 4-axis load cell system and the development of the interface for the obtainment of results, as well as a description of the taring and calibration processes.

In the third part, the results obtained in the wind tunnel are presented and discussed, and the conclusions reached are explained along with an analysis of the future work to be done.

Finally, the last part concerns aspects that compliment the rest of the thesis. Either they are not strictly related to the topic itself, or they are just examples of issues that are discussed in the text. Additionally, screen-shots of the software used, mathematical expansions and code are presented in this section.

Part I

Theoretical framework

Chapter 2

Fundamentals of Control Theory

In this first section of the theoretical framework, we will introduce basic concepts about Control Theory, focusing in the modern State Space Analysis and Geometric Control, in order to better describe the performance and the mathematical background of the novel roll mechanism that will be tested experimentally. But let's start putting the discipline in context.

2.1 History

It could be argued that the history of Control Theory started many centuries ago. The *harpenodaptai* as a construction tool in the Egypt of pharaohs and pyramids or the irrigation systems used in the ancient Mesopotamia are good examples of the use of control concepts in the earliest known civilizations. Throughout years, more and more complex mathematical developments helped giving shape to the field. Works by C. Huygens and R. Hooke at the end of the XVII Century on the oscillations of the pendulum are also remarkable.

There is a certain consensus, however, that it was not until the publication of the work by J. C. Maxwell on the centrifugal governors that the birth of Control Theory really took place. This device, invented by the Dutch astronomer C. Huygens and developed by the Scottish engineer J. Watt, consisted of a sensor that provides a parameter - usually mechanical displacement- that is function of a given angular velocity. In steam engines, when a threshold angular velocity was exceeded, the moving mechanism would open valves enabling the vapor to escape. This would cause a decrease in the pressure inside the boiler reducing, thus, velocity. The purpose of this gadget is, as it has been shown, to keep velocity as close as possible to a reference value.

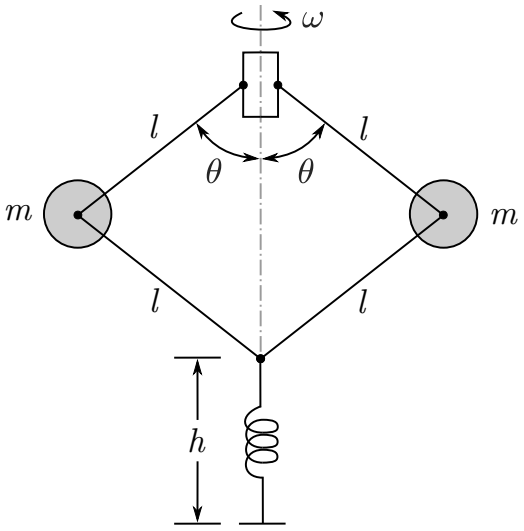

Figure 2.1: Schematic diagram of a centrifugal governor

This simple mechanism is perhaps the best example of proportional control, a type of linear feedback control system in which the correction applied to the controlled variable (velocity, in this case) is proportional to the difference between the desired value (the reference velocity) and the measured one.

Progress in fields like aviation and electronics lead to important progresses in automatic control in the 1930's. By that time, there were two different mathematical approaches emerging: one using differential equations and the other based on frequency analysis. During the Second World War, Control Theory became an important field, due to its military applications. However, it was not until the sixties that it was evidenced the obsolescence of what would be called "classical Control Theory" in a world of nonlinearities and noise. The contributions by R. Kalman in filtering techniques and R. Bellman in dynamic programming were essential in the early development of modern Control Theory.

From classic methods such as the root locus or the transfer function, that were based on a simple-input-simple-

output description of the system and allowed only limited control; the modern theory introduced the state-space representation for linear and time invariant (LTI) systems or the use of Lie algebra in the control of nonlinear systems, to name but a few. It is within the framework of this last mathematical tool that the present paper focuses in: geometric control theory in the analysis of nonlinear controllability of dynamical systems. In the following sections of this chapter, the essential concepts of geometric control will be introduced, so as to describe the how the roll mechanism works.

2.2 Classical control theory

Classical Control Theory (CCT from now on) is based on single-input-single-output dynamic systems and the use of feedback control. In order to analyze such systems, a frequency-domain approach is conducted, for which the contributions of Pierre-Simon de Laplace, Joseph Fourier and Augustin Louis Cauchy at the end of the 18th century were essential.

2.2.1 Laplace transform

The main mathematical tool used in CCT is the Laplace transform, which is defined as:

$$F(s) = \int_0^\infty e^{-st} f(t)\, dt \tag{2.1}$$

where $s = \sigma + i\omega$ is a complex number frequency parameter, with σ and ω real numbers. The Laplace transform is used in CCT to model both the signals and the behaviour of the system. Its main advantage is that, by the use of the property:

$$f(t) \leftrightarrow \mathcal{F}(s) \qquad\qquad f'(t) \leftrightarrow s\,\mathcal{F}(s) + f(0) \tag{2.2}$$

and in general:

$$f^{(n)}(t) \leftrightarrow s^n\,\mathcal{F}(s) - \sum_{k=1}^{n} s^{n-k} f^{(k-1)}(0) = s^n\,\mathcal{F}(s) \qquad \Big(\text{assuming: } f^{(i)}(0) = 0,\ \forall i \in [1,\, n]\Big) \tag{2.3}$$

an arbitrary order ordinary differential equation can be transformed to a simple algebraic equation of the same order. This is specially useful considering that the relations used to describe a system (also called a *plant* in CCT) are often equations of this type.

2.2.2 Transfer functions

Given an input signal in the Laplace frequency domain $X(s) = \mathcal{L}\{X(t)\}$, the transfer function of a given system $G(s)$ is defined as:

$$G(s) = \frac{Y(s)}{X(s)} \qquad \rightarrow \qquad Y(s) = G(s) \cdot X(s) \tag{2.4}$$

being $Y(s) = \mathcal{L}\{Y(t)\}$ the output of the system. As it is shown, in the Laplace domain the output $Y(s)$ is directly the product of the input signal $X(s)$ with the transfer function $G(s)$. Usually, the transfer function has the form of a fraction of polynomials:

$$G(s) = \frac{a_n s^n + a_{n-1} s^{n-1} + \cdots + a_1 s + a_0}{s^m + b_{m-1} s^{m-1} + \cdots + b_1 s + b_0} = \frac{N(s)}{D(s)} \tag{2.5}$$

for which the roots of $N(s)$ are called the zeros of the transfer function and the roots of $D(s)$ are the poles. The poles determine the stability, speed and oscillations of the system temporal response, meanwhile the zeros, together with the poles and the gain factor, only determine the exact final value of the response. The order of the system is the degree of $D(s)$ or m, while the relative order is the degree of $D(s)$ minus the degree of $N(s)$: $m - n$. For a system to be causal -or feasible- its relative order must be positive (strictly causal) or (a somehow problematic case for continuous time) zero.

In general, there are two types of control: open loop and closed loop. In the former, the control is independent of the output, while in the latter the control is built upon feedback of the process variable. Figure 2.2 shows the

classical block diagram of a negative feedback controlled system, in which the output is sensed and compared to a reference value to adjust the control signal.

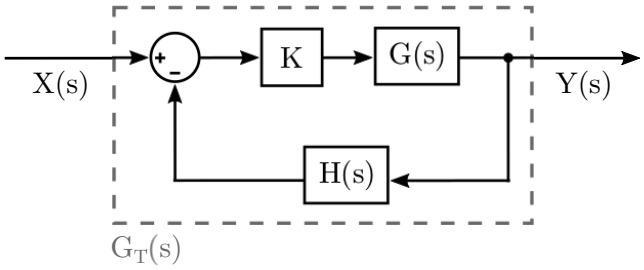

Figure 2.2: Block diagram of system that uses negative feedback

The resulting transfer function of the feedback controller $G_T(s)$ is:

$$G_T(s) = \frac{Y(s)}{X(s)} = \frac{K\,G(s)}{1 + K\,G(s)\,H(s)} \tag{2.6}$$

The value of K will be essential in the behaviour and stability of the feedback system. In order to study the effect of this parameter, the tool that is used is the root locus, however it is beyond the scope of this project and it will not be analyzed.

They are of special interest the second-order linear systems, *i.e.* the ones that only have 2 poles, as they appear often. In the canonical form, their characteristic polynomial is:

$$D(s) = s^2 + 2\,\zeta\omega_n\,s + \omega_n^2 \tag{2.7}$$

with roots at $s = \sigma \pm j\omega = -\zeta\omega_n \pm j\omega_n\sqrt{1-\zeta^2}$, where ω_n is the natural frequency and ζ is the damping ratio.

Stability and behaviour

The stability of the system will depend on the value of the real part of the roots (σ): if it is negative, we will have asymptotic stability; if its value is 0, we will have marginal stability or oscillations; while if it is positive, the system will be unstable.

The behaviour of the system within the time domain will also depend on the value of ω_n and ζ. For an asymptotically stable system, like the one in figure 2.2, the Settling Time T_S is the time until the system gets to a steady state and the Percentage Over Shot POS is the maximum overshoot of the system's transient response in percent of the steady state value. Both expressions are shown in the following figure:

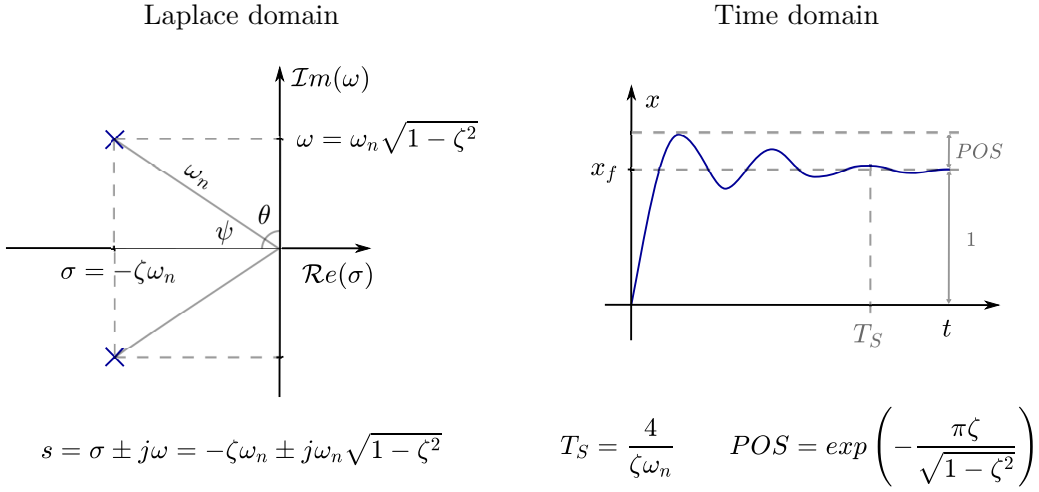

Figure 2.3: Definition of variables in a 2nd order linear system with asymptotic stability

2.3 Modern control theory

The limitations of classical control theory lead to mathematical approaches that provided a more complete description of the dynamics of systems. The following are two examples of tools that were developed to solve those restrictions and face the complexity of multiple-input-multiple-output (MIMO) systems and non-linearity.

2.3.1 State-space representation

State-space representation is a model that describes the dynamics of a system as a set of coupled first-order differential equations of control and state variables together with a set of algebraic equations of state and output variables. In our particular case, there will not be output variables (our outputs will be the state variables themselves), and so, we will only have the set of differential equations.

We will now begin defining the concept *state-space*. It consists of the minimum set of physical variables $x_i(t)$, with $i = 1, \ldots, n$, known as *state variables*, that fully describe the dynamics of a system and its response to any given set of inputs. The number of states, n is called the order of the system.

For a general, time-varying system, the time derivative (or evolution) of a state variable x_i may be written as:

$$\dot{x}_i = f_i(x, u, t) \qquad \text{for} \qquad i = 1, \ldots, n \tag{2.8}$$

where u are the system's inputs or control variables and $\dot{x}$ is the time derivative of x. In this analysis, we will focus on linear and time-independent (LTI) systems, of order n and with m inputs. The general time-derivative of a given state variable is:

$$\dot{x}_i = \sum_{j=1}^{n} a_{ij} x_j + \sum_{k=1}^{m} b_{ik} u_k \qquad \text{for} \qquad i = 1, \ldots, n \tag{2.9}$$

where a_{ij} and b_{ik} are known real coefficients that describe the system. As it is shown, the time derivative of any state variable can be expressed as a linear combination of both the actual states and the control variables. In general $m < n$, i.e. we will have less controls than states.

It is common to find the state equations in a vector form: the set of n state variables will become the *state vector*: $x(t) = [x_1(t),\, x_2(t),\, \ldots, x_n(t)]^T$ and the set of m control variables will become $u(t) = [u_1(t),\, u_2(t),\, \ldots, u_m(t)]^T$. In the matrix representation, coefficients a_{ij} and b_{ik} will be compacted in the matrices A and B. Equation 2.9 will be replaced by the following matrix relationship:

$$\frac{d}{dt}\begin{bmatrix} x_1 \\ x_2 \\ \vdots \\ x_n \end{bmatrix} = \begin{bmatrix} a_{11} & a_{12} & \ldots & a_{1n} \\ a_{21} & a_{22} & \ldots & a_{2n} \\ \vdots & \vdots & \ddots & \vdots \\ a_{n1} & a_{n2} & \ldots & a_{nn} \end{bmatrix} \begin{bmatrix} x_1 \\ x_2 \\ \vdots \\ x_n \end{bmatrix} + \begin{bmatrix} b_{11} & \ldots & b_{1m} \\ b_{21} & \ldots & b_{2m} \\ \vdots & \ddots & \vdots \\ b_{n1} & \ldots & b_{nm} \end{bmatrix} \begin{bmatrix} u_1 \\ \vdots \\ u_m \end{bmatrix} \tag{2.10}$$

that can be expressed in a more compact way $\dot{x} = Ax + Bu$.

Once presented the summarized expression, it is important to note that in a time-independent system, what does not depend on time are matrices A and B. Both the states and the controls will, in general, vary with t. We will not introduce the output equations as in our particular case, the variables that we are interested in are essentially state variables, and so, they would become trivial.

The reason why the state-space approach is so useful in flight dynamics is that it allows to reduce the order of high-order ordinary differential equations to 1st order ODEs. This is achieved by defining as states the first derivative of the greater order variable -as an auxiliary variable- and relating them in trivial rows. An example of this will be seen in following chapters.

Controllability

Controllability is defined as the possibility of steering the system from some initial point to any other within the n-dimensional state space, with an admissible control input and in a finite time. From the state-space approach, the necessary and sufficient condition for matrices A and B for linear controllability is:

$$\text{rank}\begin{bmatrix} B & AB & A^2B & \ldots & A^{n-1}B \end{bmatrix} = \text{rank}\,[C] = n \tag{2.11}$$

where rank denotes the number of linearly independent rows, and the matrix C, often called controllability matrix, has dimensions $n \times mn$.

Stability

The eigenvalues of a matrix A are defined as the solutions for λ of the determinant of the following matrix when it equals 0:

$$\text{eig}\,(A) = |\lambda \mathbb{I} - A| = 0 \tag{2.12}$$

where $\mathbb{I}$ is the identity matrix. Similarly to the transfer function approach, an LTI system will be unstable if any of the eigenvalues of matrix A has positive real part. Otherwise, in case it has any eigenvalue with zero real part, the system will be marginally stable, *i.e.* the system will have bounded-input-bounded-output (BIBO) stability. Finally, the system will be asymptotically stable if and only if all the eigenvalues have a negative real part. Table 2.1 shows what it has just been discussed.

Eigenvalues	**Real part value**	**Stability**
Any	> 0	Unstable
Any	$= 0$	Marginally stable
All	< 0	Asymptotically stable

Table 2.1: Stability in LTI systems according to the location of eigenvalues

2.3.2 Introduction to Differential Geometry

In dynamic systems the configuration space, the set of all possible positions/configurations, is typically curved, as they have rotational degrees of freedom. The classical pendulum or the rotation of an aircraft are good examples of this non-flat nature of space. Differential Geometry arises as a tool to perform calculus on nonlinear curvy spaces and, as a math branch, can be considered a language that introduces new concepts to this field of study. The first of this terms is:

- **Manifold**: is an n^{th}-dimensional space that can be considered everywhere locally diffeomorphic to $\mathbb{R}^n$. In mathematical language, we would say that M is an n^{th}-dimensional C^r manifold if:

  1. $\forall P \in M$, $\exists$ a neighborhood u of point P in M and a diffeomorphism $\varphi : u \to \mathbb{R}^n$,
  2. $\bigcup u_i = M$: the union of all neighborhoods covers the entire manifold and
  3. if $u_i \cap u_j \neq \varnothing$, then $\varphi_j \circ \varphi_i^{-1} : \mathbb{R}^n \to \mathbb{R}^n$ must be a C^r diffeomorphism (compatibility condition).

  The pair (u, φ) is called local/coordinate chart and the collection of $\{(u_i, \varphi_i)\}$ is an atlas of the manifold. The concept *diffeomorphism* refers to a smooth (no discontinuities or jumps, many times differentiable) and one-to-one (injective) relation between two spaces with smooth inverse. Figure 2.5 shows a manifold with the different elements that have been discussed in the definition.

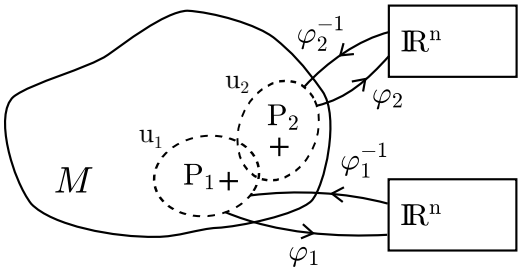

Figure 2.4: The manifold M, neighborhoods u_i, diffeomorphisms φ_i and points P_i. As neighborhoods u_1 and u_2 overlap, they have to fulfill the compatibility condition.

- **Function**: is a map from one space to another. In differential geometry, when a function relates two manifolds it is written in capital letters, while when it maps from a manifold to $\mathbb{R}$ it is written in lowercase.

  An interesting condition of functions is differentiability, the existence of a the derivative in the whole domain. In differential calculus, for a function $f : \mathbb{R} \to \mathbb{R}$, this condition is defined as:

$$\exists \lim_{h \to 0} \frac{f(x+h) - f(x)}{h} \qquad \forall x \in \mathbb{R} \tag{2.13}$$

However, as in a manifold M, h can not be summed to a point as M is a curvy multidimensional space, and thus the definition uses the inverse of the diffeomorphism. A scalar function $f : M \to \mathbb{R}$ is differentiable if for all local charts (u, φ) of M, the map $f \circ \varphi^{-1} : \mathbb{R}^n \to \mathbb{R}$ is differentiable.

For functions that map one manifold to another $\mathcal{F} : M \to N$, with φ and ψ diffeomorphisms of M and N respectively, this condition can be defined the same way or by the use of differentiable scalar functions. $\mathcal{F}$ will be differentiable if:

1. $\psi \circ \mathcal{F} \circ \varphi^{-1} : \mathbb{R}^m \to \mathbb{R}^n$ is differentiable $\forall \psi, \varphi$.
2. $\forall$ differentiable g on N, the scalar function $g \circ \mathcal{F} : M \to \mathbb{R}$ is differentiable.

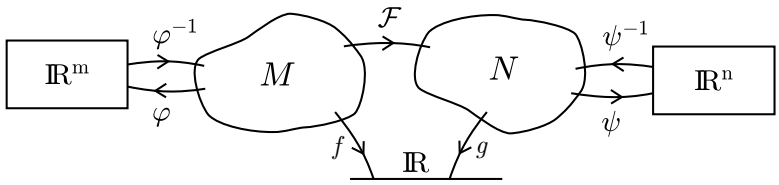

Figure 2.5: Function between two manifolds $\mathcal{F} : M \to N$ and scalar functions $f : M \to \mathbb{R}$ and $g : N \to \mathbb{R}$.

- **Curve**: it is a map from an interval of $\mathbb{R}$, usually thought as time, to a manifold M. It is noted as $\gamma : I \subset \mathbb{R} \to M$. A curve γ is differentiable if:
  1. $\varphi \circ \gamma : I \subset \mathbb{R} \to \mathbb{R}^n$ is differentiable, $\forall \varphi \in M$, or likewise if:
  2. $\forall$ differentiable f on M, $f \circ \gamma : \mathbb{R} \to \mathbb{R}$ is differentiable.

  Let the domain of γ be time, the velocity of a curve will be its time derivative $\gamma'(t)$.

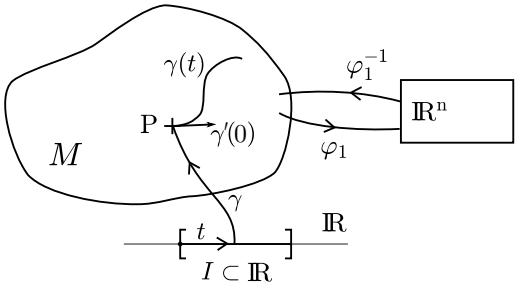

Figure 2.6: Curve γ and velocity of the curve when $t = 0$ at a point P of the manifold $\gamma'(0)$

- **Tangent space**: of a manifold in a point T_pM is the set of all velocities of the curves $\gamma_i'(t)$ passing through a point P of the manifold M. All those velocities will be vectors tangents to the manifold at the point. Given one such vector $v \in \mathbb{R}^n$ and a function $f \in \mathcal{C}^\infty$, the vector acts on the function as:

$$v(f) = v \cdot f = v_1 \frac{\partial f}{\partial x_1} + \cdots + v_n \frac{\partial f}{\partial x_n} = \vec{v} \cdot \vec{\nabla} f \tag{2.14}$$

This operation is called directional derivative of f along v and can be thought as the rate of change of the function f along the direction of vector v. Thus, it returns a real number out of a function: $v \in T_pM$, $v : C^\infty(M) \to \mathbb{R}$. The tangent space can be defined as the set of all attainable velocities at a point P.

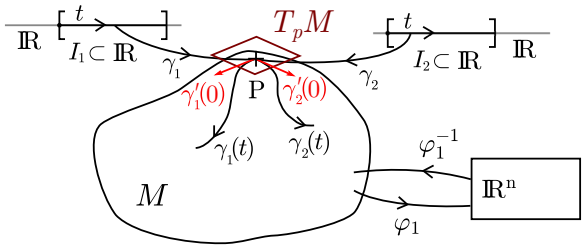

Figure 2.7: Tangent space T_pM formed by the velocities of different curves.

- **Derivation**: is a lineal map defined on a manifold M at a point $P \in M$ and noted $\mathcal{D} : \mathcal{C}^\infty(M) \to \mathbb{R}$, that satisfies Leibniz's product rule:

$$\mathcal{D}(f \cdot g) = f(P) \cdot \mathcal{D}(g) + g(P) \cdot \mathcal{D}(f) \qquad \forall f,\, g \in \mathcal{C}^\infty(M) \tag{2.15}$$

  The set of all derivations at a point $P \in M$ is noted $\mathcal{D}_p(M)$. It can be proven that $T_pM = \mathcal{D}_p(M)$: any vector $v \in T_pM$ is a derivation that takes a function $f \in \mathcal{C}^\infty$ and gives you the directional derivative of f along v and any derivation $\mathcal{D} \in \mathcal{D}_p(M)$ corresponds to the directional derivative along some $v \in T_pM$.

- **Tangent map**: (also called push forward) can be defined as the *derivative* of a mapping between manifolds. Let M and N be two C^k-manifolds with dimensions m and n and atlas $(u_i,\, \varphi_i)$ and $(v_j,\, \psi_j)$ respectively and $\mathcal{F}$ be a function defined $\mathcal{F} : M \to N$. For $x \in \mathbb{R}^m$ and $y = \psi \circ \mathcal{F} \circ \varphi^{-1}(x) \in \mathbb{R}^n$ we will have $\dot{x} \in T_pM$ and $\dot{y} \in T_{\mathcal{F}(P)}N$. The tangent map from $\dot{x}$ to $\dot{y}$ can be thought as the Jacobian of the function $\mathcal{F}$ in P and is noted $\mathcal{F}_*$ at $P : T_pM \to T_{\mathcal{F}(P)}N$.

  With $g \in \mathcal{C}^\infty(N) \to \mathbb{R}$ an infinite times differentiable function in N, $v \in T_pM$ a vector in the tangent space of M and $\mathcal{F} : M \to N$ a function such that $g \circ \mathcal{F} \in \mathcal{C}^\infty(M)$, we have that:

$$(\mathcal{F}_*(v)) \cdot g = v \cdot (g \circ \mathcal{F}) \tag{2.16}$$

- **Tangent bundle**: is the set of all attainable velocities at all points in the manifold:

$$TM = \bigsqcup_{P \in M} T_pM : \{(P,\, v) | P \in M, v \in T_pM\} \tag{2.17}$$

  Note that it is the disjoint union of all tangent spaces: it keeps the identity -the original set- of each element of the union. The tangent bundle forms itself the entire state space, as it is the combination of all positions and velocities within the manifold.

- **Vector field**: is a map that takes a point and returns a vector tangent to the manifold in this specific point. It is noted $v : P \to \mathrm{v} \in T_pM$ and is analogous to a vector valued function on $\mathbb{R}^n$. The set of all vector fields on a manifold M is noted $\Gamma(M)$ or $\mathfrak{X}(M)$.

- **Lie derivative**: given a vector field $X \in \mathfrak{X}(M)$ and a smooth function on M, $f \in \mathcal{C}^\infty(M)$, the Lie derivative of f along X is:

$$\mathcal{L}_X^f = \sum_{j=1}^{n} X_j \frac{\partial f}{\partial x_j} = \vec{\nabla} f \cdot \vec{x} \tag{2.18}$$

  Similar to the directional derivative, it gives a measure of how much a function f changes along X and its result is a function of the point in the manifold. Thus, we can concatenate Lie derivatives along different axes: given $X,\, Y \in \mathfrak{X}(M)$ and $f \in \mathcal{C}^\infty(M)$, then:

$$\mathcal{L}_X(\mathcal{L}_Y f) = \sum_{j=1}^{n} X_j \frac{\partial}{\partial x_j} \left[\sum_{k=1}^{n} Y_k \frac{\partial f}{\partial x_k} \right] = \sum_{j=1}^{n} \sum_{k=1}^{n} \left(X_j \frac{\partial Y_k}{\partial x_j} \frac{\partial f}{\partial x_k} + X_j Y_k \frac{\partial^2 f}{\partial x_j \partial x_k} \right) \tag{2.19}$$

  For an operator to be a Lie derivative, its derivative of the function has to be of first order, thus the concatenation of two Lie derivatives can not be a Lie derivative along any tangent vector V, that is to say $\mathcal{L}_X(\mathcal{L}_Y f) \neq \mathcal{L}_V f$ for $V \in \mathfrak{X}(M)$. The other way round, we would have:

$$\mathcal{L}_Y(\mathcal{L}_X f) = \sum_{j=1}^{n} \sum_{k=1}^{n} \left(Y_j \frac{\partial X_k}{\partial x_j} \frac{\partial f}{\partial x_k} + Y_j X_k \frac{\partial^2 f}{\partial x_j \partial x_k} \right) \tag{2.20}$$

  Taking eq. 2.19 and swapping indices in eq. 2.20, we can get to:

$$\left[\mathcal{L}_X \mathcal{L}_Y - \mathcal{L}_Y \mathcal{L}_X\right] f = \sum_{k=1}^{n} \left[\sum_{j=1}^{n} \frac{\partial Y_k}{\partial x_j} X_j - \frac{\partial X_k}{\partial x_j} Y_j \right] \frac{\partial f}{\partial x_k} = \mathcal{L}_V f \tag{2.21}$$

  which is indeed a Lie derivative along a certain tangent vector V and receives the name of:

- **Lie bracket**: given 2 vector fields on M, $X, Y \in \mathfrak{X}(M)$, the Lie bracket is defined as:

$$[X, Y] \triangleq \mathcal{L}_X \mathcal{L}_Y - \mathcal{L}_Y \mathcal{L}_X = \frac{\partial Y}{\partial x} X - \frac{\partial X}{\partial x} Y \tag{2.22}$$

  As already discussed, $\mathcal{L}_X \mathcal{L}_Y, \mathcal{L}_Y \mathcal{L}_X \notin \mathfrak{X}(M)$, only the Lie bracket's result is a possible velocity of the system as it does belong to the set of vector fields on M. Some notation used for the Lie bracket are: $[X, Y] = \mathcal{L}_X Y = ad_X Y$. For higher order Lie brackets we would have $ad_X^2 Y = [X, ad_X Y] = [X, [X, Y]]$ and, in general, $ad_X^N Y = [X, ad_X^{N-1} Y]$.

- **Integral curve**: given a vector field $V \in \mathfrak{X}(M)$ and a point $P \in M$, $\gamma : I \subset \mathbb{R} \to M$ will be an integral curve of V at P if $\gamma(0) = P$ and $\gamma'(t) = V(\gamma(t)) = V \circ \gamma(t)$, $\forall t \in I$. The existence of a smooth integral curve is dictated by the following lemma: given the vector field $V \in \mathfrak{X}(M)$ and the point $P \in M$, $\exists (a, b) \ni 0$ with $a!$ a curve $\gamma : (a, b) \to M$ will be smooth for $\gamma(0) = P$ and γ being an integral curve.

- **Flow map**: along a certain vector $V \in \mathfrak{X}(M)$ for some time t is noted $\phi_t^V : M \to M$. It takes an initial point P from the manifold and returns the point you would reach after a certain time t following a velocity equal to the vector field V. The time derivative of the flow map will be the velocity:

$$\frac{\partial}{\partial t} \phi_t^V(P) = V(\phi_t^V(P)) \tag{2.23}$$

  The following theorem holds: given two vector fields $X, Y \in \mathfrak{X}(M)$ and a point $P \in M$, if the curve $\gamma : I \to M$ is defined $\gamma(t) = \phi_{\sqrt{t}}^{-Y} \circ \phi_{\sqrt{t}}^{-X} \circ \phi_{\sqrt{t}}^{Y} \circ \phi_{\sqrt{t}}^{X}(P)$ then the velocity at 0 is the Lie product of the vector fields $\gamma'(0) = [X, Y]$.

- **Pullback** of a vector field Y along a function F, denoted $F^* Y$, given a diffeomorphism $F : M \to M$ and a vector field $Y \in \mathfrak{X}(M)$ is defined as $(F_*^{-1}) Y_0 F$.

- **Distribution**: on a manifold M, denoted as Δ, given a point $P \in M$, returns a subspace of the tangent space $T_p M$. A distribution can be:
  - Regular: if the rank of the subspace is constant in the whole manifold.
  - Integrable: if there exists a surface $N \subset M$ such that the distribution at a point P is the tangent space of the surface N at this point $\Delta(P) = T_p N$.
  - Involutive: if for any two vector fields in the distribution $X, Y \in \Delta$ their Lie bracket is also in the distribution $[X, Y] \in \Delta$.

  The Frobenius theorem (1877) states that a regular smooth distribution is integrable if and only if it is involutive: one condition is necessary and sufficient for the other.

- **Family**: of vector fields $\mathfrak{F}$ is a subset of $\mathfrak{X}$: that is to say $\mathfrak{F}(V_1, V_2, \dots V_k) \subset \mathfrak{X}(M)$. The operator Diff($\mathfrak{F}$) is defined as follows:

$$\text{Diff}(\mathfrak{F}) = \{\phi_{t_1}^{V_1} \circ \phi_{t_2}^{V_2} \circ \cdots \circ \phi_{t_k}^{V_k} |\ t_1, \dots t_k \in \mathbb{R},\ V_1, \dots V_k \in \mathfrak{F}\} \tag{2.24}$$

  It is important to note here that time can have either negative or positive values. The flow along a vector V for a negative time $-t$ is equivalent to the flow along the vector $-V$ for time t.

- **Orbit**: of a family of vector fields $\mathfrak{F}$ through a point $x_0 \in M$, is defined as:

$$\mathcal{O}(x_0, \mathfrak{F}) = \{\Psi(x_0) |\ \Psi \in \text{Diff}(\mathfrak{F})\} \tag{2.25}$$

  The following lemma applies: the orbit of a family of vector fields $\mathcal{O}(x_0, \mathfrak{F})$ is a connected immersed submanifold of M, and thus has the same structure as the manifold (theorem known as the Nagano–Sussmann orbit theorem). We can then define the tangent space of the orbit as the set of all attainable velocities:

$$T_x \mathcal{O}(x_0, \mathfrak{F}) = \{\Psi^* V |\ \Psi \in \text{Diff}(\mathfrak{F}),\ V \in \mathfrak{F}\} \tag{2.26}$$

- **Lie Algebra**: of a family $\mathfrak{F} \subset \mathfrak{X}(M)$, denoted $\mathcal{L}ie^\infty(\mathfrak{F})$ is the set of all the Lie bracket combinations of all orders, up to infinity:

$$\mathcal{L}ie^\infty(\mathfrak{F}) = \{ad_{V_i}^n V_j |\ V_i, V_j \in \mathfrak{F},\ n = 0, 1, \dots, \infty\} \tag{2.27}$$

The Lie algebra will be a subset of the vector space: $\mathcal{L}ie^{\infty}(\mathfrak{F}) \subset \mathfrak{X}(M)$. Eventually, for a certain unknown finite value of N, we will have $\mathcal{L}ie^{\infty}(\mathfrak{F}) = \mathcal{L}ie^{N}(\mathfrak{F})$.

Rashevsky–Chow orbit theorem states that if Δ is a regular $\mathcal{C}^{\infty}$-smooth or analytic distribution, the Lie Algebra of Δ at any x is equal to the tangent space of the orbit from any x_0 of the distribution Δ and for all x in the orbit:

$$\mathcal{L}ie^{\infty}(\Delta)|_x = T_x\mathcal{O}(x_0,\, \Delta),\, \forall x \in \mathcal{O}(x_0,\, \Delta) \tag{2.28}$$

2.3.3 Differential Geometry in Modern Nonlinear Control

Similary to the state-space representation, that was used to describe linear time-invariant systems, differential geometry is a good tool to work with nonlinear control affine systems, of the form:

$$\dot{x}(t) = f(x(t)) + \sum_{i=1}^{m} g_i(x(t)) \cdot u_i(t), \tag{2.29}$$

where x is the state vector $x \in M^n$, f is the drift function, g_i are the control vectors and u_i are the control inputs, with:

- x evolving on an n-dimensional manifold: $x \in M^n$,
- f and $g_1, \ldots, g_m$ creating a family of vector fields $\mathfrak{F}$ that is a subspace of the set of all vector fields of the manifold: $\mathfrak{F} = \{f, g_1, \ldots, g_m\} \subset \mathfrak{X}(M)$, and:
- $u_1, \ldots, u_m$ having real values, in general constrained to a control set: $\{u_1, \ldots, u_m\} \in U \subset \mathbb{R}^m$.

When $f(x) = 0$, the system is said to be driftless. We define the **control system** as the triplet of the manifold M, the family of vector fields that define the dynamics $\mathfrak{F}$, and the control set U, and we denote it as $\Sigma = (M, \mathfrak{F}, U)$.

It's now time to defined a controlled trajectory of Σ: it consists of a curve $\gamma : I \subset \mathbb{R} \to M$ subject to:

$$\gamma(t)' = f \circ \gamma(t) + \sum_{j=1}^{m} u_j(t) \cdot g_i \circ \gamma(t), \quad \forall t \in I, \text{ for some } [u_1, \ldots, u_m]^T \in U \tag{2.30}$$

The set of all reachable points from x_0 in exactly time T, denoted $\mathcal{R}_{\Sigma}(x_0, T)$, is:

$$\mathcal{R}_{\Sigma}(x_0, T) = \{\gamma(T) | \, \gamma(0) = x_0\}, \tag{2.31}$$

being $\gamma(t)$ a controlled trajectory. The set of all reachable points in at most time T is, by definition:

$$\mathcal{R}_{\Sigma}(x_0, \leq T) = \bigcup_{t \in [0,T]} \mathcal{R}_{\Sigma}(x_0, t) \tag{2.32}$$

Finally, what is called **reachable set** is the set of all reachable points in any *positive* time, and is denoted as $\mathcal{R}_{\Sigma}(x_0)$. It is important to note here the difference between the orbit and the reachable set; in the first case, time can be negative, and so the negative direction of the flow is also considered, as figure 2.8 suggests:

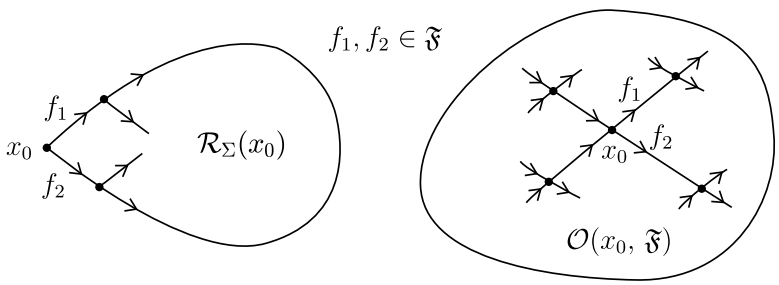

Figure 2.8: Reachable set $\mathcal{R}_{\Sigma}(x_0)$ and orbit $\mathcal{O}(x_0,\, \mathfrak{F})$.

According to this definition, we will now present the following basic concepts in modern control theory:

- **Accessibility**: a system Σ is said to be accessible from x_0 if the set of reachable points after time T is not empty, that is if $\mathcal{R}_\Sigma(x_0, \leq T) \neq \varnothing$.

  In particular, for nonlinear control-affine systems, accessibility is satisfied when the distribution:

$$C = [g_1, \ldots, g_m, [g_i, g_j], \ldots, ad^k_{g_i} g_j, \ldots, [f, g_i], \ldots, ad^k_f g_i] \tag{2.33}$$

  has rank n. This condition is called Lie Algebraic Rank Condition (LARC from now on) and is equivalent to the statement: a system $\Sigma = (M, \mathfrak{F}, U)$ is accessible from $x_0 \in M$ if and only if $\mathcal{L}ie^\infty(\mathfrak{F})_{x_0} = T_{x_0}M$ (as derived by Sussman-Judgevic, 1972).

- **Small Time Local Controllability (STLC)**: a system Σ will be STLC from x_0 if there exists some time $T > 0$ such that the initial point is in the interior of the reachable set: $x_0 \in int(\mathcal{R}_\Sigma(x_0, \leq T))$. It is, thus, a more restrictive condition than accessibility.

  Remind, here, that a point P is in the interior of an interval E if there exists a neighborhood V around P, such that entire neighborhood is a subset of E: $P \in int(E) \leftrightarrow \exists\, V$ around $P \,|\, V \subset E$.

- **Controllability**: a system Σ is said to be controllable from x_0 if the system can be steered from x_0 to any point of the manifold in some time, that is, if $\forall x \in M, \exists\, T > 0$ such that $x \in \mathcal{R}_\Sigma(x_0, T)$.

Figure 2.9 shows a comparison between the three features described above:

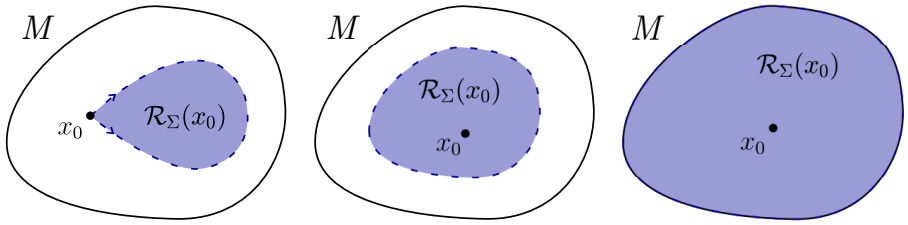

(a) Σ is accessible (b) Σ is STLC (c) Σ is controllable

Figure 2.9: Controllability characteristics of dynamic systems.

Lie brackets generated by control vector fields are called nonlinear Lie brackets and are not included in the linear controllability analysis. When such brackets are needed in order to satisfy the LARC, linear controllability is not ensured, as some directions of motion are not directly actuated: such motions are generated by combinations of direct actuators through time. Therefore, the analysis of nonlinear motion planning techniques is needed.

Nonlinear motion planning

In order to analyze the motion planning of a system in which some of the directions of motions are not directly actuated, we must define an extended system that will have r control inputs that will be denoted as v_k. Thus, we extend the system from eq. 2.29 to:

$$\dot{x}(t) = f(x(t)) + \sum_{k=1}^{r} g_k(x(t)) \cdot v_k(t),\ r > m. \tag{2.34}$$

For $k = 1, \ldots, m$, the vector fields g_k will be the original ones; for $k = m+1, \ldots, r$, on the other hand, vector fields g_k will be the Lie bracket combinations that are needed for the accessibility distribution to cover the entire n-dimensional space (*i.e.,* to have rank n), according to the LARC definition. Those are Lie brackets of control vector fields only, of the form $[g_i, g_j]$ and $ad^k_{g_i} g_j$.

In the extended system, the Lie brackets of control vector fields $g_{m+1}, \ldots, g_r$ are considered 'fictitious' control vectors and their corresponding control inputs $v_{m+1}, \ldots, v_r$ are controls to which we would have direct access. Once obtained the extended control input sequence to steer our system from an initial point to a final one, some transformations need to be made in order to get the original system's control sequences. Such transformations will be discussed in detail in upcoming sections.

Chapter 3

An Overview of Flight Dynamics

3.1 Frames of reference

Flight Dynamics use a series of specific frames of reference in order to project over their axes forces and moments, linear and angular accelerations as well as velocities and positions. All such frames use the Cartesian coordinate system (x, y, z) and are related one another by a set of angular rotations.

We will first define the horizontal frame, considered locally inertial.

Local horizontal frame

The local horizontal frame of reference $F_h(O_h, x_h, y_h, z_h)$ has its origin O_h in an arbitrary position, let it be the center of gravity of the aircraft or CG for the sake of simplicity. Its x_h axis is contained within the horizontal plane and is pointing North, while its y_h, also in the horizontal plane, points East. Finally, the z_h axis points the center of the Earth, creating an orthogonal trihedral.

Although strictly speaking it moves with respect to the inertial frame F_i, located in the center of the Earth, it is considered locally inertial. It receives other names such as vehicle carried vertical frame, north-oriented local-level frame, local geodetic horizon frame or local north-east-down (NED) coordinates.

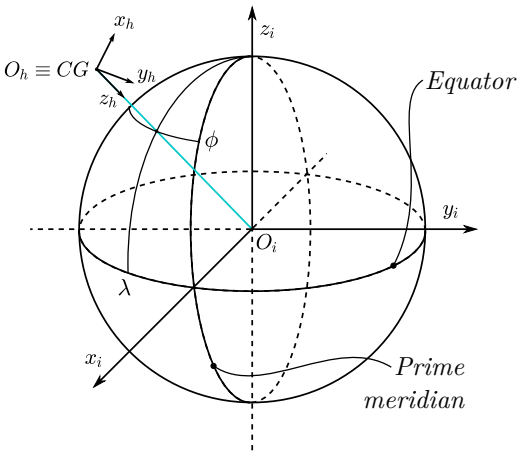

Figure 3.1: Local horizontal frame of reference with respect to the inertial one.

Body frame

The body frame of reference $F_b(O_b, x_b, y_b, z_b)$ is also centered at the CG of the aircraft. Its x_b axis is contained within the symmetry plane of the aircraft and follows a reference line on the body, usually the chord line of the airfoil. The y_b axis is perpendicular to the symmetry plane, in such a way that z_b, contained in the symmetry plane, points downwards.

Wind frame

The wind frame $F_b(O_w, x_w, y_w, z_b)$ is related to the instantaneous aerodynamic velocity of the aircraft. Its origin O_w is again centered at CG, its x_w axis is positive in the direction of the velocity vector of the aircraft and its z_w axis is contained in the symmetry plane of the aircraft, perpendicular to x_w, and pointing downwards. The y_w axis completes the trihedral. Note that if x_w is within the symmetry plane, then $y_w \equiv y_b$.

Euler angles and rotation matrices

Converting a vector $\vec{A}$ from the basis $\mathcal{B}_a = \{x_a, y_a, z_a\}^T$ to any arbitrary basis $\mathcal{B}_b = \{x_b, y_b, z_b\}^T$ can be achieved by applying three elemental rotations about the axes of the coordinate system. Such rotations define the so-called Euler angles.

In general, to go from basis $\mathcal{B}_i$ to $\mathcal{B}_j$ we will multiply our original vector by a rotation 3x3 matrix L_{ji}. As there are 3 rotations to be done from the original basis $\mathcal{B}_a$ to the final one $\mathcal{B}_b$, the following matrices will be used:

$$\vec{A}_1 = L_{1a} \cdot \vec{A}_a \qquad \rightarrow \qquad \vec{A}_2 = L_{21} \cdot \vec{A}_1 \qquad \rightarrow \qquad \vec{A}_b = L_{b2} \cdot \vec{A}_2 \tag{3.1}$$

passing by the auxiliary bases $\mathcal{B}_1$ and $\mathcal{B}_2$. The overall matrix L_{ba} is the matrix multiplication of the matrices defined above and directly converts a vector from basis $\mathcal{B}_a$ to $\mathcal{B}_b$:

$$L_{ba} = L_{b2} \cdot L_{21} \cdot L_{1a}; \qquad \vec{A}_b = L_{ba} \cdot \vec{A}_a \tag{3.2}$$

At this point, it is important to note that L_{ba} is orthogonal, *i.e:* it has unitary determinant and its inverse matrix equals its transpose, as follows:

$$|L_{ab}| = 1; \qquad L_{ab} = L_{ba}^{-1} = L_{ba}^{T} \tag{3.3}$$

From all the possible sequences of axis rotations we will use $z_a - y_1 - x_2$, which is actually called a Tait-Bryan combination. In this case, the matrices look like:

$$L_{1a} = \begin{bmatrix} \cos\delta_3 & \sin\delta_3 & 0 \\ -\sin\delta_3 & \cos\delta_3 & 0 \\ 0 & 0 & 1 \end{bmatrix} \qquad L_{21} = \begin{bmatrix} \cos\delta_2 & 0 & -\sin\delta_2 \\ 0 & 1 & 0 \\ \sin\delta_2 & 0 & \cos\delta_2 \end{bmatrix} \qquad L_{b2} = \begin{bmatrix} 1 & 0 & 0 \\ 0 & \cos\delta_1 & \sin\delta_1 \\ 0 & -\sin\delta_1 & \cos\delta_1 \end{bmatrix} \tag{3.4}$$

Figure 3.2 shows the effect of rotating each base. The resulting matrix L_{ba}, multiplying all matrices is:

$$L_{ba} = \begin{bmatrix} c\delta_2 c\delta_3 & c\delta_2 s\delta_3 & -s\delta_2 \\ s\delta_1 s\delta_2 c\delta_3 - c\delta_1 s\delta_3 & s\delta_1 s\delta_2 s\delta_3 + c\delta_1 c\delta_3 & s\delta_1 c\delta_2 \\ c\delta_1 s\delta_2 c\delta_3 + s\delta_1 s\delta_3 & c\delta_1 s\delta_2 s\delta_3 - s\delta_1 c\delta_3 & c\delta_1 c\delta_2 \end{bmatrix} \tag{3.5}$$

where c stands for the cosine and s is the sine.

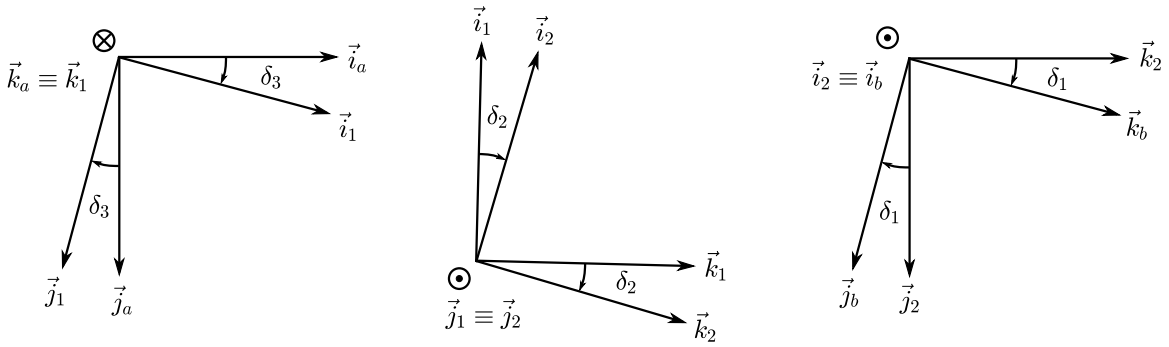

Figure 3.2: The three main rotations, about z_a, y_1 and x_2

According to the original and final basis $\mathcal{B}_a$ and $\mathcal{B}_b$, the Euler angles δ_1, δ_2 and δ_3 will receive different names. Table 3.1 contains the conventional notation for those angles, which will be used in this chapter, as well as the names those angles have:

Matrix	δ_1		δ_2		δ_3	
L_{bh}	ϕ	roll angle	θ	pitch angle	ψ	yaw angle
L_{wh}	μ	bank angle	γ	flight path angle	χ	heading angle
L_{bw}	0	-	α	angle of attack	$-\beta$	sideslip angle

Table 3.1: Name of the different angles $\delta_1, \delta_2, \delta_3$ for each rotation matrix

Note that $\delta_1 = 0$ for matrix L_{bw}. This is due to the fact that both z_b and z_w are contained within the symmetry plane of the aircraft.

3.2 General equations of motion

The physical model that allows us to study the motion of an aircraft is based on the general equations of motion. This approach has, as its main hypothesis, the idea that the aircraft is a rigid body with 6 degrees of freedom (6DOF): 3 of translation of its CG with respect to a certain reference frame and 3 of rotation of the rigid body itself: the angles defined in the previous section.

Force Equations

From the definition of force as the time derivative of the linear momentum $\vec{p} = m\,\vec{V}$, and assuming constant mass, we have:

$$\vec{F} = \frac{d\vec{p}}{dt} = m\frac{d\vec{V}}{dt} = \begin{pmatrix} F_x \\ F_y \\ F_z \end{pmatrix} \tag{3.6}$$

Where $\vec{V} = (u,\, v,\, w)^T$ is the velocity in the body frame. It must be noted, however, that to obtain the time derivative of a vector in an inertial frame of reference, knowing its derivative in the rotating frame, we must add a term witch will be the cross product of the angular velocity at witch the frame is rotating $\vec{\omega} = (p,\, q,\, r)^T$ times the vector being derived. The expression will then be:

$$\vec{F} = m\left(\frac{\partial \vec{V}}{\partial t} + \vec{\omega} \times \vec{V}\right) \qquad \rightarrow \qquad \begin{cases} F_x = m\,(\dot{u} - rv + qw) \\ F_y = m\,(\dot{v} + ru - pw) \\ F_z = m\,(\dot{w} + qu + pv) \end{cases} \tag{3.7}$$

Isolating the acceleration terms and considering the role of the gravitational acceleration in each axis, we reach the final expression:

$$\begin{aligned} \dot{u} &= rv - qw - g\sin\theta + \frac{F_x}{m} \\ \dot{v} &= -ru + pw + g\cos\theta\sin\phi + \frac{F_y}{m} \\ \dot{w} &= qu - pv + g\cos\theta\cos\phi + \frac{F_z}{m} \end{aligned} \tag{3.8}$$

Moment Equations

Similarly, the definition of the force momentum $\vec{G}$ is:

$$\vec{G} = \frac{d\vec{L}}{dt} = \begin{pmatrix} \mathcal{L} \\ M \\ N \end{pmatrix} \tag{3.9}$$

where $\vec{L} = I\,\vec{\omega}$ is the product of the inertia tensor, defined as:

$$I = \begin{bmatrix} I_x & -I_{xy} & -I_{xz} \\ -I_{xy} & I_y & -I_{yz} \\ -I_{xz} & -I_{yz} & I_z \end{bmatrix} \tag{3.10}$$

with diagonal elements:

$$I_x = \int_m (y^2 + z^2)\,\mathrm{d}m \qquad I_y = \int_m (x^2 + z^2)\,\mathrm{d}m \qquad I_z = \int_m (x^2 + y^2)\,\mathrm{d}m \tag{3.11}$$

and inertia products:

$$I_{xy} = \int_m xy\,\mathrm{d}m \qquad I_{xz} = \int_m xz\,\mathrm{d}m \qquad I_{yz} = \int_m yz\,\mathrm{d}m \tag{3.12}$$

with the angular velocity, already defined. The additional rotation element is introduced leading to the simplified expression:

$$\vec{G} = \frac{\partial \vec{h}}{\partial t} + \vec{\omega} \times \vec{h} \qquad \rightarrow \qquad \begin{cases} \mathcal{L} = I_x \dot{p} - I_{xz} \dot{r} + (I_z - I_y)\, qr - I_{xz} pq \\ M = I_y \dot{q} - (I_z - I_x)\, pr + I_{xz} \left(p^2 - r^2\right) \\ N = I_z \dot{r} - I_{xz} \dot{p} - (I_x - I_y)\, pq + I_{xz} qr \end{cases} \tag{3.13}$$

Note that there is no net moment due to the gravitational forces, as the origin of the body-axis system has been chosen at the CG of the aircraft. After manipulating this last expression, we get to:

$$\begin{aligned} \dot{p} &= (C_1 r + C_2 p)\, q + C_3 \mathcal{L} + C_4 N \\ \dot{q} &= C_5 pr - C_6 \left(p^2 - r^2\right) + C_7 M \\ \dot{r} &= (C_8 p - C_2 r)\, q + C_4 \mathcal{L} + C_9 N \end{aligned} \tag{3.14}$$

where:

$$\begin{aligned} C_1 &= \frac{(I_y - I_z)\, I_z - I_{xz}^2}{\Gamma} & C_2 &= \frac{(I_x - I_y + I_z)\, I_x z}{\Gamma} & C_3 &= \frac{I_z}{\Gamma} \\ C_4 &= \frac{I_{xz}}{\Gamma} & C_5 &= \frac{I_z - I_z}{I_y} & C_6 &= \frac{I_{xz}}{I_y} \\ C_7 &= \frac{1}{I_y} & C_8 &= \frac{(I_x - I_y)\, I_x - I_{xz}^2}{\Gamma} & C_9 &= \frac{I_x}{\Gamma} \end{aligned} \tag{3.15}$$

and $\Gamma = I_x I_z - I_{xz}^2$. The three moments, $\mathcal{L}$, M, N can be controlled by the pilot by the use of the control surfaces called ailerons, elevator and rudder, whose deflections are represented by δ_a, δ_e and δ_r, respectively. Additionally, δ_t is the throttle, that controls the thrust force. It must be noted that those deflections also have a role in the three components of force F_x, F_y and F_z, and so, the six equations of force and moments are coupled.

Figure 3.3 shows the nomenclature and sign convention of forces and moments as well as for the control surfaces in a conventional aircraft.

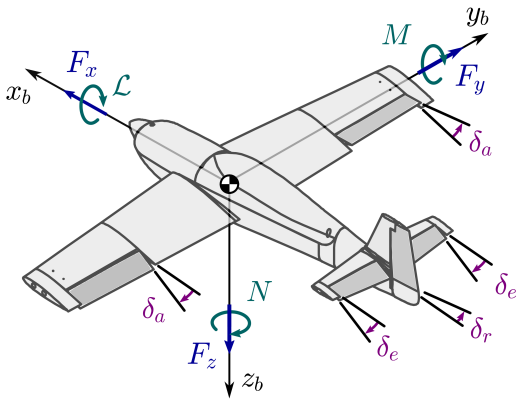

Figure 3.3: Nomenclature and sign convention in a typical aircraft.

Kinematic Equations

From the original expression of the angular velocity:

$$\begin{pmatrix} p \\ q \\ r \end{pmatrix} = \dot{\psi}\vec{i}_b + \dot{\theta}\vec{j}_1 + \dot{\psi}\vec{k}_h \tag{3.16}$$

being the sub-index 2 one of the auxiliary basis, and by projecting the versors into the body frame of reference, we get to:

$$\begin{aligned} p &= \dot{\phi} - \dot{\psi} \sin\theta \\ q &= \dot{\theta} \cos\phi + \dot{\psi} \cos\theta \sin\phi \\ r &= -\dot{\theta} \sin\phi + \dot{\psi} \cos\theta \cos\phi \end{aligned} \tag{3.17}$$

and by manipulating the above expression, we get to the final result:

$$\begin{aligned}\dot{\phi} &= p + \tan\theta\,(q\sin\phi + r\cos\phi)\\ \dot{\theta} &= q\cos\phi - r\sin\phi\\ \dot{\psi} &= \sec\theta\,(q\sin\phi + r\cos\phi)\end{aligned} \tag{3.18}$$

Navigation Equations

To obtain the navigation equations, *i.e:* the equations that describe the translation of the aircraft in the local horizon frame of reference, all that has to be done is the product of the matrix L_{hb}, obtained as the transpose of L_{bh} from table 3.1, and the velocity vector:

$$\begin{pmatrix}\dot{P}_N\\ \dot{P}_E\\ \dot{h}\end{pmatrix} = \begin{bmatrix}\cos\theta\cos\psi & \sin\phi\sin\theta\cos\psi - \cos\phi\sin\psi & \cos\phi\sin\theta\cos\psi + \sin\phi\sin\psi\\ \cos\theta\sin\psi & \sin\phi\sin\theta\sin\psi + \cos\phi\cos\psi & \cos\phi\sin\theta\sin\psi - \sin\phi\cos\psi\\ -\sin\theta & \sin\phi\cos\theta & \cos\phi\cos\theta\end{bmatrix}\begin{pmatrix}U\\ V\\ W\end{pmatrix} \tag{3.19}$$

The product leads to the final result:

$$\begin{aligned}\dot{P}_N &= U\cos\theta\cos\psi + V\,(\sin\phi\sin\theta\cos\psi - \cos\phi\sin\psi) + W\,(\cos\phi\sin\theta\cos\psi + \sin\phi\sin\psi)\\ \dot{P}_E &= U\cos\theta\sin\psi + V\,(\sin\phi\sin\theta\sin\psi + \cos\phi\cos\psi) + W\,(\cos\phi\sin\theta\sin\psi - \sin\phi\cos\psi)\\ \dot{P}_D &= -\dot{h} = -U\sin\theta + V\sin\phi\cos\theta + W\cos\phi\cos\theta\end{aligned} \tag{3.20}$$

Note that in the last equation $\dot{h}$ is in the opposite direction of $\dot{P}_D$. This is because the positive axis of $\dot{h}$ points upwards, unlike $\dot{P}_D$. The variables $\dot{P}_N$, $\dot{P}_E$ and $\dot{P}_D$ can also be referred to as $\dot{x}_h$, $\dot{y}_h$ and $\dot{z}_h$.

3.3 Force analysis

In the development of the force equations in the section above, the expressions F_x, F_y and F_z were used, each of them representing the net force in the direction of the axis denoted by their corresponding subscript, in the body frame. Figure 3.3 also depicts those forces. However, a more thorough analysis of the decomposition of each force is required in the study of the basis of flight dynamics.

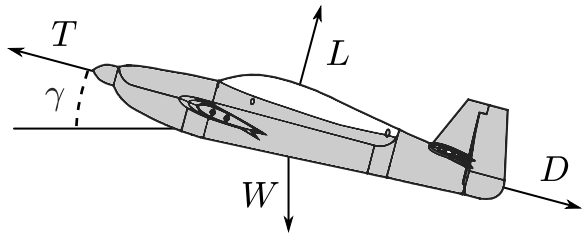

Figure 3.4: Main forces acting on an aircraft.

In the classical approach to the dynamics of a flight, four main forces interact all the time. Lateral forces (F_y) are neglected, and, for a general path angle γ, we have:

$$F_x = T - W\sin\gamma - D; \qquad F_z = W\cos\gamma - L,$$

where T is the Thrust, W is the Weight, D is the Drag and L is the Lift. Figure 3.4 shows a representation of such forces acting on an airplane.

For an aircraft flying at constant height, with $\gamma = 0^{\text{o}}$, the Lift force compensates the Weight and the Thrust makes up for the Drag: $L = W, T = D$. But in general this will not be the case. A deeper analysis of the mentioned forces follows, specially focusing on Lift and Drag.

Lift

In a nutshell, lift force is due to the change in the pressure distribution between the upper and lower surface of an airfoil. It is beyond the scope of this thesis a thorough description of how this force is generated, but we will give a glance to the main definition to better understand the concept of stall.

The general expression for the lift force is:

$$L = \frac{1}{2}\,\rho\, S\, U_\infty^2\, C_L, \tag{3.21}$$

where ρ is the density of the flow in $kg \cdot m^{-3}$, S is the total surface of the wings in m^2, U_∞ is the flow's velocity with respect to the object at a certain distance from the airfoil's surface in $m \cdot s^{-1}$ and C_L is a dimensionless parameter called Lift Coefficient that basically depends on the angle of attack α.

The relationship between C_L and α is considered to be affine for low values of α:

$$C_L = C_{L,0} + C_{L,\alpha} \cdot \alpha, \tag{3.22}$$

where $C_{L,0}$ is the lift coefficient at zero angle of attack and $C_{L,\alpha}$ is the slope of the straight line. Note that in a symmetric airfoil $C_{L,0} = 0$. This expression only holds when the angle of attack is lower than a certain threshold, denoted as α_{stall}, whose value usually ranges from 10 to 15º.

For values of α close to or greater than this critical angle of attack, the relation is no longer linear and due to instabilities the lift coefficient drops dramatically as α increases, as figure 3.5 suggests. This flight regime is called stall and is considered to be dangerous, as stall recovery is not usually immediate and there is a sudden loss of altitude.

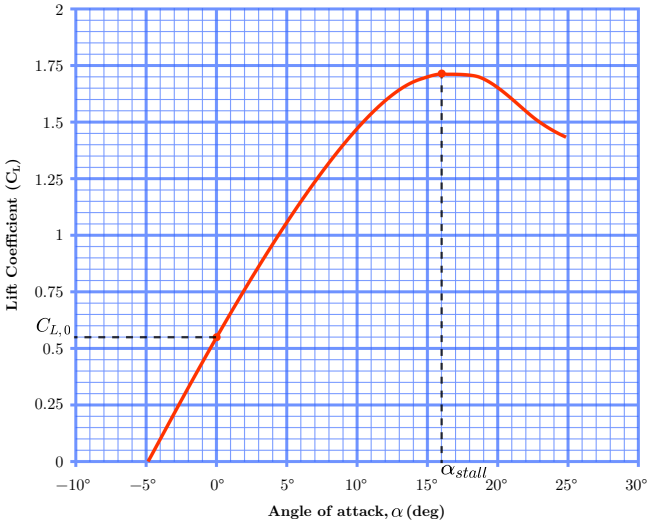

Figure 3.5: $C_L - \alpha$ curve for a SM701 airfoil.

The aileron sensitivity in the rolling maneuver when flying at stall will be discussed in the next chapter as one of the motivations for the LIBRA mechanism.

Drag

Drag is the force that acts upon an object that is moving through a fluid in the opposite direction of its motion. It is, thus, an undesired force as it opposed to the thrust. Like the lift force, it also has a quadratic relationship with velocity:

$$D = \frac{1}{2}\,\rho\, S\, U_\infty^2\, C_D, \tag{3.23}$$

where C_D is the drag coefficient, a dimensionless parameter that has a quadratic relationship with the lift coefficient as:

$$C_D = C_{D0} + kC_L^2 \tag{3.24}$$

This last equation is called the drag polar and is very useful to find the maximum value of the aerodynamic efficiency, defined as the ratio of the lift and drag forces. As the drag polar suggests, and for a symmetric airfoil, the drag force will have a minimum for $\alpha = 0$º and will increase following the shape of a parabola.

When observing the evolution of the drag against velocity, the total force has to be decomposed in two main forces according to their dependency on the velocity: the parasitic and the lift-induced drag. The first of them has a quadratic relationship with velocity while the second has an inverse quadratic relationship. The sum of both contributions results in a drag minimum.

Thrust and weight

The rest of the main forces acting on an aircraft are the thrust and weight. Thrust is the force produced by the engines in the combustion of fuel. It is usually pointing the x-axis of the body frame of reference, but in military aviation its directional might be an additional control parameter. In such case, the angles ϵ and ν are the ones that are commonly used to define its direction.

Finally the weight is the gravitational force that pushes the aircraft to the center of the Earth. Although the mass of the aircraft is not constant due to the ejection of fuel, it is usually considered constant as it doesn't change significantly in relatively short periods of time.

3.4 Stability analysis

Now that all the basic variables have been defined, we will proceed to make a control analysis. Using the state space representation, we will define the 9 different independent states that are involved in the flight of an aircraft: the three components of the velocity, the three components of the aircraft rotation and the three angles of rotation of the aircraft with respect of the horizontal frame of reference:

$$x = \begin{bmatrix} u, & v, & w, & p, & q, & r, & \phi, & \theta, & \psi \end{bmatrix}^T \tag{3.25}$$

As already mentioned, the four main controls in an aircraft are:

$$u = \begin{bmatrix} \delta_a, & \delta_e, & \delta_r, & \delta_t \end{bmatrix}^T \tag{3.26}$$

In the state space representation, and with such defined states and controls, we would have the system $\dot{x} = Ax + Bu$, in which A would be 9x9 matrix and B would be 9x4. As some of the states are not related to each other or their relationships are negligible, many of the components of the A matrix will have values close to 0. The same happens with the controls: not all the actuators affect all the states. A simplification is made to better describe the behaviour of an aircraft, consisting of splitting the system into two subsystems with less states and controls: the longitudinal and the lateral flight dynamics.

Longitudinal

The longitudinal flight dynamics are related to the pitching modes of stability and use, as state variables, u, w, θ and q, and only consider the throttle δ_t and the elevator δ_e as controls. The state space for this subsystem is:

$$\begin{pmatrix} \dot{u} \\ \dot{w} \\ \dot{q} \\ \dot{\theta} \end{pmatrix} = \begin{bmatrix} X_u & X_w & 0 & -g \\ Z_u & Z_w & u_0 & 0 \\ M_u & M_w & M_q & 0 \\ 0 & 0 & 1 & 0 \end{bmatrix} \cdot \begin{pmatrix} u \\ w \\ q \\ \theta \end{pmatrix} + \begin{bmatrix} X_{\delta_e} & X_{\delta_t} \\ Z_{\delta_e} & Z_{\delta_t} \\ M_{\delta_e} & M_{\delta_t} \\ 0 & 0 \end{bmatrix} \begin{pmatrix} \Delta\delta_e \\ \Delta\delta_t \end{pmatrix} \tag{3.27}$$

Note here that the last row in the A matrix is showing how, as expected, the angular velocity q is the time derivative of the angle θ: this is an example of how the state-space representation helps reducing the order of ordinary differential equations. By obtaining the eigenvalues of the A matrix, for a certain aircraft's coefficients, two different modes are found, both of them stable, as their real parts are negative.

The first of the modes, corresponding to two of the four eigenvalues, has a very short period and is physically coupled to the state variables α and q; while the second one, obtained from the other two eigenvalues, has a significantly greater period and is associated with u and θ. They are called short period and phugoid mode respectively.

As there is a clear association of each mode to two of the states, a reduced-order model can be defined for each of them in order to better characterize them. The short period mode would give the following reduced-order model:

$$\begin{pmatrix} \dot{w} \\ \dot{q} \end{pmatrix} = \begin{bmatrix} Z_w & u_0 \\ M_w & M_q \end{bmatrix} \cdot \begin{pmatrix} w \\ q \end{pmatrix} + \begin{bmatrix} Z_{\delta_e} & Z_{\delta_t} \\ M_{\delta_e} & M_{\delta_t} \end{bmatrix} \begin{pmatrix} \Delta\delta_e \\ \Delta\delta_t \end{pmatrix} \tag{3.28}$$

This mode is felt as short period vertical vibrations of the aircraft, that vanish fast, as it is a stable mode. On the other hand, the phugoid reduced-order model will be:

$$\begin{pmatrix} \dot{u} \\ \dot{\theta} \end{pmatrix} = \begin{bmatrix} X_u & -g \\ \frac{-Z_u}{u_0} & 0 \end{bmatrix} \cdot \begin{pmatrix} u \\ \theta \end{pmatrix} + \begin{bmatrix} X_{\delta_e} & X_{\delta_t} \\ \frac{-Z_{\delta_e}}{u_0} & \frac{-Z_{\delta_t}}{u_0} \end{bmatrix} \begin{pmatrix} \Delta\delta_e \\ \Delta\delta_t \end{pmatrix} \tag{3.29}$$

The phugoid mode can be described as a long period cyclic exchange of potential and kinetic energies. When an aircraft is flying at this motion, it climbs up reducing velocity until it starts pitching down, softly increasing velocity. As the period is long, it is not felt as a big disturbance.

Lateral

The lateral flight dynamics involve all the states and control that haven't appeared in the longitudinal study: we have as states v, p, r, ϕ and ψ and have as controls the ailerons δ_a and the rudder δ_r:

$$\begin{pmatrix} \dot{v} \\ \dot{p} \\ \dot{r} \\ \dot{\phi} \\ \dot{\psi} \end{pmatrix} = \begin{bmatrix} Y_v & Y_p & Y_r - u_0 & g & 0 \\ \mathcal{L}_v & \mathcal{L}_p & \mathcal{L}_r & 0 & 0 \\ N_v & N_p & N_r & 0 & 0 \\ 0 & 1 & 0 & 0 & 0 \\ 0 & 0 & 1 & 0 & 0 \end{bmatrix} \cdot \begin{pmatrix} v \\ p \\ r \\ \phi \\ \psi \end{pmatrix} + \begin{bmatrix} Y_{\delta_a} & Y_{\delta_r} \\ \mathcal{L}'_{\delta_a} & \mathcal{L}'_{\delta_r} \\ N'_{\delta_a} & N'_{\delta_r} \\ 0 & 0 \\ 0 & 0 \end{bmatrix} \begin{pmatrix} \Delta\delta_a \\ \Delta\delta_r \end{pmatrix} \tag{3.30}$$

where:

$$\mathcal{L}' = \frac{\mathcal{L} + \frac{I_{xz}}{I_x} N}{1 - \frac{I_{xz}^2}{I_x I_z}} \quad \text{and} \quad N' = \frac{N + \frac{I_{xz}}{I_x} \mathcal{L}}{1 - \frac{I_{xz}^2}{I_x I_z}} \tag{3.31}$$

As it happened before, two of the rows of A are showing that some of the states are defined as the time derivative of others: $p = \dot{\phi}$ and $r = \dot{\psi}$. Besides, the last column of A being all zeros shows that the state that corresponds to the yaw angle, ψ, doesn't have any role in the evolution of the rest of states, which is logical, as flight dynamics don't depend on where the aircraft is pointing. It is also interesting to point out that controls affect to the rate of change of the angles, not to the angles themselves, as matrix B suggests.

As it happened before, we can decompose the lateral dynamics into reduced-order systems. In this case there are up to 3 different modes. The first of them, corresponding to only one of the eigenvalues, that is located in the negative part of the real axis, is the pure roll mode, that can be modeled as:

$$\dot{p} = \mathcal{L}_p \cdot p + \mathcal{L}_{\delta_a} \delta_a \tag{3.32}$$

This mode shows the very intuitive relationship between the aileron deflection and the rolling moment generation. The second of them involves lateral velocity or sideslip and yaw. It is called the dutch roll and its reduced-order model is the one that follows:

$$\begin{pmatrix} \dot{v} \\ \dot{r} \end{pmatrix} = \begin{bmatrix} Y_v & Y_r - u_0 \\ N'_v & N'_r \end{bmatrix} \cdot \begin{pmatrix} v \\ r \end{pmatrix} + \begin{bmatrix} Y_{\delta_a} & Y_{\delta_r} \\ N'_{\delta_a} & N'_{\delta_r} \end{bmatrix} \begin{pmatrix} \delta_a \\ \delta_r \end{pmatrix} \tag{3.33}$$

The dutch roll is a very unpleasant motion as it usually has short period and so, it is usually damped. The last of the lateral modes is the spiral mode, that can not be reduced to a simplified model. This long period mode consists of the aircraft yawing in a spiral shape creating a sideslip velocity and reduction in altitude.

Chapter 4

LIBRA mechanism

After some key aspects in control theory, differential geometry and flight dynamics have been reviewed, it is time to present the LIBRA mechanism: its motivation, the model that uses and the results that have been reached after numerical simulations.

4.1 Motivation

The main motivation of the LIBRA mechanism comes from observing the limitations of the conventional rolling procedure, that uses only the ailerons as actuator. It is well known that the sensitivity of the ailerons in the generation of rolling moment $C_{\delta_\dashv}$ is linearly dependent on the AoA derivative of the lift coefficient $\frac{dC_L}{d\alpha}$. Thus we will analyze its evolution for relatively high values of the AoA. The potential flow lift without leading edge suction can be expressed as:

$$C_L = C_{L_\alpha} \sin\alpha \cos^2\alpha \tag{4.1}$$

being C_{L_α} the slope of the lineal part of the $C_L - \alpha$ curve. Its derivative with respect to the angle of attack is:

$$\frac{dC_L}{d\alpha} = C_{L_\alpha} \cos\alpha \left(\cos^2\alpha - 2\sin^2\alpha\right) \tag{4.2}$$

And, as already mentioned, the sensitivity of the ailerons in their ability to generate rolling moment is linearly dependent on this last expression, and so, we will have:

$$C_{\mathcal{L}_{\delta_a}}(\alpha) = C_{\mathcal{L}_{\delta_{a,0}}} \cos\alpha \left(\cos^2\alpha - 2\sin^2\alpha\right) \tag{4.3}$$

This whole reasoning does also apply to the elevator sensitivity to generate pitching moment, $C_{M_{\delta_e}}$. Figure 4.1 shows this last expression for a significant range of AoA, showing how, at about $\alpha = 30^{\text{o}}$, the curve crosses the x-axis, showing a change in the behaviour. Note that the values are normalized.

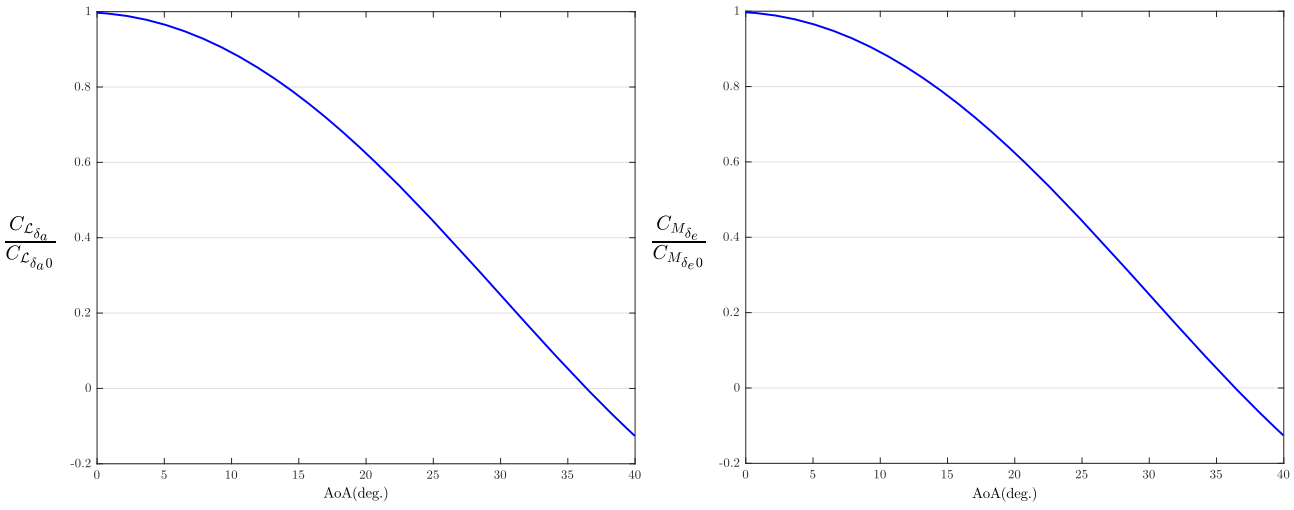

Figure 4.1: Variation of the normalized $C_{\mathcal{L}_{\delta_a}}$ and $C_{M_{\delta_e}}$ with α, extracted and adapted from [16]

In the mathematical model of figure 4.1, the aircraft is supposed to stall at about 30^{o}, and so, the critical AoA coincides with the point at which the aileron's effectiveness changes sign. The same feature was evaluated in the NASA's generic transport model (GTM), giving as result the graph that is shown at figure 4.2.

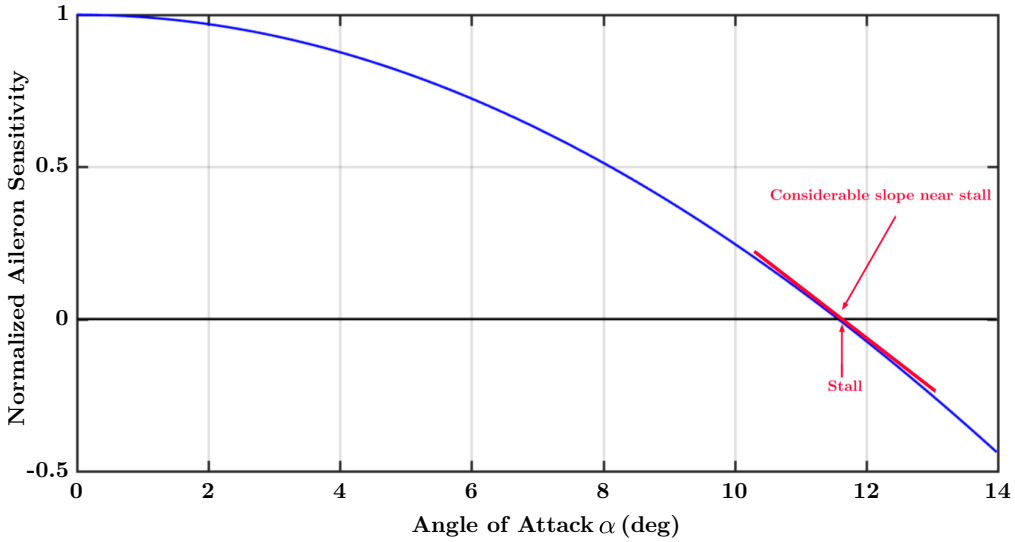

Figure 4.2: Variation of the normalized $C_{\mathcal{L}_{\delta_a}}$ with α, extracted from [18]

The conclusion that can be extracted from those figures is that the aileron sensitivity $C_{\mathcal{L}_{\delta_a}}$ becomes very low at stall up to the point at which it changes sign. Its derivative with respect to α, $\frac{dC_{\mathcal{L}_{\delta_a}}}{d\alpha}$ has a significant value.

The motivation of the LIBRA mechanism was finding a way of generating new control capabilities from the combination of more than one of the available controls. By the Lie product of two or more of the available controls, new directions of motion would be created. This idea is the same one that is used in the parallel parking procedure, in which the car can move to the side by cyclically activating its two available controls: the steering and front-back acceleration. This example is developed more thoroughly in one of the appendices in this thesis.

In another of the appendices, we can find the mathematical expansion of the drift function, the control function and all the first order Lie products generated, a total of 10. From all of them, it is important to note the one shown in eq. 10.10, that shows the Lie derivative of the aileron and the elevator control functions $[g_{\delta_a}, g_{\delta_e}]$. It generates rolling p and pitching r rates that both have a term that is proportional to $\frac{dC_{\mathcal{L}_{\delta_a}}}{d\alpha}$. As already mentioned, this term has a significant value when flying at stall, and so there are reasons to believe that more roll rate will be generated by the Lie bracket of the aileron and the elevator than by only deflecting the aileron.

4.2 Reduced order model

In order to analyze the performance of this unconventional roll mechanism, a reduced-order system was created to simplify the 9 state original one. This model has only three degrees of freedom expressed in a total of 6 states: the heaving motion (z, w) the roll (ϕ, p) and the pitch (θ, q). The standard nonlinear form of the 3DOF reduced-order model flight dynamics is:

$$\underbrace{\begin{bmatrix}\dot{z}\\ \dot{\phi}\\ \dot{\theta}\\ \dot{w}\\ \dot{p}\\ \dot{q}\end{bmatrix}}_{\dot{x}} = \underbrace{\begin{bmatrix} w \\ p + q\tan\theta\sin\phi \\ q\cos\phi \\ -g - \frac{qS}{m}C_Z(\alpha) - \frac{qS}{2m}\frac{\bar{c}}{2V_T}\frac{C_{Z_q}(\alpha)}{\cos\alpha}q - \frac{k_s}{m}z \\ C_2pq + C_3qSb\left(C_L(\alpha) + \frac{b}{2V_T}C_{\mathcal{L}_p}(\alpha)p\right) \\ -C_6p^2 + C_7qS\bar{c}\left(C_M(\alpha) + \frac{\bar{c}}{2V_T}C_{M_q}(\alpha)q\right)\end{bmatrix}}_{f(x)} + \underbrace{\begin{bmatrix}0\\0\\0\\ \frac{qS}{m\cos\alpha}C_{Z_{\delta_e}}(\alpha)\\0\\ C_7qS\bar{c}C_{M_{\delta_e}}(\alpha)\end{bmatrix}}_{g_{\delta_e}(x)}\delta_e + \underbrace{\begin{bmatrix}0\\0\\0\\0\\ C_3qSbC_{\mathcal{L}_{\delta_a}}(\alpha)\\0\end{bmatrix}}_{g_{\delta_a}(x)}\delta_a \qquad (4.4)$$

where the different coefficients are the ones that have already been defined. The states in this case are $x = [z,\ \phi,\ \theta,\ q,\ p,\ q]^T$, and the problem can be expressed in the simplified form $\dot{x} = f(x) + g_{\delta_e}(x)\,\delta_e + g_{\delta_a}(x)\,\delta_a$.

4.3 Comparison with conventional mechanism

In the conventional mechanism, the control input history is just the full deflection of the aileron, in this case, considered to be 30^{o}:

$$\delta_e(t) = 0^{o}, \qquad \delta_a = 30^{o} \tag{4.5}$$

This behaviour is shown in figure 4.3 (a). Meanwhile, in the novel mechanism, the two inputs follow sinusoidal functions with a 90^{o} phase shift between them and at the same frequency. This is a way in which the Lie product of two controls can be applied, as one of the theorems discussed in the first chapter of the theoretical background suggests. The controls that will be applied are, in this case:

$$\delta_e(t) = 2k_e\sqrt{j}\cos j\omega t, \qquad \delta_a(t) = -k_a\sqrt{j}\sin j\omega t, \tag{4.6}$$

where j is a tuning parameter that must be maximized for an optimal performance, and k_a and k_e are scaling factors, used to make the controls fit in their corresponding constraints. Figure 4.4 (a) shows this input history.

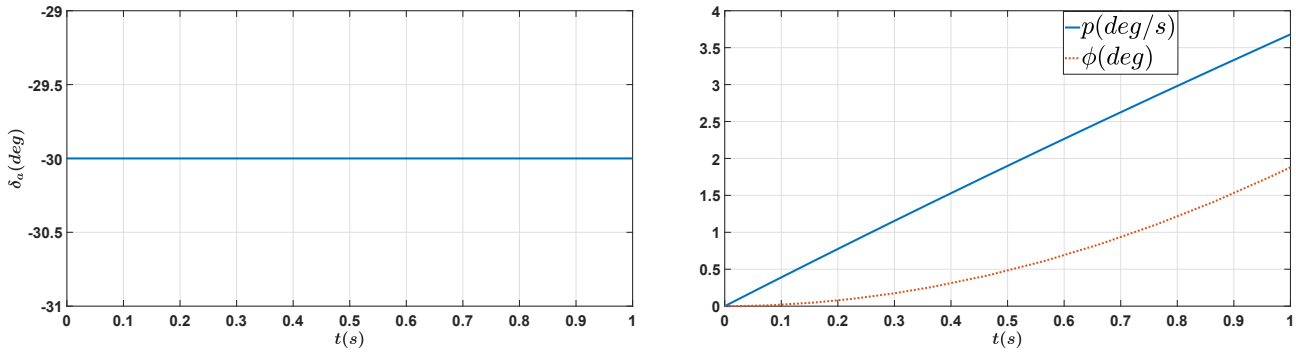

(a) Control input history. (b) Roll output.

Figure 4.3: Conventional roll mechanism numerical simulation, extracted from [18]

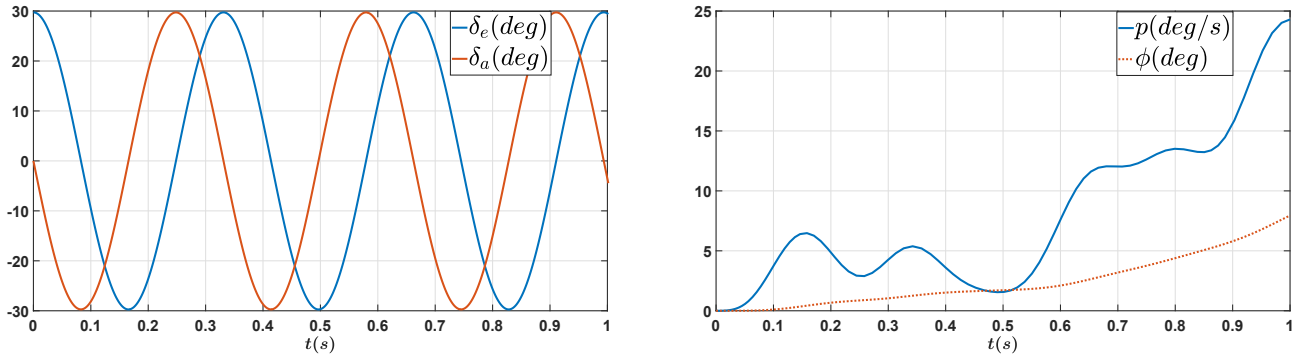

(a) Control input history. (b) Roll output.

Figure 4.4: Novel roll mechanism numerical simulation, extracted from [18]

In the numerical simulations that were run, ω was chosen to be 1 and j to equal 19, giving a frequency in the oscillations of 3Hz. That led to the scaling values of $k_a = 0.119$ and $k_e = 0.0595$, as the maximum deflection available in magnitude is 30^{o} for both the ailerons and the elevator.

Figure 4.3 (b) shows roll output when the conventional roll mechanism was applied at full deflection, while figure 4.4 (b) depicts the roll behaviour of the novel mechanism. In the first of them the final value for the roll angle, after 1 second, is of less than 2, while in the unconventional mechanism it gets to almost 8. This shows an improvement in the control capabilities in the order of 4 times, having the new mechanism greater control capabilities.

Part II

Practical framework

Chapter 5

Design of the 4-axis Load Cell

Within the framework of the first phase in the experimental part of the LIBRA project, a load cell system is required to measure both the lift and drag forces and the pitching and rolling moments that act on an aircraft model mounted in a wind tunnel. In this section, the design of such load cell system and its challenges will be discussed.

5.1 Motivation and evolution

Our main objective is to measure the forces in the x and z directions and the moments in the x and y axes. We need, thus, a 4-axis force sensor to support our aircraft model and give us the proper readings. Currently, this goal can be attained by 6-axis load cells of different capacities available on the market. The main drawback of doing so is that the prices for such devices are very high (they are all over $5000) and that an overload in any if the internal 1D-load cells would cause the whole gadget an irreversible damage, making it useless.

An alternative to such expensive devices is building multi-axis load cell systems by placing several one-dimensional load cells in specific configurations. We need first to understand how those load cells work. Figure 5.1 shows how a 1D load cell works. When a force F is applied to one of the ends, being the other end fixed, the resistances R_1 and R_2 increase and decrease respectively, being their difference ΔR proportional to the force applied. The voltage value that is transmitted to the data acquisition device has a linear relation with ΔR.

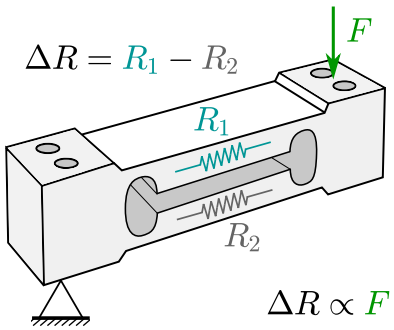

Figure 5.1: Functioning of a 1D load cell.

Earlier efforts have been made to build multi-axis modular load cell systems that can measure forces and moments in different directions and that are composed of more than one 1D-load cell, that are substantially cheaper. Figure 5.2 shows some examples of such designs, all of them developed by Moatasem Fouda, showing for each of them the forces and moments that are being measured.

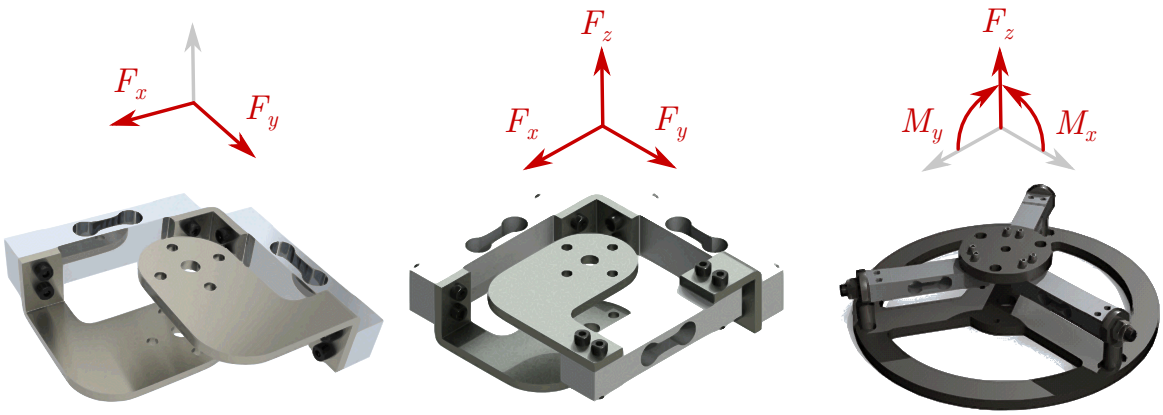

Figure 5.2: Evolution of the multi-axis Load Cell.

From this figure, please note that, in order to measure forces or moments in n directions, at least n 1D load cells will be required. It will be precisely the third of the designs shown in figure 5.2, that our 4-axis load cell system will evolve from, as it already gives as the two moments that we are interested in and one of the forces. Besides aesthetic aspects and changes in the materials used, two main enhancements will be made in order to get to the final result:

- The use of 4 horizontal 90º-separated load cells, instead of 3. Although, strictly speaking, it is not needed, it will ease the calculation of the moments and will decouple the two moments into the two pairs of load cells. Besides, it will avoid cross-talk effects and provide a better accuracy in the overall readings.
- The addition of a vertical load cell, in order to measure the missing force in the upper-left scheme of figure 5.2. The model that will be tested shall be mounted over this vertical load cell.

5.2 Final design

Thus, the final design consists of a 2-by-2 set of 4 horizontal load cells supported by rod end bearings and connected all of them by a mounting structure, at whose center arises the vertical load cell. Over this fifth load cell a mount is fixed, over which a plate with the aircraft will be fastened. The four rod end bearings will be fixed, at the same height on supports, that will be placed in the ends of two horizontal plates joined in a 90º cross by 4 L-brackets. The whole set will be hold by one of the horizontal plates by the two legs installed in the wind tunnel through screws.

For the horizontal load cells, the end connected to the supports is the one that is fixed, while the end that is in contact with the mounting structure is the one over which the force is applied. In the vertical load cell, however, the lower end is considered to be fixed and the force is applied in the upper one.

In order the horizontal load cells to be fixed to the center, the mounting structure is formed by 3 different parts: the main one and the lower and upper plates, whose holes are aligned to enable screwing and fixing the four load cells. Similarly, the vertical load cell is strengthened by four small vertical plates, that rise from the lower plate in the four sides. Figure 5.3 shows the design just described.

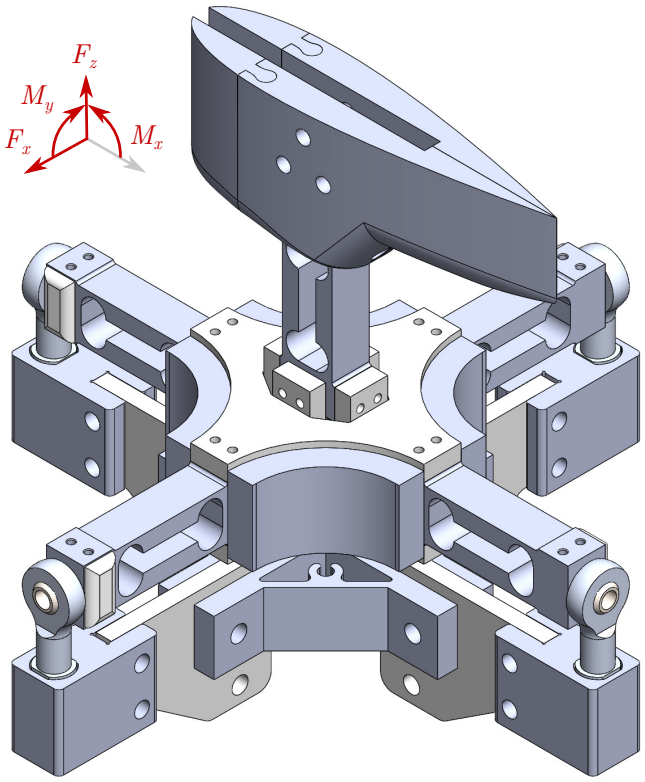

Figure 5.3: Design of the 4-axis modular Load Cell.

In the process of improvement of the load cell system up to three different versions have been manufactured.

First prototype

In the first prototype of the load cell system, all designed pieces were 3D printed using black Z-Ultrat material. Due to the use of this technique, there was an aspect that was very important in the design of the different parts: the direction of printing. As the part is manufactured by applying thin layers of filament following geometric patterns, the result is very resistant to shear forces, forces parallel to the surface of the layer, while it is more fragile to axial forces: those forces that are normal to the layers. In other words, it is much easier to separate layers than to create a crack perpendicular to their surface.

This consideration was specially taken into account in the presence of holes for the screws. In such cases, the reinforcement of the edges did also help make the holes more resistant when the part was printed in the right direction.

In this regard, when in the same part there were holes pointing different directions, some adjustment had to be made, in order to make sure none of the holes would be weak. We have considered two different solutions to this problem:

- Splitting the piece into two different parts, each of them printed in its right direction, that would later on be assembled. This is the case that is shown in figure 5.4. The first assembly acts as an L-bracket and is composed by two equal parts that are glued together. In the second case, the two pieces are also glued, and are inserted by a cross extrusion.
- Creating sleeves in the proper direction to be fit in the main piece. The holes in the main piece will thus have as a greater diameter, equal to the outer diameter of the sleeves. This can be seen in figure 5.6 (d). The mount has up to three different sleeves that are used for the holes to be stronger.

Figure 5.7 (a) shows a photo of the first prototype of the load cell system. It is mostly black, as this was the color of the filament that we used in this version. As the stiffness of the material wasn't good enough, the system was subject to stronger vibrations. This is the reason why we decided to replace the thin parts with laser cut plates. In our first attempt, the second version of the load cell system, we used recycled High-Density PolyEthylene (HDPE) as a material for the plates.

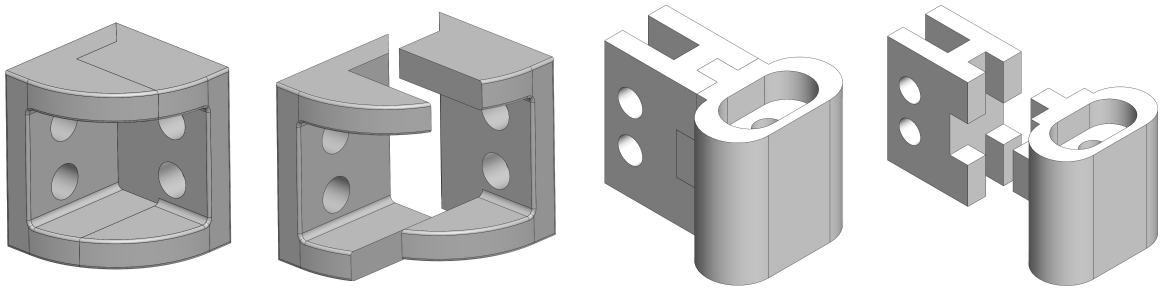

(a) Horizontal plate wedge assembly

(b) Rod end support assembly

Figure 5.4: Details of some of the parts in the first version of the load cell system.

Second version

As already mentioned, in the second version, the thin 3D printed parts were substituted by HDPE laser cut plates. Those plates were recycled and had a thickness of 1/4in. Figure 5.5 shows how the white HDPE plate was laser cut into the different parts.

Apart from this enhancement, there were some other changes that were made in order to improve some aspects of the design:

- Change in the shape of the plates of the mounting structure. The four radius have been increased so that the distance between the hole of the vertical load cell and the edge would increase, in order to reinforce it. The resulting shape of both the mounting structure and the plates is shown in figure 5.6 (c) as well as in the photo of the laser cutting (figure 5.5).

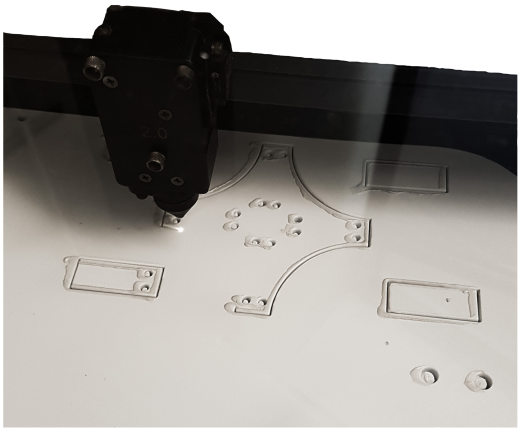

Figure 5.5: Laser cutting of a HDPE plate.

- The horizontal plate wedge was replaced by purchased L-brackets. As it took a time for the order to arrive, we modelled the standard part and 3D printed it. It used sleeves to ensure strength in the direction of the holes, as already discussed. The purchased L-brackets were added to the final assembly.
- In order to strengthen the fixation of the end nod bearings, the 3D printed supports, that are shown in figure 5.4 (b), have been replaced by geometrically simpler parts, that will be manufactured on Computer Numerical Control (CNC). Again, as the CNC parts were not manufactured at that time, we printed them with the exact shape that the CNC would have and used them instead.
- The whole mount was designed in this version. This element, that actually consisted of four different parts, would be mounted at the top of the vertical load cell and would hold another HDPE plate connected to the aircraft model. The mount assembly was designed from the shape of the symmetric airfoil NACA0015 for aerodynamic purposes as it will be a piece that will be very close to the aircraft model.

  The two rear parts of the mount, almost symmetric and located at the trailing edge of the airfoil shape, were the ones that fixed the plate to the vertical load cell through screws; while the front parts had aerodynamic purposes only. Two of the four pieces can be seen in figure 5.6 (d), whereas the whole mount is shown in the isometric projection of the general assembly (figure 5.3).

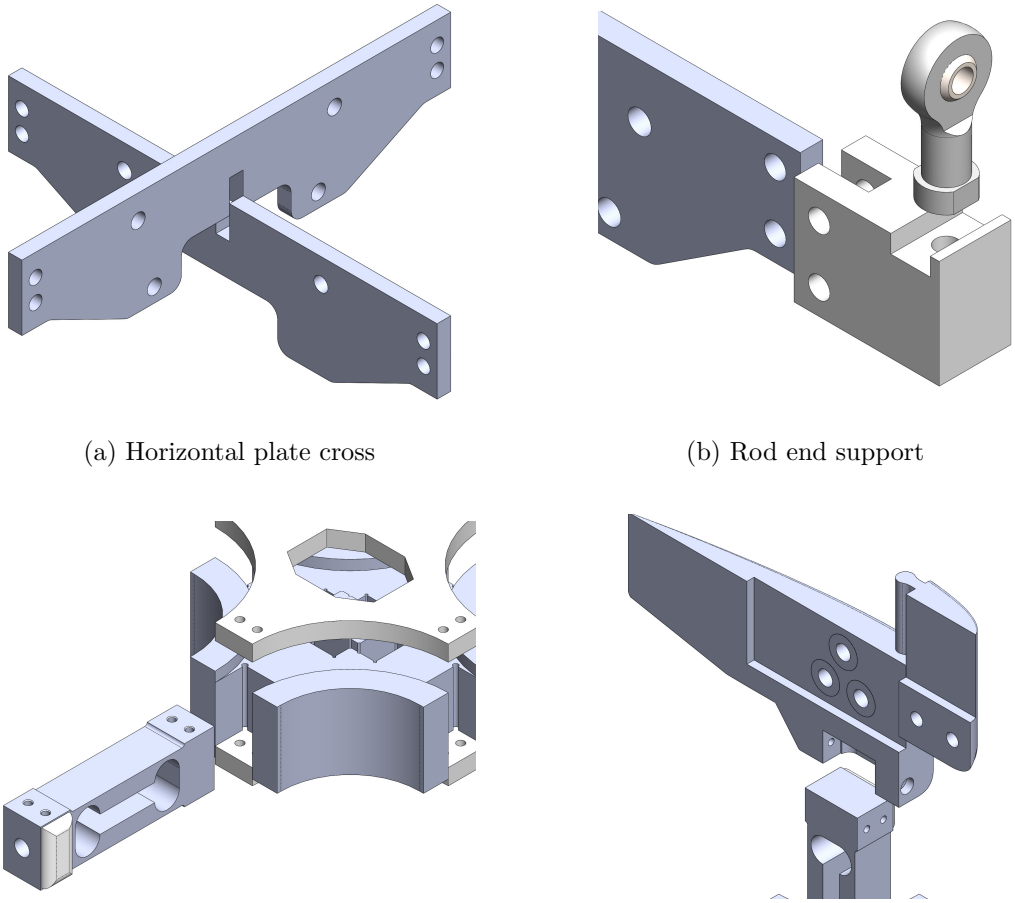

(a) Horizontal plate cross

(b) Rod end support

(c) Main structure and load cell

(d) Load cell and mount

Figure 5.6: Details of some of sub-assemblies in the second and third versions.

Figure 5.6 shows different sub-assemblies of the design: (a) shows how the two horizontal plates are joined, (b) depicts how the end rod bearing are hold in the CNC supports of the third version, the insertion of the load cells in the main structure and the role of the plates can be seen in (c) while the mount is presented in (d).

Besides, figure 5.7, shows photos of the first prototype and the second version as manufactured in the lab. Note that in the first case, the vertical load cell is well located, as it is facing the y-body axis and would measure the lateral forces of the aircraft. This was corrected once the error was noticed.

In the photos, it is shown how the connections of the horizontal plates to the L-brackets and to the supports are done with M6 screws and reinforced by nut nylon inserts. The end nod bearings are fixed to the supports

with M6 screws and to the the load cells with headless M6 bolts with nut inserts: in one of the ends of each horizontal load cell, a hole has been drilled very carefully to this end. Besides, all load cells are fixed to the main structure or the mount by M3 bolts; and finally, the mount holds the plate with three M6 screws.

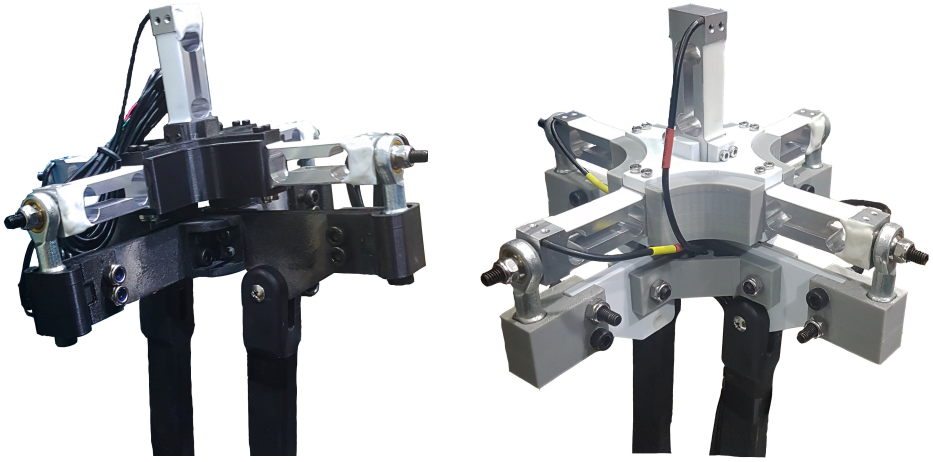

(a) Original version (b) Second version

Figure 5.7: Photo of the two first prototypes of load cell systems.

Final design

As it has already been mentioned, in the final design three main updates have been made:

- Use of laser cut Aluminum plates instead of the HDPE ones.
- Use of the purchased Aluminum L-brackets in the junction of the horizontal plates.
- CNC fabrication for the supports of the end rod bearings.

As a summary, table 5.1 shows the materials used for each of the pieces at each stage of the design:

Version	All plates	L-Brackets	Supports	Main structure	Mount
1	3D printed	3D printed V1	3D printed V1	3D printed	N/A
2	Laser cut HDPE	3D printed V2	3D printed V2	3D printed	3D printed
3	Laser cut Aluminum	Purchased Aluminum	CNC	3D printed	3D printed

Table 5.1: Materials and techniques used in the different parts at each version.

5.3 Calibration

As it is well known, the reading that is obtained from any sensing device is not directly equal to the value of the physical magnitude being measured. The voltage difference from the two wires of a signal has to be corrected by an offset, that will be added to the reading, and a gain, that will be later multiplied. This process is known as the taring and the calibration.

The process of taring consists of setting the zero to be the mean of the voltage values throughout a certain time frame in order to remove the offset that is inherent to the mechanical setup of the experiment. Once the offset is removed, the reading is proportional to the physical magnitude that we intend to measure. The only adjustment that must be made is multiplying the tared reading to a constant, that is the same for all the devices of the same kind.

For the taring process, we will need an accurate measurement of what value the load cell gives when there is no force acting. In order to filter the thermal noise that is intrinsic in our system, several averaging techniques have been considered. As the value that we are interested in is static, the best option has been shown to be a dynamic averager, that takes an updated mean of all the previous readings. The algorithm makes a weighted average of the current sample and the average at the previous iteration. The output is the updated average of all previous samples and tends to converge to a certain value after some time.

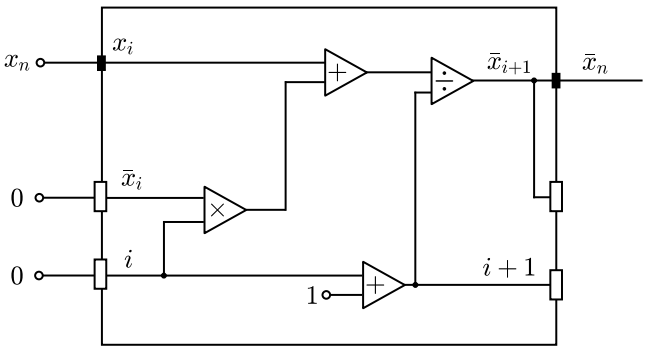

Figure 5.8: Block diagram of the averager of dynamic data.

Figure 5.8 shows a block diagram of the algorithm used. The big box represents a while loop, and the values that go in and out by the small black gates are the input (the dynamic data to be averaged) and the output (the updated average). The white gates are shift registers, that take the value from the previous iteration and are initialized by a constant 0.

Once the reading is tared, we need to find the gain constant to convert the voltage provided by the load cell to the force that we are measuring. As already mentioned, this constant is the same for all load cells of the same kind so we found it by measuring the weight of different objects. The value turned out to be 513.95g/V.

5.4 Testing

In order to figure out if the taring and the calibration processes had been accurately performed, we designed a testing setup. It consisted of a Y-shaped pulley structure, shown on figure 5.10, that would transfer a known weight to the mounting structure at a specific angle through a rope. It was important for the pulleys not to present any friction, as it would result in the weight not being entirely measured by the load cell. By changing the angle of the rope with respect to the load cell system, namely θ, we would get the stress to be split differently among the load cells.

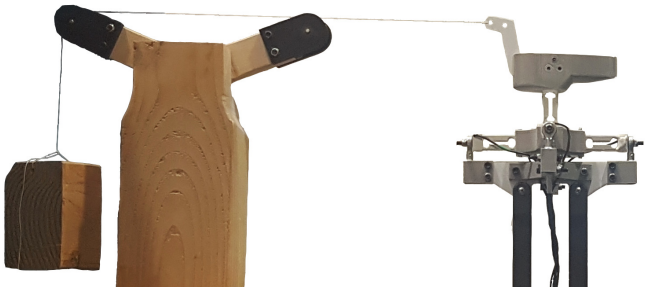

Figure 5.9: Setup for the testing.

Figure 5.9 shows the setup of the testing with $\theta = 0^{\text{o}}$, figure 5.10 shows a photo of the Y-shaped pulley structure.

Figure 5.10: Y-shaped pulley structure.

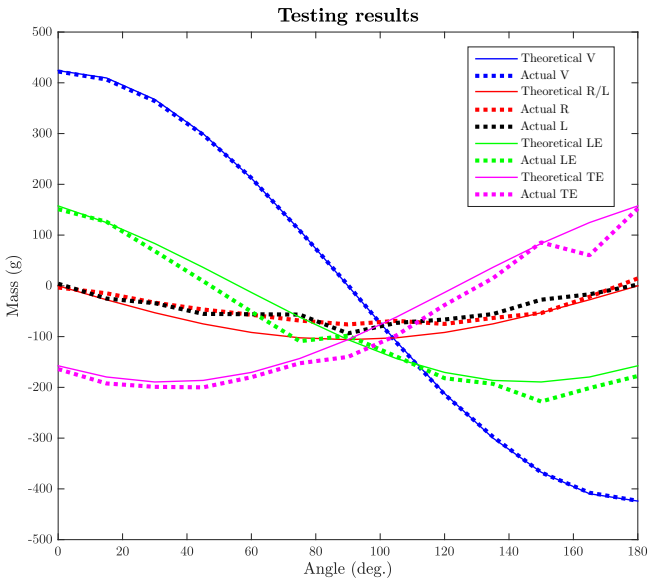

Figure 5.11: Testing results in the full range.

We measured the weight of a wooden block and we obtained a mass of m=424g. The total mass measured in the vertical load cell was m times the cosine of the angle of the rope θ. The vertical component of the weight, m times the sine of θ, would be split into the four horizontal load cells and a moment would arise in the y direction. This moment, proportional to the reading in the vertical load cell, would be split between the LE and the TE in opposite directions.

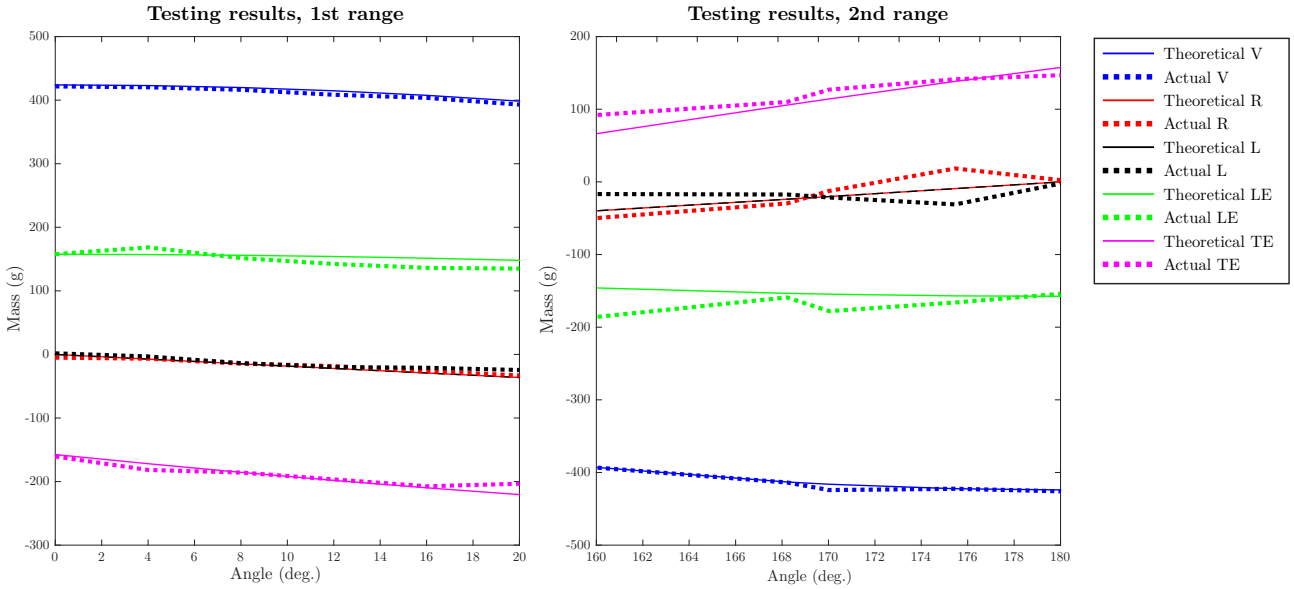

Figure 5.12: Testing results for the two different ranges.

The testing has consisted in two different stages. In the first of them, all the range from $\theta = 0^{o}$ to $\theta = 180^{o}$ has been used, with steps of 15^{o}. Figure 5.11 shows the theoretical or expected values and the obtained ones. In the second stage, we have focused in low values of θ, covering 2 ranges of 20^{o} in steps of 4^{o}. Figure 5.12 shows the obtained values. In general, the calibration shows good results as the measured values match the expectations. The errors that arise in some of the measurements always compensate each other and might be related to not setting the proper angle, to misalignments of the load cells or to stresses caused through the experiment.

5.5 Derivation of forces and moments

In this section the derivation of both the two forces lift and drag and the two moments pitch and roll will be discussed. It is important, first to define some magnitudes that will be used through this analysis:

- Angle θ: is the angle between the horizontal surface of the load cell system and the streamlines in the wind tunnel. It is not directly equivalent to the angle of attack as the chord is not perfectly parallel with the load cells: there is a 8^{o} difference between them.
- Distances x_{CG} and y_{CG}: the x and y distances from the upper plate's center to the CG of the aircraft model and the mount. The procedure that has been followed to determine the position of the CG is discussed in one of the appendices of this thesis.
- Distance d: is the distance between the LE load cell bearing and the TE one, as depicted in figure 5.13.
- Mass m_t: total mass of both the aircraft and the mount. It will be used in the definition of the weight W.

In the first approach, for the sake of simplicity, we will analyze the case in which $\theta = 0^{o}$, in which $\alpha = 8^{o}$, as already discussed and shown in figure 5.13. Later on, we will generalize it to $\theta \neq 0^{o}$.

We will define the horizontal and vertical forces, F_H and F_V respectively, as the summation of all forces measured in the axes x and y of the load cell system, as defined in the figure. The load cell system has been designed in such a way that, regardless of the angle of attack, the defined forces are measured by the different load cells in a very simple way:

$$F_H = f_V; \qquad F_V = f_{LE} + f_{TE} + f_R + f_L, \tag{5.1}$$

where f_i are the forces measured in the different load cells: V is the vertical, LE is leading edge, TE is the trailing edge and R and L are the right and left load cells. From this point, and with $\theta = 0^{o}$, it is very easy to

find the forces:

$$D = F_H; \qquad L = F_V + W, \tag{5.2}$$

where $W = m_t \cdot g$ is the weight of the aircraft and the mount. For the pitching moment M, we will consider the following moment balance in the center of the upper plate, that uses the difference in the readings of the LE and the TE:

$$\left(\frac{f_{LE} - f_{TE}}{2}\right) d = \underbrace{(L - W)}_{F_V} x_{CG} + \underbrace{D}_{F_H} y_{CG} + M \tag{5.3}$$

Note that this last equation can be expressed by the use of F_H and F_V. M will then be:

$$M = \left(\frac{f_{LE} - f_{TE}}{2}\right) d - (L - W)\, x_{CG} - D\, y_{CG} \tag{5.4}$$

In a similar way, the rolling moment is obtained from the difference in the readings of the left and right load cells. The expression for the rolling moment $\mathcal{L}$ follows:

$$\mathcal{L} = \left(\frac{f_L - f_R}{2}\right) d \tag{5.5}$$

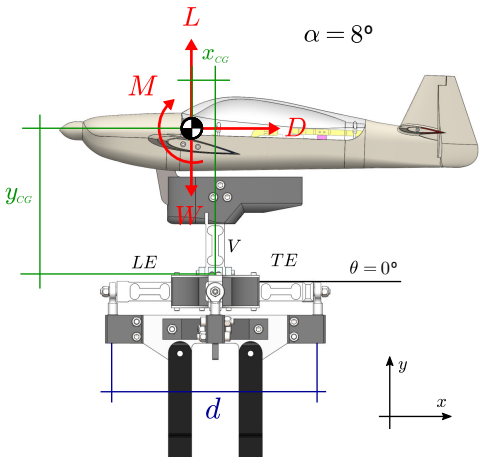

Figure 5.13: Main features introduced, for $\theta = 0^o$.

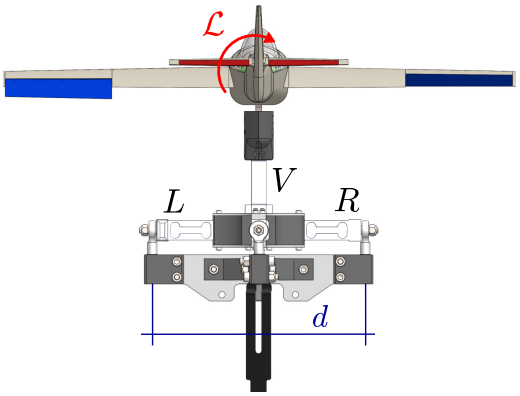

Figure 5.14: Back view of the rolling moment.

Figure 5.14 shows the rolling moment generated by a full deflection of the ailerons, $\delta_a = 30^o$. Note that this derivation is much more simple as the center of gravity is found in the symmetry plane of the aircraft, as discussed in the appendix of the Adjustment of the Center of Gravity.

Now we will consider the case in which $\theta \neq 0^o$. Eq. 5.1 still holds, but now eq. 5.2 will become:

$$D = F_H \cos\theta + F_V \sin\theta \tag{5.6}$$

for the drag force and

$$L = F_H \sin\theta + F_V \cos\theta + W \tag{5.7}$$

for the lift. And so, the horizontal and the vertical forces, F_H and F_V will now be:

$$F_H = D\cos\theta - (L-W)\sin\theta; \qquad F_V = (L-W)\cos\theta + D\sin\theta. \tag{5.8}$$

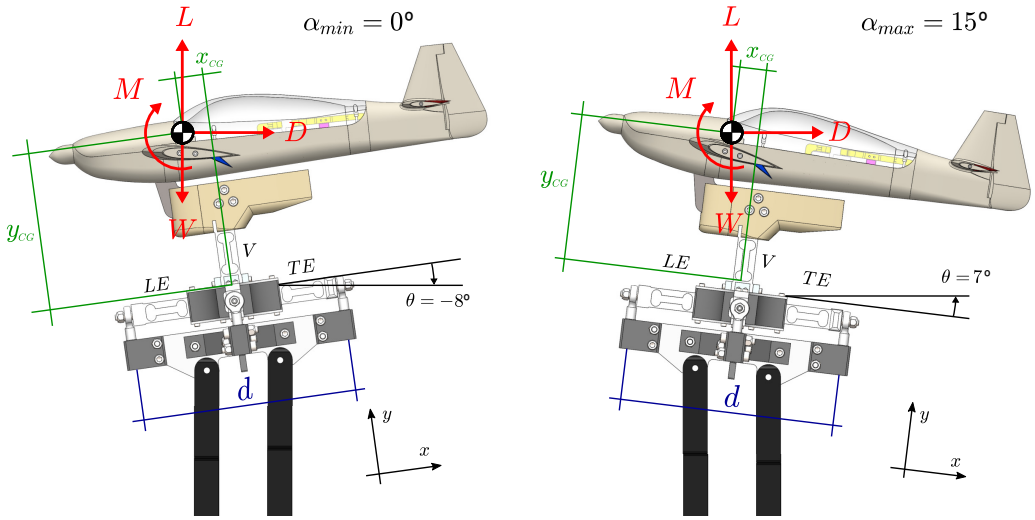

Figure 5.15: Main features introduced, for $\theta = -8^o$ and $\theta = 7^o$.

Chapter 6

Experimental setup

Beyond the load cell system itself, other aspects of the experiment need to be reviewed, as they are also important to be presented because they also belong to the subject of this thesis. They include the aircraft model capabilities

6.1 Aircraft model

The aircraft model that has been used was designed by Moatasem Fouda the previous months and its different parts were manufactured and assembled during the elaboration of the present thesis. Figure 6.1 shows a drawing obtained from Solid Works and a photo of the actual manufactured aircraft model once mounted over the load cell system.

Figure 6.1: SolidWorks screenshot and photo of the manufactured aircraft model in the load cell system.

The requirements for the aircraft model that was designed for the phase 1 of the project are the ones that follow:

- Ability to deflect both the ailerons and the elevators at maximum values of $\pm 30^{o}$. Deflections must be independent one another, in the sense that one surface will be able to deflect without the other one being deflected.
- Stiffness in the wings to support high velocity air flows in the wing tunnel.
- Aerodynamic shape to minimize the drag force being produced at high angles of attack, as the airplane will be tested after stall. To this regard, the airfoil used was the symmetric NACA-0015 airfoil.
- Similar shape and proportions to a conventional aircraft, for the sake of being able to extrapolate the obtained data to a life-size aircraft.

- Existence of a hole in the lower part of the nose of the fuselage, through which a metallic plate will connect the load cell system mount to the aircraft, via the carbon fiber bars that go all the way through the wings.

Most of the pieces of the aircraft were 3D printed, and so were most of the components of the internal mechanism that converted the movement of the two servo motors to deflection in the control surfaces. Additionally, metallic bars were used as rails for the sliders, carbon fiber bars were used to ensure stiffness in the wings and bolts of different sizes were used in the whole assembly.

Figure 6.2 shows two more Solid Works views of the aircraft, the first of them showing and isometric view of the aircraft with the fuselage cover, and the second one showing the interior mechanism.

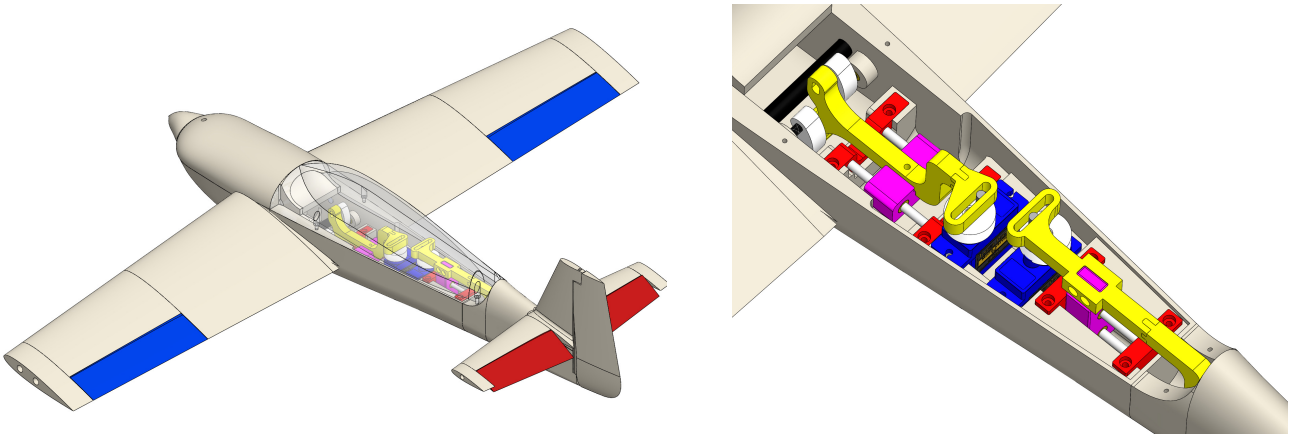

Figure 6.2: Isometric view of the aircraft and detail of the internal mechanism.

Some aerodynamic dimensions of the aircraft, that will later been used later on in the calculation of dimensionless coefficients, can be found in table

Wingspan, b (m)	0.6	**Mean chord**, $\bar{c}$ (m)	0.088	**Wing surface**, S (m^2)	0.045135

Table 6.1: Main aerodynamic dimensions of the aircraft model used.

Such magnitudes will be used in the process of making forces and moments become dimensionless parameters that do not depend on the Reynolds number. Note here that the mean chord was derived by making the mean of the maximum chord, the one in contact with the fuselage, and the minimum one, in the wing tip.

6.2 Hardware used

The main hardware equipment that has been needed in this experiment is listed here:

- **National Instruments DAQ**, NI USB-6211: the data acquisition system that collected the signals from the different load cells and transferred them into the LabView software. A total of 10 analogue inputs were needed, as the signal is read as the difference between two values. This device is shown in figure 6.3.
- **Arduino UNO board**: the classical board that will be used for two main purposes:
  - Implementation of the software that will manipulate the different control surfaces. For each of them 2 wires will be connected as digital outputs.
  - Excitation of the 5 load cell systems. The values for the excitation voltages required are $V^+ = 5V$ (red wire in the load cell) and $V^- = 0V$ (black wire).

  A drawing of this device is shown in figure 6.4.
- **Load Cell TAL226**: force sensor that has a capacity of ± 5 kg. The configuration of the different load cells in the whole measuring system has already been discussed in detail and will not be commented on here. Figure 6.5 shows a drawing of such device, showing the five different wires. The green and white wires will be connected to the data acquisition system, while the thin black and red will be connected to the voltage source of the Arduino board. The thick black will be connected to the thick black wires of the rest of load cells.

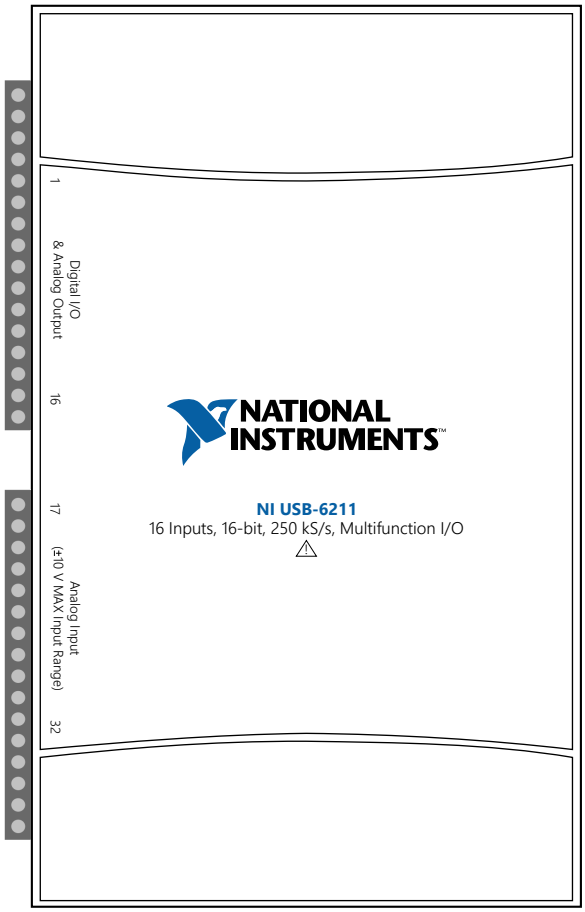

Figure 6.3: National Instruments USB-6211 data acquisition module.

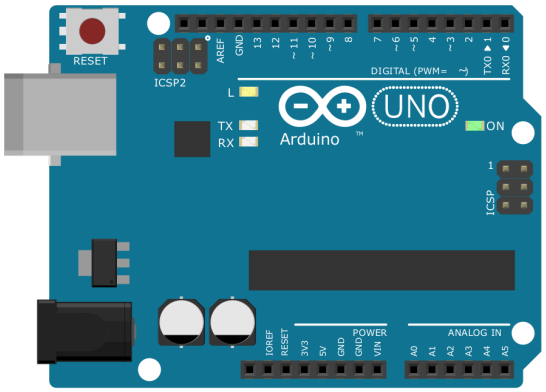

Figure 6.4: Arduino UNO board.

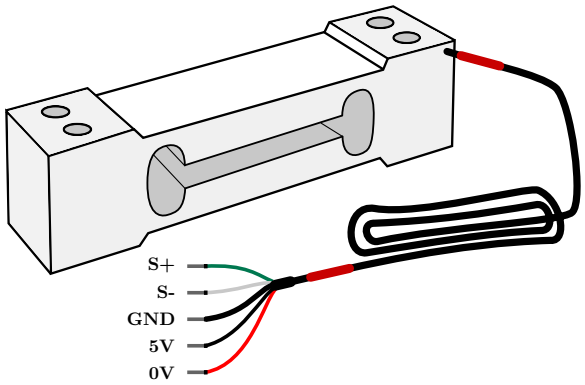

Figure 6.5: Load Cell Tal226 force sensor.

6.3 Interface software

Apart from the use of Excel sheets in the collection and processing of data, and of Matlab in the creation of plots, the two main software tools that have been used in the experiments are Arduino and LabView. The former was used to control the actuators and the later was needed to tare the load cell system and to display the readings from the five devices.

The Arduino code, that can be found in one of the appendices of this thesis, is used to deflect the ailerons and elevators independently. Different wires connect the board with the two DC motors that work separately. In the interface console, the user must type a message that will be understood by the program as follows: 'letter'+'number'+','. The letter can be an a in case the ailerons need to be deflected or e for the elevator. The number will correspond to the deflection required in degrees according to the sign convention that has been already described.

The LabView program was used in the processing and displaying of the readings coming from the load cells. The taring and calibrating of the raw data was also performed by this software tool, as well as the removal of noise by averaging. One of the appendices of this thesis shows screenshots of the program used and discusses its functioning, presenting an example of SubVI.

Part III

Results and conclusions

Chapter 7

Experimental results

In this section, we are presenting the results that have been reached after testing the aircraft model in the wind tunnel with the use of the load cell system. The whole experimental part has been divided into 3 different sections, according to the control surface that has been analyzed. Thus, in the first section, we present the results for the moments and forces acting in the airplane with no deflection in any of the control surfaces. In the second section we focus on the aileron role to obtain rolling moment at different angles of attack, which is the main purpose of this thesis. Finally, we run an additional study on the forces and moments with the elevators being fully deflected, specially paying attention to the pitching moment.

7.1 No deflection

We run up to five different experiments over the full range of angles of attack -from 0^{o} to 20.125^{o}- in different days and after having tared the load cell system in different occasions, in order to ensure consistency in the results. The main objectives of the zero-deflection study are, on the one hand find out if the measuring system works correctly, by comparing the $C_L - \alpha$ curve to the theoretical one, and on the other hand, to determine the stall angle of the designed airplane by observing the $C_D - \alpha$ curve.

Besides, by repeating the same experiment different times, we will be able to determine the consistency of the results, as already mentioned, and we will be able to analyze the drag polars. We will also compare the results from the experiments with the full deflection experiments, shown in upcoming sections with the ones obtained in this section, particularly the rolling moment for the aileron deflection case and the pitching moment in the elevator deflection one.

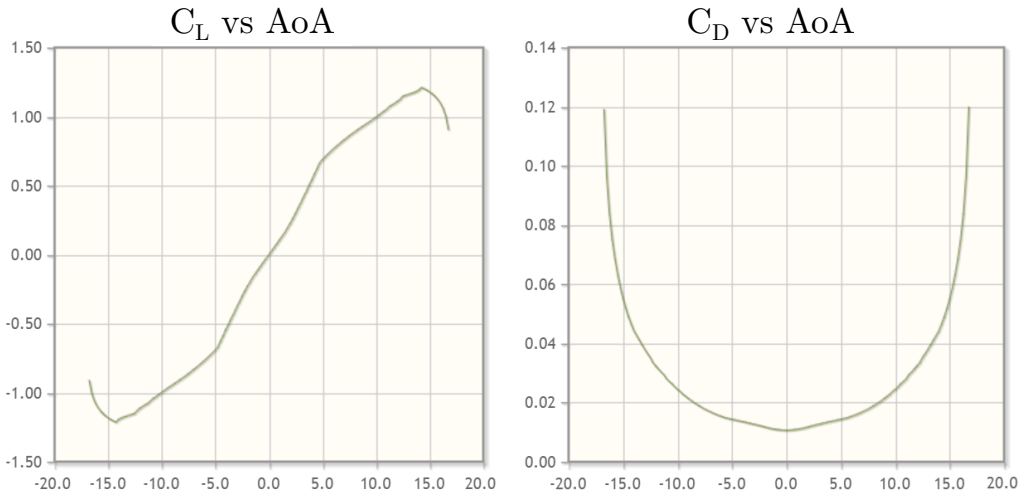

Figure 7.1: $C_L - \alpha$ and $C_D - \alpha$ curves for the NACA-0015 airfoil at $Re = 100.000$, from Airfoil Tools.

The airfoil that has been used in this aircraft was a NACA 0015. As its name suggests, this airfoil is symmetric, and its behaviour is well known. In general, the aerodynamic behaviour of any airfoil depends on the Reynolds number Re, a dimensionless parameter in fluid dynamics that compares the inertial and the viscous forces, and

is defined as:

$$Re = \frac{\rho \cdot U \cdot \bar{c}}{\mu}, \tag{7.1}$$

where ρ is the density of the fluid, U is its velocity, $\bar{c}$ is the reference longitude, the average chord in this case, and μ is the dynamic viscosity of the fluid. In our case, being the air constants $\rho = 1.22\,kg \cdot m^{-3}$ and $\mu = 18.5 \cdot 10^{-6} Pa \cdot s$ and with a velocity of $25\,m \cdot s^{-1}$ and a measured average chord of $0.088\,m$, the Reynolds number is about $Re = 145000$.

Figure 7.1 shows two important features of the NACA airfoil: the $C_L - \alpha$ and $C_D - \alpha$ curves. The first one shows the expected lift coefficient at a certain range of AoA. It is important to note that it passes through the origin as it is a symmetric airfoil and that stall is found at some point between AoA = 10 and 15º. Its behaviour shows odd symmetry with respect to the origin for negative values of AoA, showing negative lift force for $\alpha < 0$.

The second plot of figure 7.1 shows the drag force with respect to the AoA. Again, due to the symmetry in the airfoil, we can find the same behaviour for negative and positive values of α, and in this case we have even symmetry and a minimum for the drag force at $\alpha = 0$. When stall is reached, the drag force starts increasing dramatically.

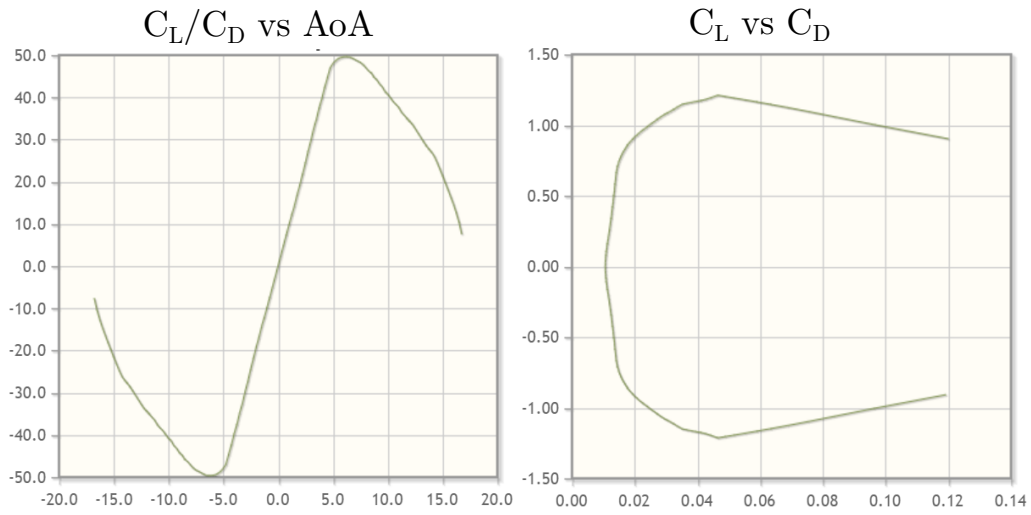

Figure 7.2: $C_L/C_D - \alpha$ and $C_L - C_D$ curves for the NACA-0015 airfoil at $Re = 100.000$, from Airfoil Tools.

Figure 7.2 shows the $C_L/C_D - \alpha$ and $C_L - C_D$ theoretical curves of the airfoil. In the first of them, we can see the quotient of the lift and drag coefficients for a certain interval of the AoA; this is the exact same thing as the Lift-to-Drag ratio, as the dimensionless parameters are defined the same way with respect to the corresponding forces. It is also known as aerodynamic efficiency and it has its maximum before the stall angle. After its maximum, it decreases dramatically.

The second plot of the figure shows the lift to drag coefficients' relation. The angle of attack appears explicitly in the graph as a parameter: at each point of the curve, we have a certain value for the AoA. It is also a symmetric plot, in this case with respect to the x-axis.

The relationship between the first and second graphs can be seen very easily as follows: from the $C_L - C_D$ curve, a straight line is drawn from the origin tangent to the curve in the first quadrant. The point of tangency will correspond to the maximum in the lift-to-drag ratio (plot in the left). In this case, the point is $C_L = 0.75$ and $C_D = 0.015$; and its ratio is equal to 50, which corresponds to the maximum in the $C_L/C_D - \alpha$ graph.

In the comparison of the expected curves with the ones obtained experimentally, it is important to note that in our experiment we are testing the whole aircraft instead of just the airfoil, and thus there are other contributions that also play a role in the aerodynamic performance, such as the fuselage, the horizontal tail and the mount and plate that hold the structure. Their effect will also be discussed.

In the zero-deflection scenario, the experiment was conducted up to five times in different dates, in order to check the consistency of the obtained data. The environmental conditions were very similar: temperature was about 24ºC and pressure was around 100hPa. The range of AoA in this experiment was from 0º to 20.125º in steps of 0.875º.

Figure 7.3 shows the different forces and moments as a function of the AoA in the different experiments. In general, they show very similar behaviours. The pitching moment, always negative due to the role of the

horizontal tail, keeps increasing in magnitude until it gets to the stall angle. It then starts decreasing again in the presence of vibrations that generate some disparity in the pitching moment readings.

The rolling moment, in the other hand, is much lower in magnitude, and theoretically should be zero for all values of α due to the symmetry of the aircraft. Right after stall, there is a positive peak in the rolling moment. This peak does also appear in the rolling moment when the ailerons are deflected, see figure 7.9 below. It can be attributed to some feature in the shape of the aircraft model or to some effect due to the mounting structure. Further experiments with different airplane designs might determine if this effect is inherent to stall and so it is independent of the shape of the aircraft model.

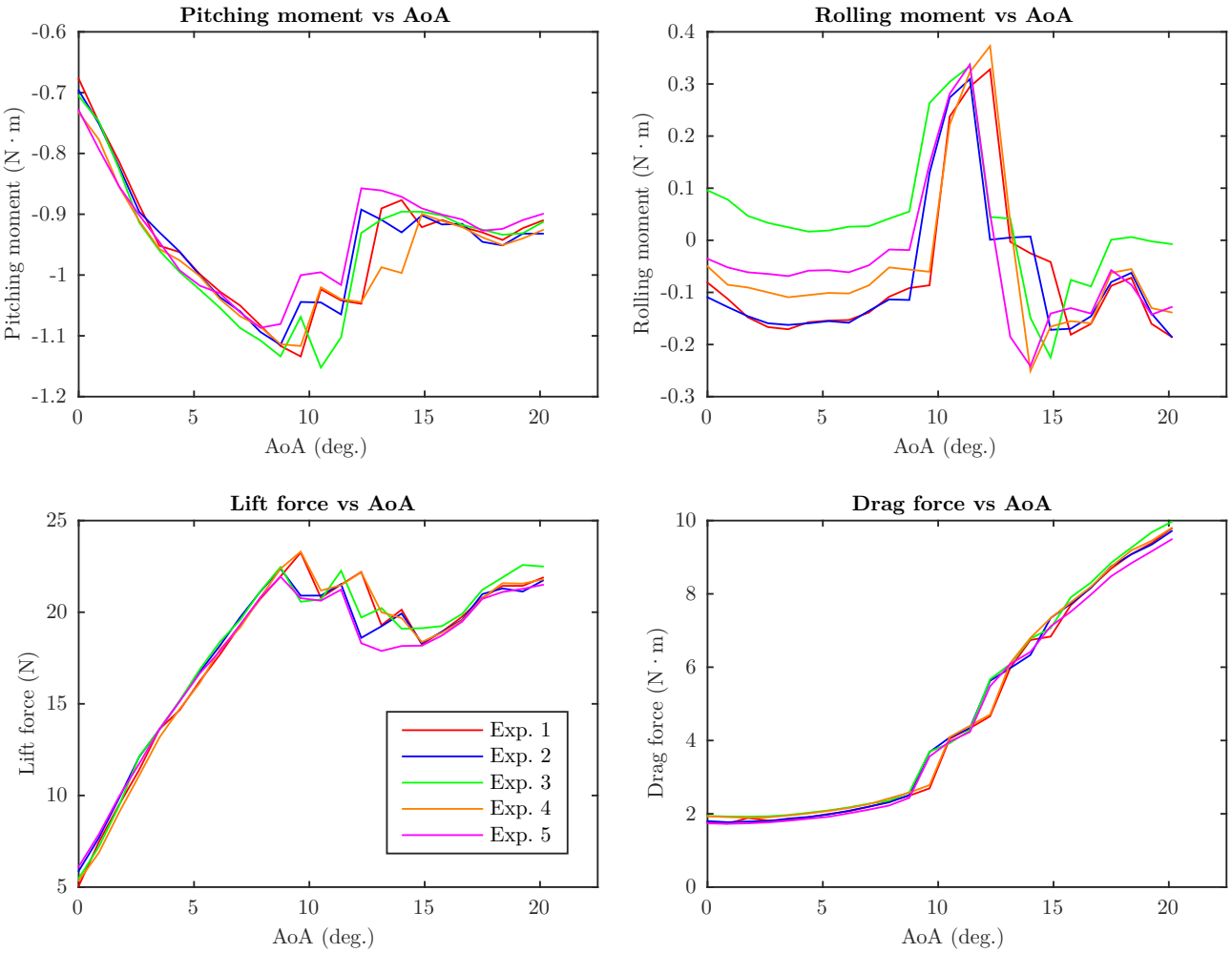

Figure 7.3: Forces and moments obtained with no deflection.

The $L - \alpha$ curve shows the expected behaviour. Its linear part has two slightly different slopes, changing at $\alpha \approx 4^{o}$, as expected in figure 7.1. The lift coefficient at zero AoA is not zero, an effect that is due to the geometry of the whole aircraft being tested. The stall angle appears to be before, also due to the shape of the fuselage. After stall, lift decreases significantly until a certain point, around $\alpha = 15^{o}$, where it increases again. It is important to note here that this increase in the lift would only be achieved if velocity was kept the same, which is almost impossible considering the big increase in the drag force.

The last graph of the figure shows the drag force with respect to the AoA. As expected, it keeps almost constant -slightly increasing- until stall, when it begins escalating with a high and constant slope. As we know, this is due to the airflow separation from the airfoil, producing vortexes in the wings.

Figure 7.4 shows the different moments (the graph on the left) and forces (the one on the right) averaged through the five experiments. It can be seen that the pitch moment is greater than the rolling moment in magnitude and that the stall effect is detected in the lift and drag curves for the same critical AoA, around 8.

Figure 7.3 might incorrectly suggest that forces are measured with a higher precision than moments: the absolute error of the different readings around the mean looks much lower for forces than for moments. This is confusing as they are not expressed in the same units, and they don't have similar absolute values. Figure 7.5 shows the

standard deviations for forces and moments around the mean. As already mentioned, it is important to note that the deviations are not expressed in the same units, and they can not be compared in magnitude.

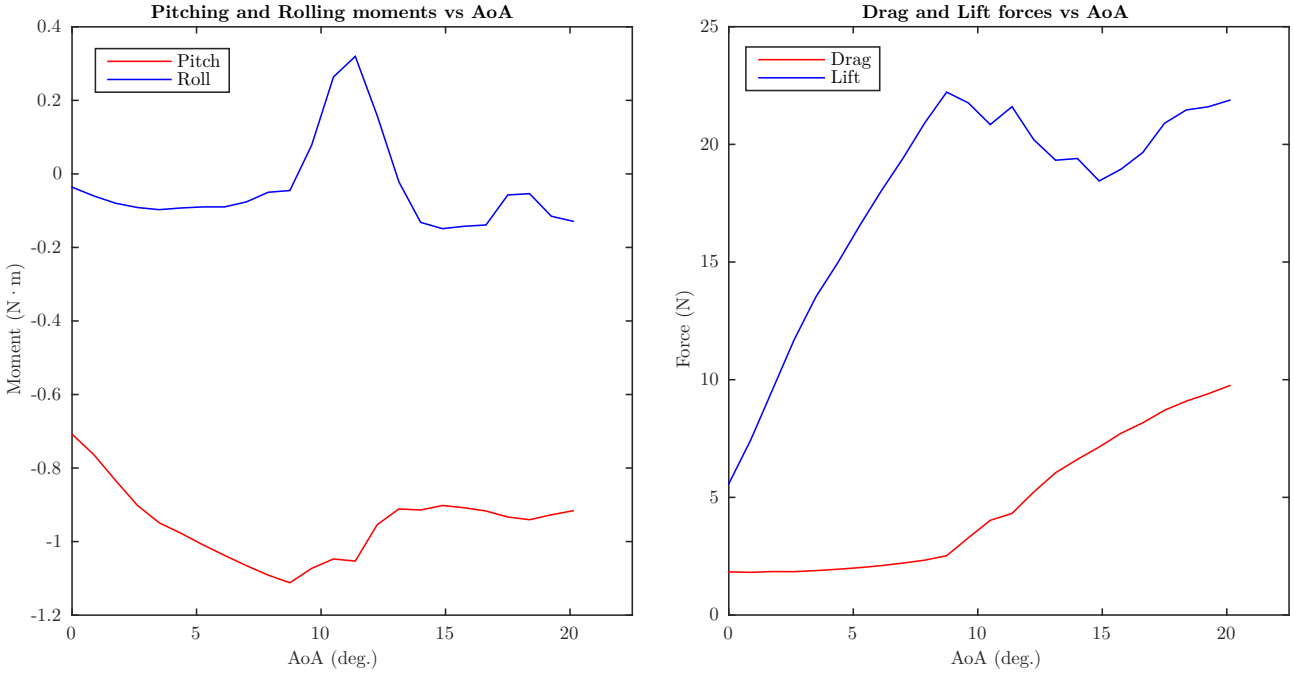

Figure 7.4: Averaged moments and forces in the range of AoA.

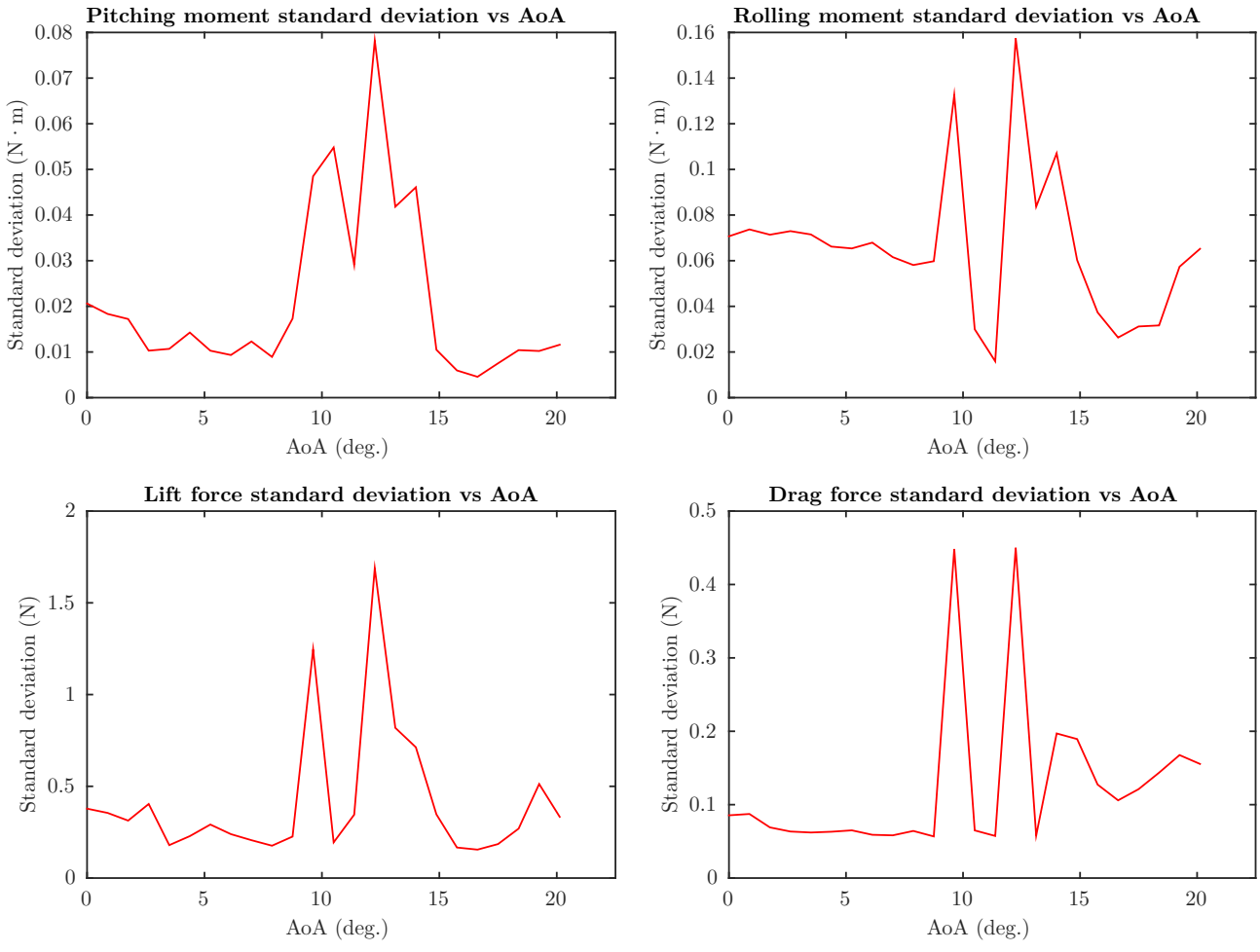

Figure 7.5: Standard deviations for both forces and moments.

Figure 7.5 shows how the standard deviation increases considerably after stall, having two peaks at about $\alpha = 9^{o}$ and at $\alpha = 12.5^{o}$ separated by a valley in all four graphs. This interesting behaviour can also be noticed at figure 7.3, where values seem to join after stall and split again as α increases.

Figures 7.6 and 7.7 show the aerodynamic efficiency and the drag polars respectively. The plot on the left shows the five different records while the averaged is displayed on the right graph. Those two figures have to be compared to the theoretical data shown in figure 7.2.

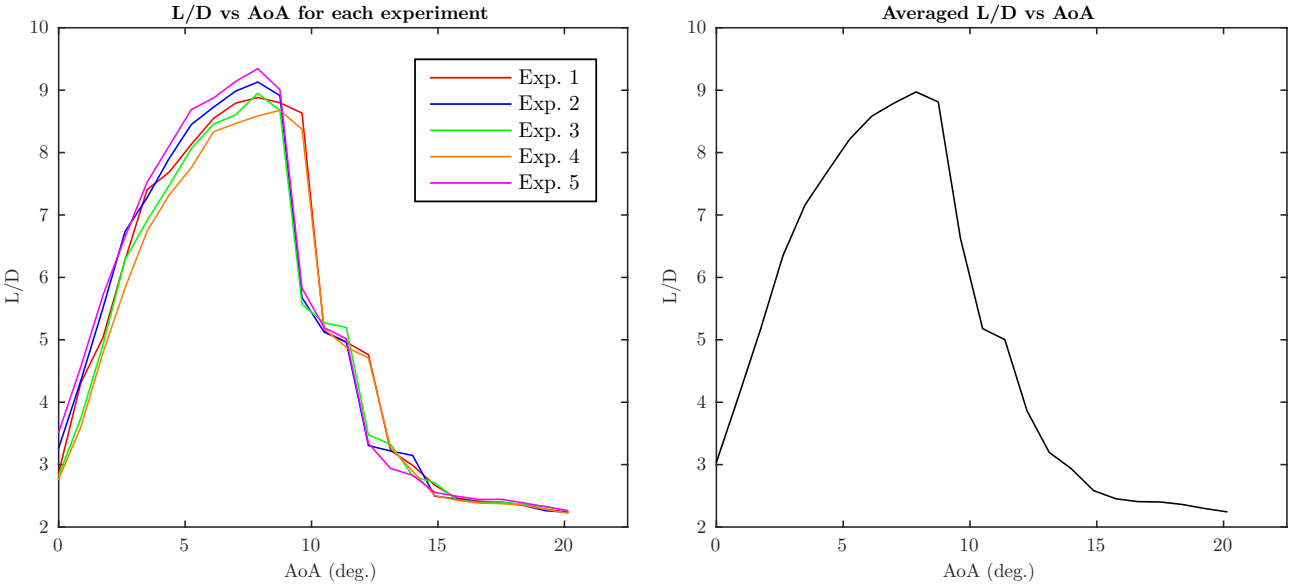

Figure 7.6: L/D curve vs AoA, for each experiment and averaged.

The aerodynamic efficiency, shown in figure 7.6 has its maximum at about $\alpha = 7.5^{o}$. Its value, around 9, is far from the expected, 50. Again, this discrepancy can be explained by the effect of the fuselage and other components being tested. The point at which this maximum is achieved is very close to the expected, about $\alpha = 6^{o}$; the reason of it not being exactly the same might be the 4^{o} inclination of the horizontal tail with respect to the wing.

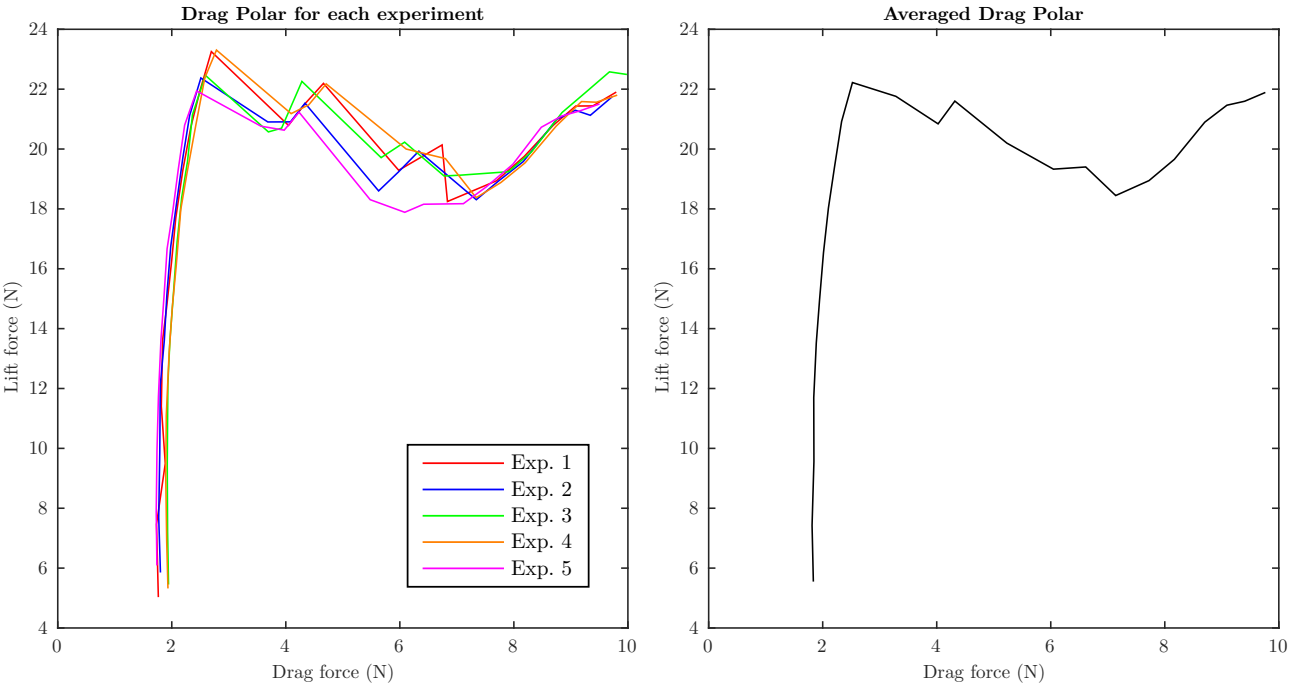

Figure 7.7: Drag polars for each experiment and mean of the drag polar.

Figure 7.7 shows the expected shape. Maybe the fall is more abrupt than the expected one, and there isn't

supposed to be a local minimum after stall. This behaviour is related to the existence of the horizontal tail, shifted 4º with respect to the wing. This tilt makes the horizontal tail to stall after the wing, causing a greater increase in the drag and some additional decrease in the lift force.

7.2 Aileron deflection

In this section, the role of the aileron will be analyzed and, in particular, its ability to generate rolling moment for different values of α, focusing in the case of stall. One of the claims that have been discussed in the theoretical background of this thesis is that, when flying at stall, the aileron sensitivity decreases drastically, up to the point at which the normalized sensitivity turns negative, see figure 4.2. This would imply that a positive aileron deflection would cause a negative roll moment, making the aircraft controls' behaviour become unpredictable and compromising safety at a big extent. In this section, this effect will be analyzed in the wind tunnel and the corresponding experimental results will be presented.

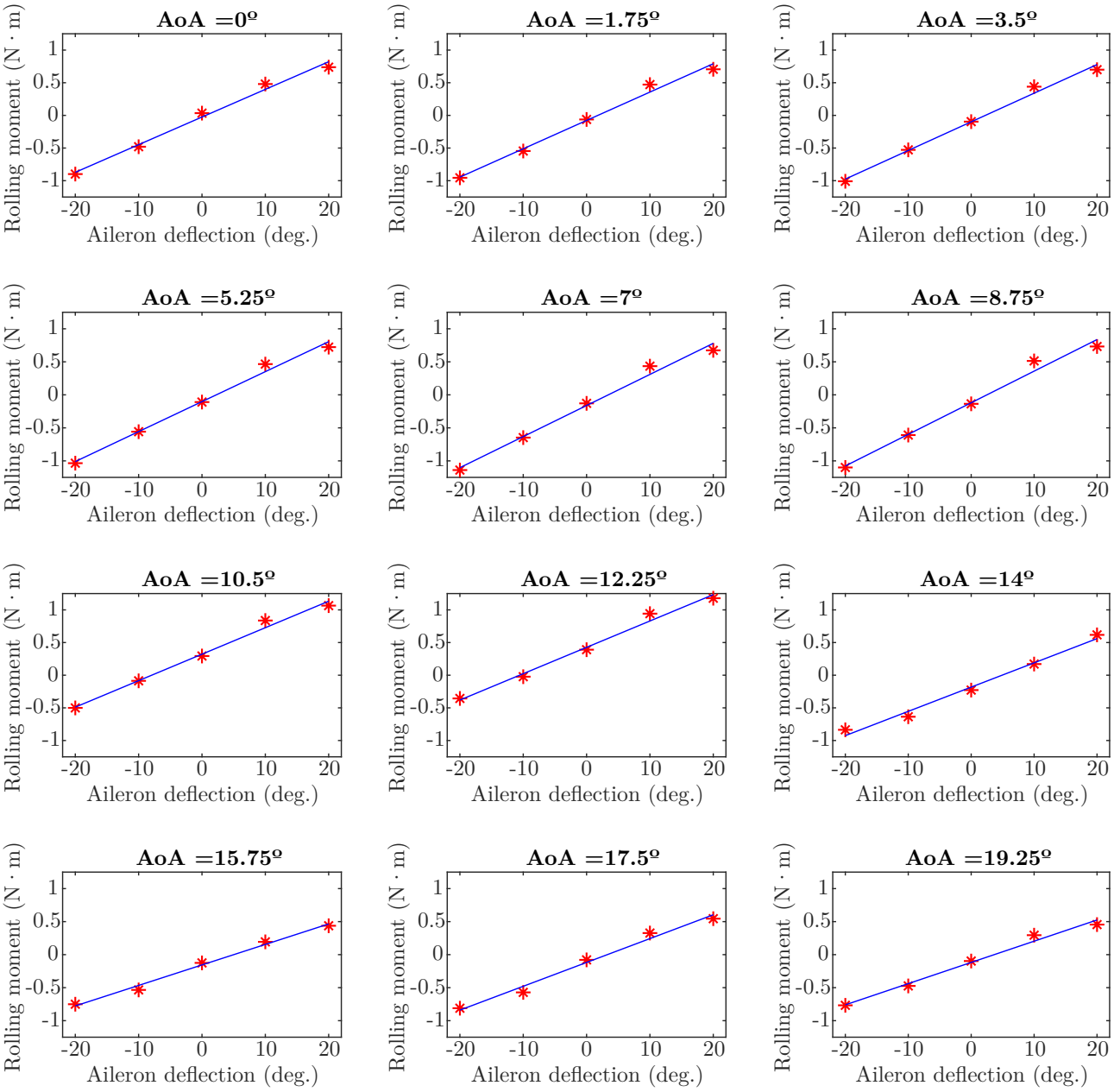

Figure 7.8: Rolling moment induced by the aileron deflection for different AoA.

The main setup of this experiment consists of deflecting the ailerons at 5 different angles ($\delta_a = -20º$, $-10º$, $0º$, $10º$, and $20º$) at different angles of attack, with a spacing of $1.75º$ in this case. The angles of attack range from $0º$ to $19.25º$, far after stall.

Figure 7.8 shows the rolling moments obtained for the different aileron deflections at each of the AoA. They are all scaled the same way in both axes in order for the comparison to be more easily made. Out of the 5 different readings, represented as red stars, there has been made a linear regression in order to determine the slope of the points being plotted, that consists of the sensitivity of the ailerons in the rolling moment. This sensitivity will be shown at figure 7.15 along with the elevator's analogous with respect to the pitching moment.

On the other hand, figure 7.9 shows the rolling moment and the drag force generated with respect to the angle of attack at each aileron deflection. On the left one, we can feel the same asymmetric effect that was already commented on previously, see figure 7.3 upper right. It can be shown, thus, that this effect does not depend on the aileron deflection. The plot on the right shows what we could perfectly expect: when the ailerons are fully deflected, the drag increases for all AoA. Meanwhile, not deflecting the ailerons minimizes the drag force.

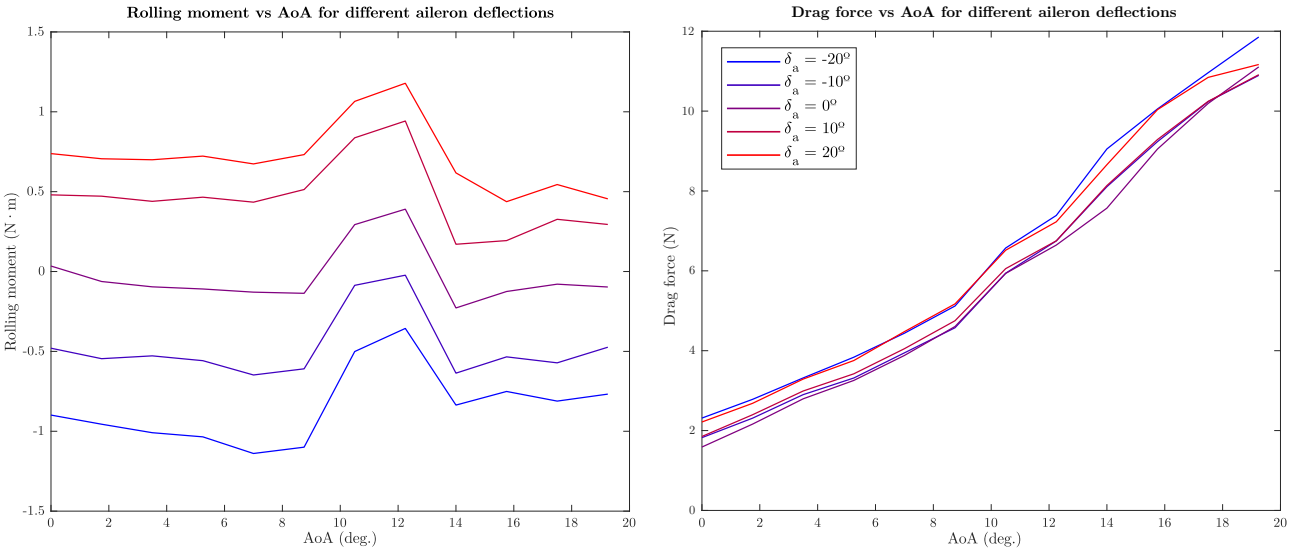

Figure 7.9: Rolling moment and drag force vs AoA for different aileron deflections.

Apart from this setup, an additional one was done as well. It consisted of measuring the rolling moment at each angle of attack when the ailerons were fully deflected, both in the positive and in the negative sense. The experiment was conducted two different times in order to find out if the results were consistent.

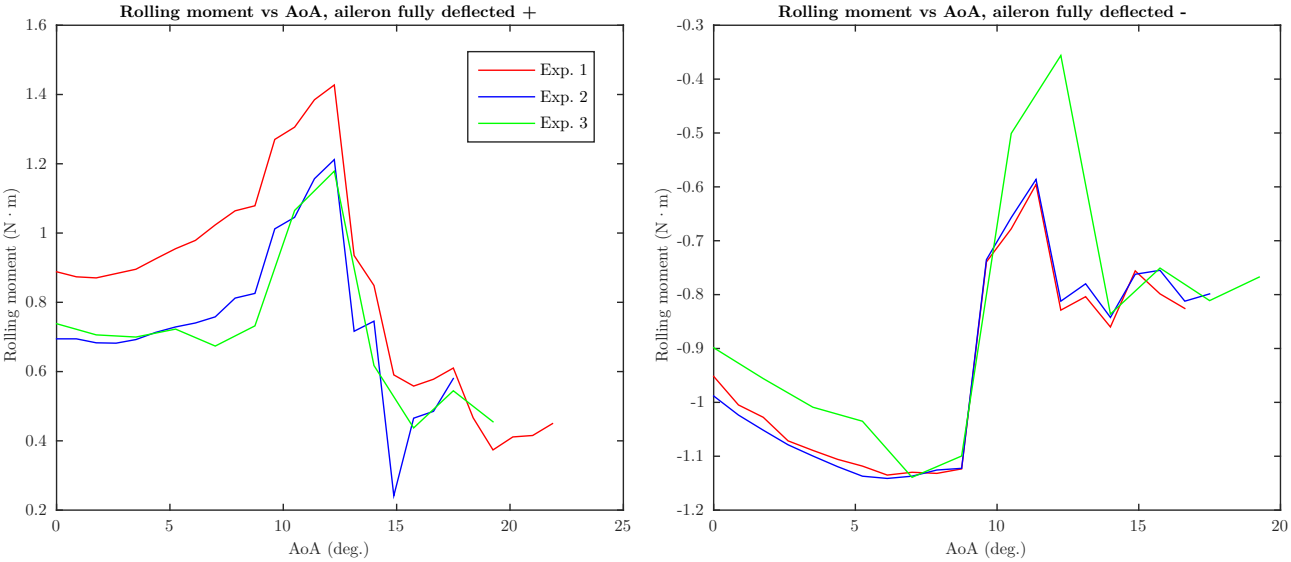

Figure 7.10: Rolling moment induced by the aileron's maximum deflection vs AoA.

Figure 7.10 shows the rolling moment obtained at each deflection: positive on the left and negative on the right. The red and blue lines correspond to the second setup, and their aileron deflections might not have the precise same value as they had in the first setup ($\pm 20^{o}$). Besides, the ranges of AoA might not be the same as in some cases resonant vibrations were encountered.

While some variation is observed, qualitatively all curves show very similar behaviours. The deviation in the reading might be attributed to some sensitivity in the angle of deflection of the ailerons, as it has not been always the same, as already mentioned.

7.3 Elevator deflection

Although it was not the main focus of this thesis, in the third stage of the experimental part the role of the elevator in the generation of pitch moment will be analyzed. The setup is very similar to the one in this last section: observing the pitching moment generated at each of five different elevator deflections for a certain set of AoA. In this case, however the deflections were $\delta_e = -25^o$, -15^o, 0^o, 15^o, and 25^o.

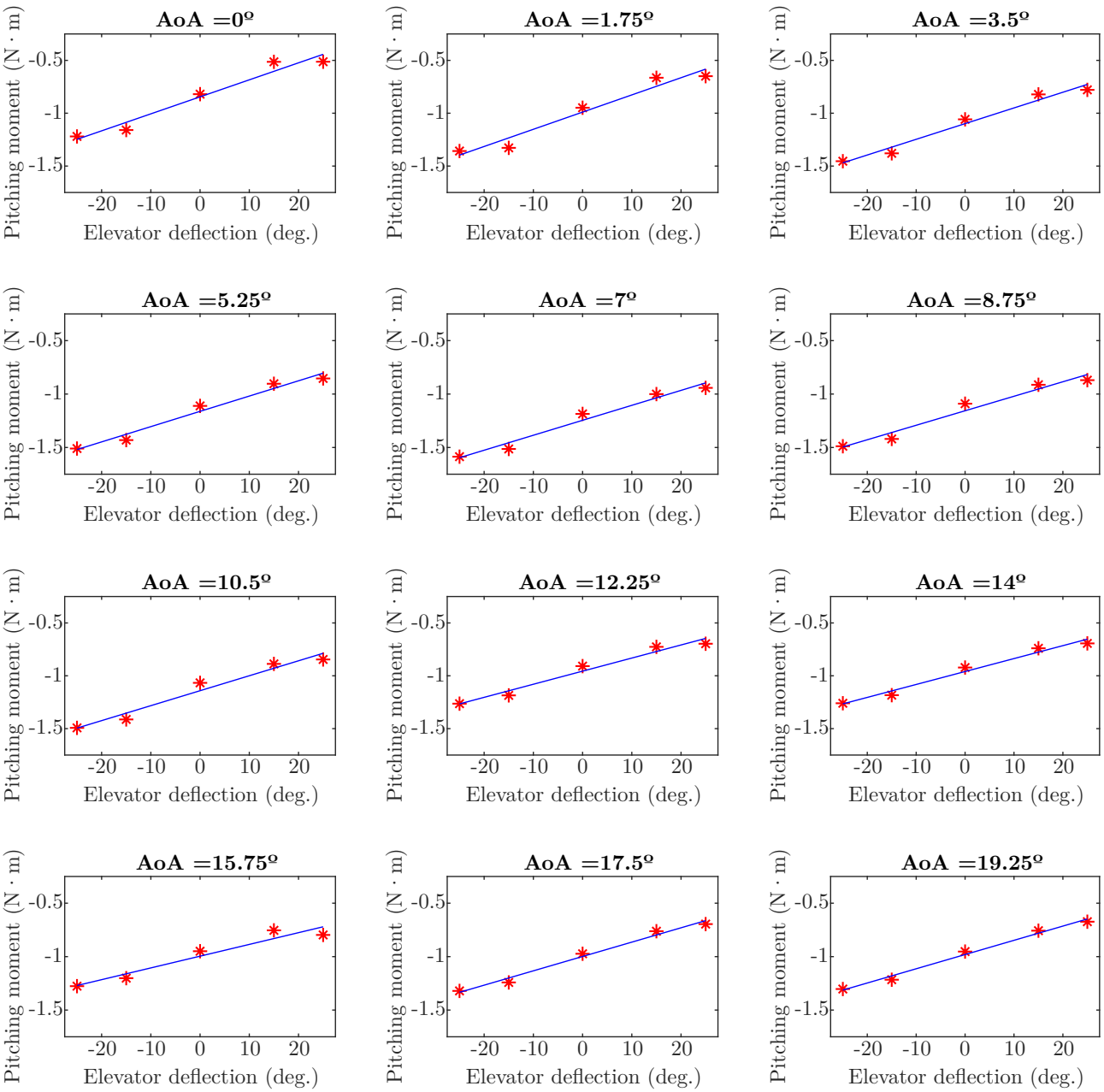

Figure 7.11: Pitching moment induced by the elevator deflection for different AoA.

Figure 7.11 shows the pitching moments at each elevator deflections for all AoA in the range, as red stars. Again, regression lines have been drawn in blue to obtain the sensitivity of the control surface. Qualitatively, it can be observed that all lines have a similar slope, as all graphs are scaled equally.

Note here that the points when the elevator is half deflected (corresponding to $\delta_e = \pm 15^o$) are usually a little bit displaced from the regression line. This might be due to the fact that the elevator's deflections were measured when the wind tunnel was off and the effect of the airflow hitting the control surfaces might have reduced to a

certain extent the full deflection, slightly distorting the graph. As this interference affects equally regardless of the AoA, we will neglect it in our comparison.

As before, we did also focus in the evolution of the pitching moment with respect to the AoA and the drag induced in each case. Figure 7.12 shows this features. From the plot in the left, we can observe that the pitching moment increases in magnitude until stall, when it decreases softly before keeping almost constant from about $\alpha = 12^{o}$ on (see the red curve in the left graph of figure 7.4, that shows the same behaviour when there is no aileron deflection). The plot in the left, on the other hand shows how the minimum drag force is obtained when the elevator is not deflected at all.

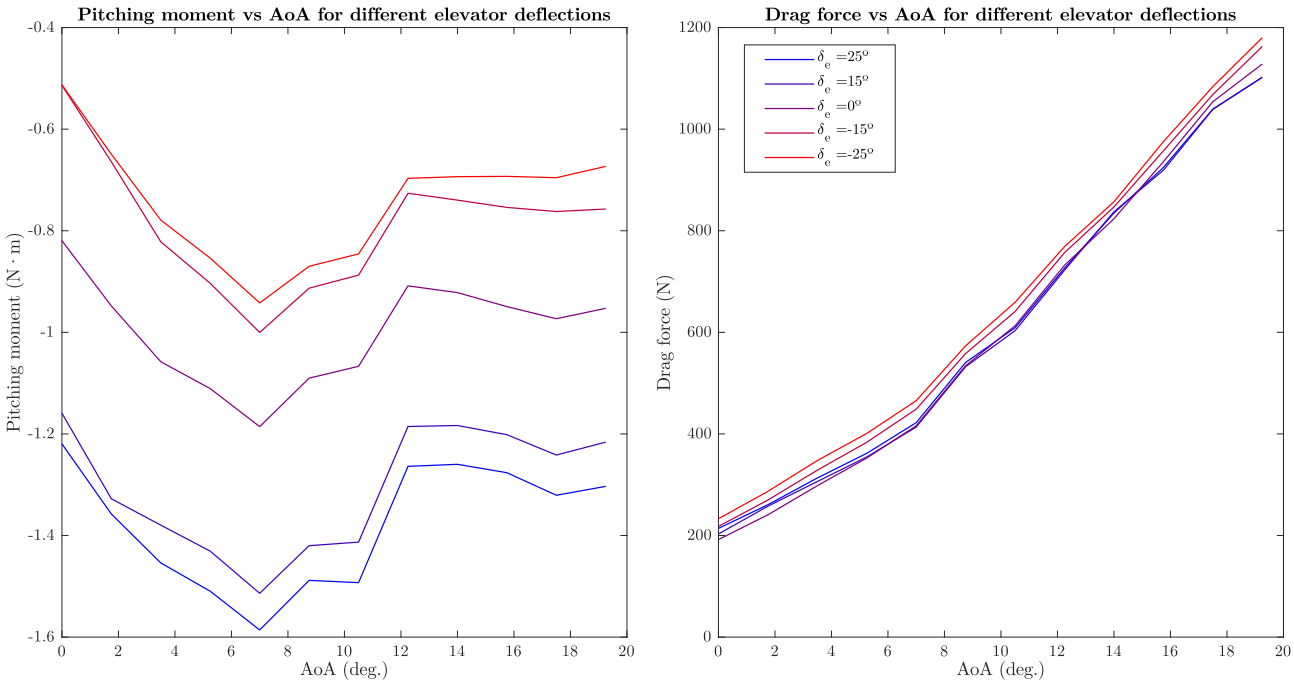

Figure 7.12: Pitching moment and drag force vs AoA for different elevator deflections.

Again, an additional experiment was conducted in order to observe the forces and moments acting on the aircraft with fully deflected elevators. The data was gathered in different days with very similar air conditions.

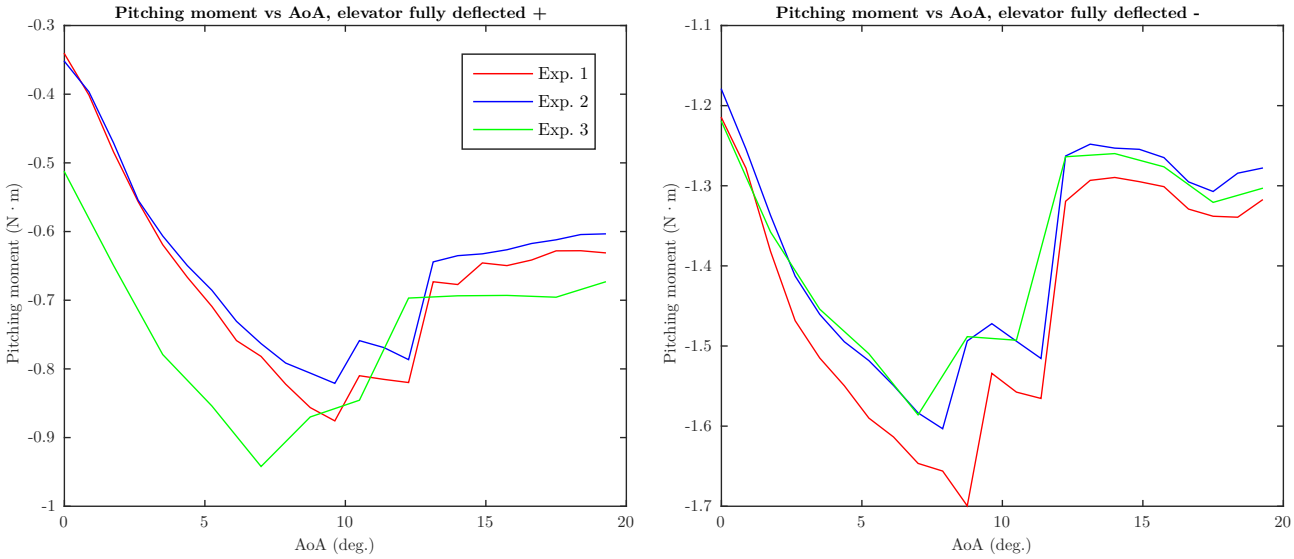

Figure 7.13: Pitching moment induced by the elevator's maximum deflection vs AoA.

Figure 7.13 shows such results, being the green line the one obtained in the original setup. As it happened in the previous case, results show consistency and all curves have similar shapes: they all show an almost constant increase in absolute value before stall, a decrease after stall and an almost constant value in the end.

7.4 Aileron and elevator comparison

In this section, the two previous stages will be analyzed together, comparing them to the zero deflection case. In all cases, the presented results are the averaged values of as many experiments as there have been of each kind, in order to show precise values for all the curves.

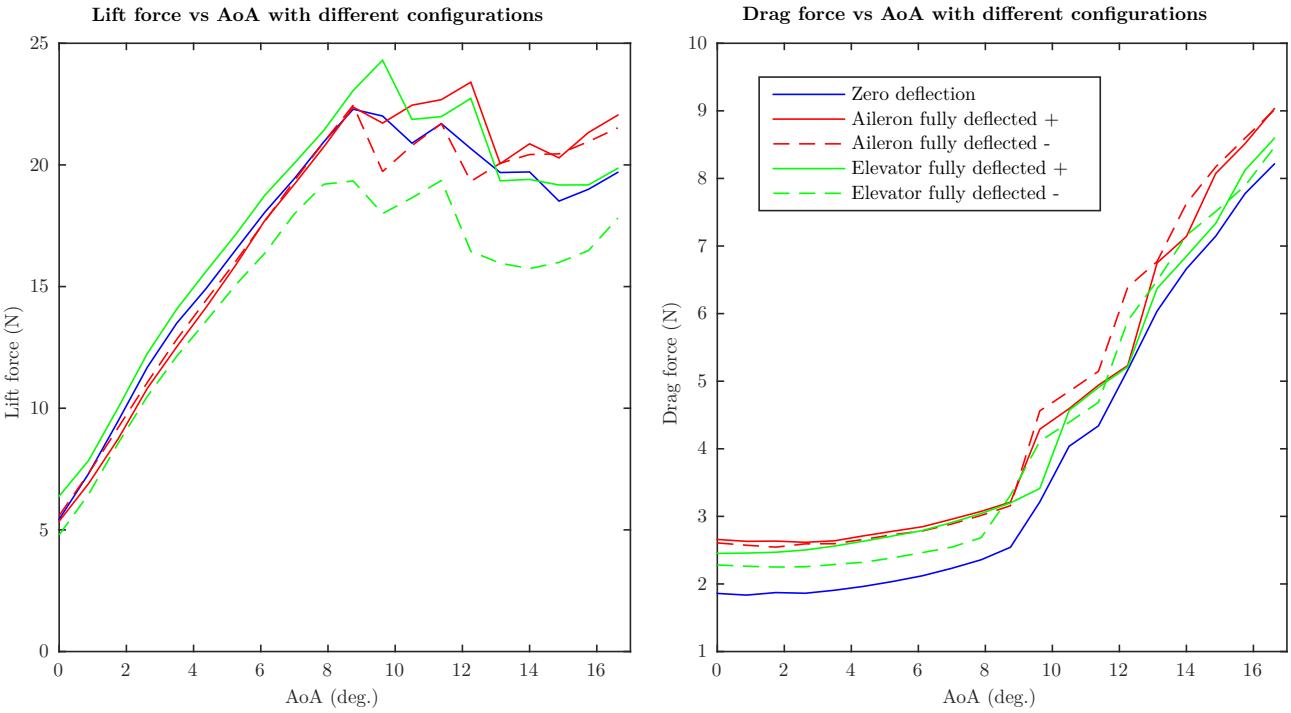

Figure 7.14: Lift and drag forces under different configurations vs AoA.

Figure 7.14 shows, on the one hand, the lift and drag curves with respect to the AoA. In both cases the blue line represents the zero-deflection case, while the red line corresponds to the aileron deflection and the green one is the elevator deflection. From the plot on the left, we can see that in most cases, the lift is reduced when deflecting control surfaces. Only in the case of positive elevator deflection there is an increase in the lift force, as the horizontal increases its effective angle of attack generating extra lift. Nevertheless, this increase in the lift force is compensated by an increase in the drag force, making it less aerodynamically efficient: the L/D value will probably be worse than the zero deflection case. In all the rest of configurations, the drag force is greater than in the reference case.

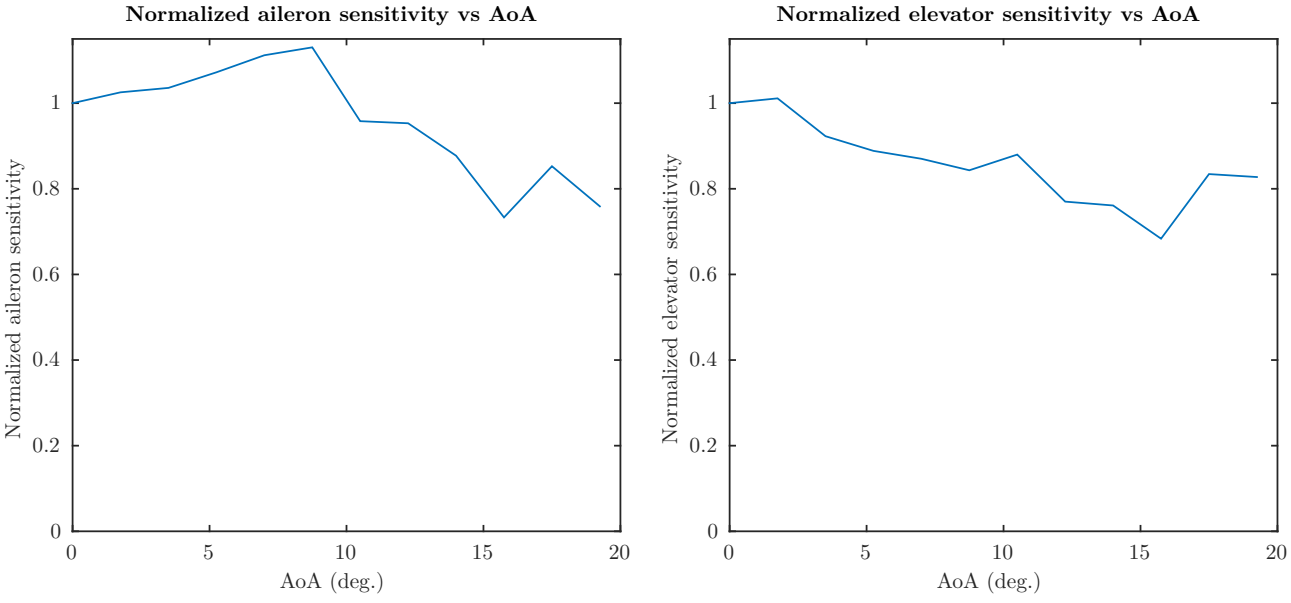

Figure 7.15: Control surfaces sensitivity vs AoA.

Figure 7.15 shows a very important aspect: the sensitivity of the control surfaces with respect to their corresponding moments against the angle of attack. In other words: it shows the ability of the different control surfaces, namely the ailerons and the elevators, to generate their corresponding moments, that is to say the rolling and pitching moments respectively.

The expected behaviour of the first of them has been already discussed in the theoretical background of this thesis. The results gathered in the second stage of the present experimental part appear to be in contradiction with this expected behaviour. Not only they don't show a decrease in the aileron sensitivity before stall, but they keep the same sign for all the range of AoA. Nevertheless, there is indeed a change in the evolution of the aileron sensitivity when the aircraft enters stall: it stops increasing and decreases with a big slope. In the conclusions section, how this slope might encourage further research on the LIBRA mechanism will be discussed.

The normalized elevator sensitivity is shown on the right plot of the same figure. Unlike the previous case, this one has a very similar decrease rate in the whole domain considered. In this case, as before, we can not talk of loss of control capabilities at stall as it has a normalized value of 0.8.

7.5 Different Reynolds numbers

In order to complement the experiments made so far, in this last section we will analyze the behaviour of forces and moments acting on the aircraft model with different Reynolds numbers: namely with different velocities. It would have been of special interest using higher velocities, as the Reynolds number would have approached more the one that is given in civil aviation flights, ranging from 500 000 to 1 million. However, due to the wind tunnel capabilities, we've had to work with lower airspeeds.

Velocities used have been 9.3, 16, 19.2 and 25 m/s, matching the to different RPMs of the wind tunnel. Those velocities correspond to the Reynolds numbers 55k, 93k, 111k and 145k, considering the same chord and air characteristics used in the previous stages. This range of Reynolds numbers are considered to be low in flight dynamics wind tunnel testing.

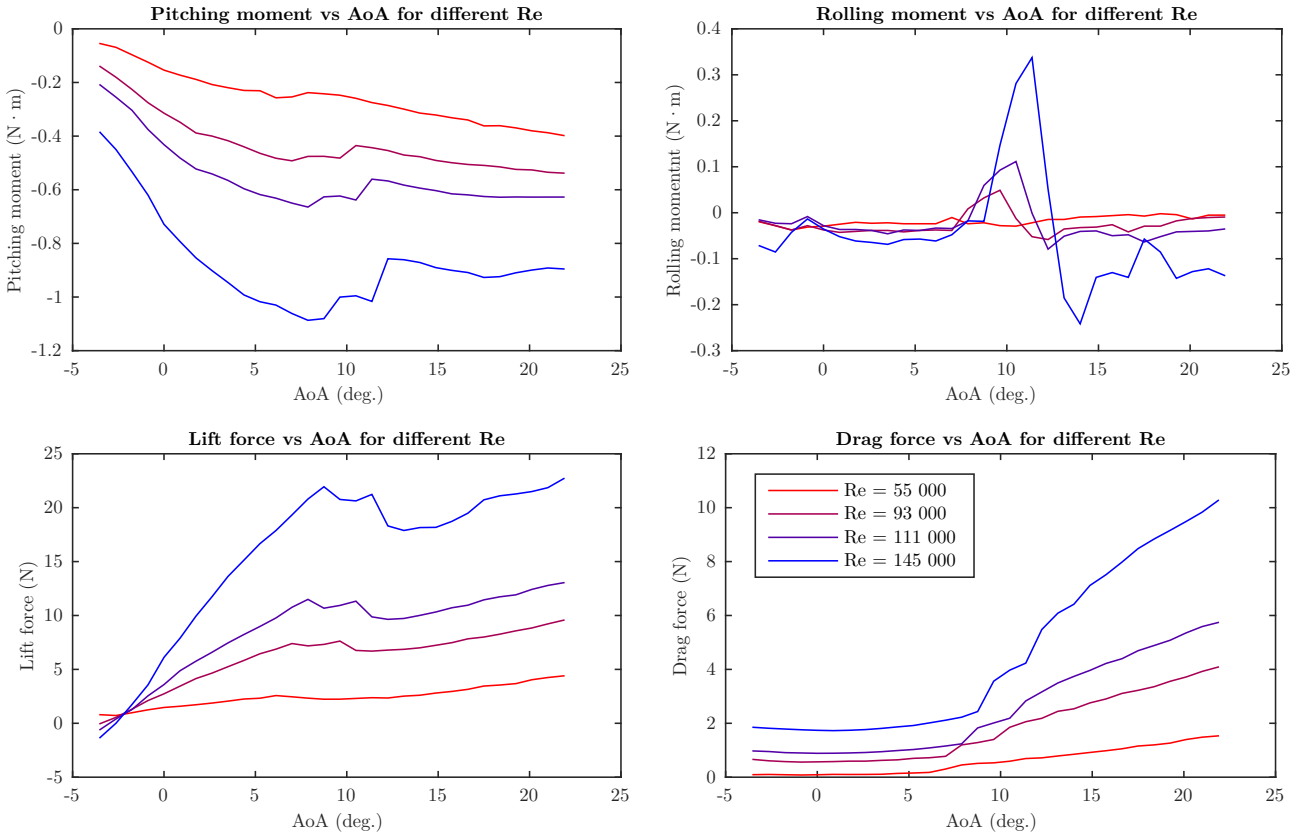

Figure 7.16: Moments and forces for different Reynolds numbers.

Figure 7.16 shows the obtained data as moments and forces. Note here that the range of AoA has been extended to negative values in order to show the point at which there is no Lift force. As expected, as velocity goes down, forces and moments approach the x-axis in all four plots, as forces and moments are zero, for all AoA, if the

velocity is zero; except for the pitching moment, that would show the effect of the CG moving horizontally with respect to the mount. Leaving this apart, results make sense: the lift force grows with a higher slope as Re increases and the drag force is also greater with greater values of Re: they are both proportional to square of the velocity. Finally, the rolling moment asymmetric peak at stall, described above, vanishes as the velocity decreases.

In order to compare more easily the accuracy of this experiment, we've converted the forces and moments to dimensionless coefficients to make them be independent of velocity. The transformations for the moments are the ones that follow:

$$C_m = \frac{M}{(1/2)\rho\,\bar{c}\,U_\infty^2} \qquad\qquad C_{\mathcal{L}} = \frac{\mathcal{L}}{(1/2)\rho\,b\,U_\infty^2}$$

where $\bar{c}$ is the average chord and b is the wing span. For the forces' coefficients, we've applied:

$$C_L = \frac{L}{(1/2)\rho\,S\,U_\infty^2} \qquad\qquad C_D = \frac{D}{(1/2)\rho\,S\,U_\infty^2}$$

being S the wings' total surface. Figure 7.17 shows the dimensionless coefficients. It is clearly shown that the lowest velocity case doesn't provide accurate readings for most of the features measures throughout the AoA range, as it has a very low Reynolds number. The rest of the cases show very close values, with a certain error margin. This error is related to a low precision in the velocities used, as they haven't been measured -their value has been taken from a table of correspondence rpm-airspeed- and they have a quadratic relationship with the dimensionless coefficients.

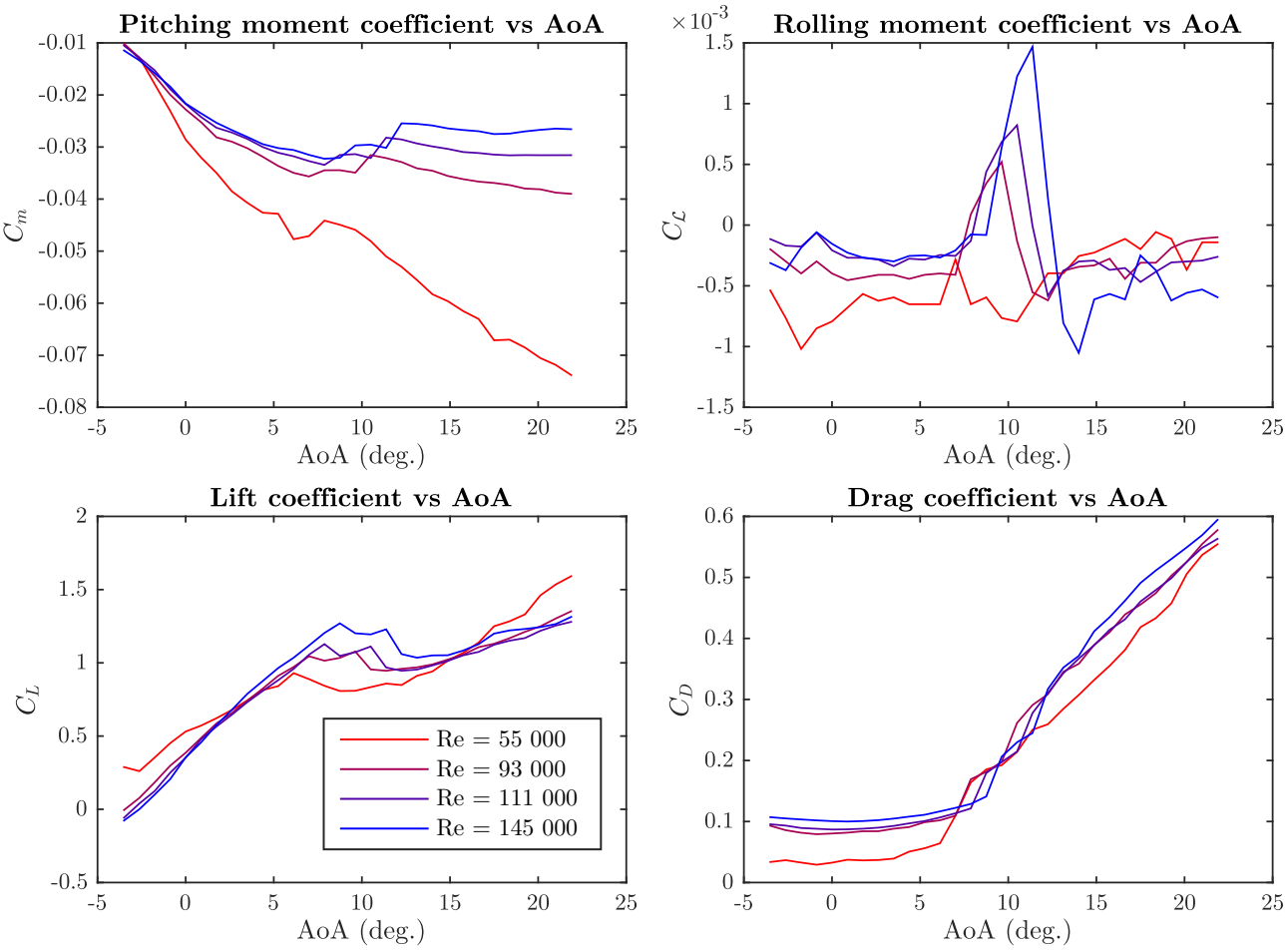

Figure 7.17: Moments and forces dimensionless coefficients for different Reynolds numbers.

Chapter 8

Conclusions

To begin with, and in view of the results, we can conclude that the load cell system designed has a good accuracy in the obtainment of the forces and moments acting on an aircraft. The different figures show the aerodynamic behaviour that was expected, in general terms, and point out unpredictable phenomena that will have to be analyzed.

Apart from the accuracy, the load cell system has proven to have high precision, as results have shown consistency through the different experiments that have been repeated several times. The variation around the mean has been very low, specially in the forces. Those two features imply that the load cell system devised is a good tool in the measurement of forces and moments acting on a body tested in a wind tunnel.

Due to the instability caused by the separation of the flow from the airfoil, stall has presented a higher order of error than the linear regime. Actually two different peaks, separated by a valley have been noticed in the standard deviation figure, the first of them corresponding to the critical AoA.

Another phenomenon that has been observed is the shape of the rolling moment with respect to the AoA. An unexpected peak appears after tall, regardless of the aileron's deflection. This asymmetric behaviour has surprised us, as so far we had assumed that the aircraft model was symmetric. Three different possible causes can be listed:

- Imbalance in the geometry. It can be from the aircraft model, from the mount or from the load cell system itself. Also it can be the effect of the wires coming out from the aircraft tensing at a specific AoA and generating an asymmetric extra stress.
- Error in the model. Not accounting for a well defined effect occurring at stall. Less probable.
- The described effect might not be due to an error but can be an aerodynamic effect inherent to stall. Further and independent research might clarify if this is the case.

One of the main conclusions of this research is that there is not a significant loss in the control capabilities of the ailerons when flying at stall; while it is true that there is an important slope in the evolution of the sensitivity with respect to the AoA, that encourages to continue with the following phases of the LIBRA project. The unconventional mechanism could be giving a greater rolling moment at stall, specially if high frequencies and amplitudes can be attained.

Additionally, the elevator sensitivity shows a very similar behaviour showing a very small reduction in the control capabilities.

Finally, from the experiments conducted at different velocities, we can conclude that the higher the Reynolds number we have, the more accurate results will be. We've noticed this effect mainly from the low velocity curves, that showed a big discrepancy with the other curves.

8.1 Future work

Before continuing with the following phase of this project, several improvements of this first phase will be suggested, as there are some misalignments that have been detected in the design that could be generating error.

The main correction that should be added in the design is the use of metallic aluminum plates instead of the HDPE ones that we are using currently, as it has been described in the Design section. The use of the very

same material that the load cells are made of would standardize the whole design making everywhere to have the same thermal diffusion coefficient and other material characteristics.

An additional enhancement that should be made is the application of wind tunnel corrections. The first of them would be running the whole experiment without the aircraft model to then subtract the previously obtained results to the new ones, getting rid of effects of the mount and plate. Additionally, other corrections can be apply, like the role of the ceiling and walls or the changes in temperature, just to name a few. Such corrections are standardized and can be found in books. Further repetitions of the experiments should be done at the maximum Reynolds number achievable.

Once the first phase is finalized, phases 2 and 3 will follow. The aircraft model will have to be redesign from scratch, keeping the exact same outer shape and geometry, in order to make room for the new mechanism that will be able to implement the control input required for LIBRA. This mechanism will have to guarantee a phase shift of exactly $90^{\underline{o}}$ providing the maximum possible frequency in the oscillations. This will be an engineering challenge.

In parallel to what has been mentioned, two different publications will be released, the first of them concerning the design and manufacturing of multi-axis load cell systems and the second one showing the results obtained in phase 1. In the first publication, we will describe in detail how to fabricate different designs of load cell systems, showing all the important aspects to consider and introducing a new design that extends the current one to 5 axes. In the second one, we will show the results that we've obtained, applying the enhancements and corrections that have been just mentioned.

Bibliography

[1] Fernández-Cara, E. & Zuazua, E. *Control Theory: History, Mathematical Achievements and Perspectives.*, Departamento de Ecuaciones Diferenciales y Análisis Numérico, Universidad de Sevilla | Bol. Soc. Esp. Mat. Apl. no0 (0000), 1-62

[2] Andrei, Neculai, *Modern Control Theory - A historical perspective*, Research Institute for Informatics, Center for Advanced Modeling and Optimization, 8-10, Averescu Avenue, Bucharest 1, Romania

[3] Rowell, Derek & huang, I.L, *State-Space Representation of LTI Systems*, Analysis and Design of Feedback Control Systems, October 2002.

[4] Guest, Martin, *Introduction to manifolds*, Tokyo, January 2007

[5] Dayton Ellwanger, *Manifolds, Tangent Spaces, Cotangent Spaces, Vector Fields, Flow, Integral Curves*, Notes on Differential Geometry and Lie Groups, Department of Computer and Information Science, University of Pennsylvania, March 2009

[6] J. Isham, Chris, *Modern Differential Geometry for Physicists*, World Scientific Lecture Notes in Physics - vol 61, Second Edition

[7] J. Sussmann, Héctor & Guoqing, Tang, *Shortests Paths for the Reeds-Shepp Car: a Worked Out Example of the Use of Geometric Techniques in Nonlinear Oprimal Control*, Department of Mathematics, Rutgers University, SYCON 91-10, September 1991

[8] Abdelgalil, Mahmoud A. M. *The Trinity of Control Theory*, University of California at Irvine - February, 2019.

[9] Desoky, Mohamad A.A. *Experimental Study on Bio-Inspired Wings with Tubercles*, Faculty of Engineering, Cairo University - Giza, Egypt, 2018

[10] Gómez Tiern, M.A., Pérex Cortés, M. & Puentes Márquez, C., *Mecánica del Vuelo*, Garceta Grupo Editorial, 2ª Edición, Madrid, 2012.

[11] Anderson, David F. & Everhardt, Scott, *Understanding Flight*, McGraw Hill, Second Edition, 2010.

[12] Etkin, Bernard & Duff Reid, Lloyd, *Dynamics of Flight, Stability and Control*, McGraw-Hill, Third Edition, 1996.

[13] Nelson, Robert C., *Aircraft Stability and Automatic Control*, McGraw-Hill, Second edition, 1998.

[14] Schmidt, Louis V., *Introduction to Aircraft Flight Dynamics*, AIAA Education Series, 1998.

[15] Nelson, R.C., *Flight Stability and Automatic Control*, McGraw-Hill, 1989.

[16] Hassan, Ahmed M. & Taha, Haithem E., *Geometric Nonlinear Controllability Analysis for Airplane Flight Dynamics*, University of California, Irvine, CA - AIAA SciTech

[17] Hassan, Ahmed M. & Taha, Haithem E., *Geometric control formulation and nonlinear controllability of airplane flight dynamics*, Springer Science+Business Media Dordrecht 2017

[18] Hassan, Ahmed M. & Taha, Haithem E., *A Novel Airplane Roll Mechanism: Nonlinear Motion Planning Approach*, University of California, Irvine, AIAA SciTech Forum, San Diego, California - 2019.

Part IV

Appendix

Chapter 9

Geometric Control example: parallel parking

In order to better understand the idea of the LIBRA mechanism, in this appendix, a simpler example of increasing the control capabilities in a system by means of Lie brackets will be analyzed: the parallel parking maneuver of a kinetic car. Due to its simplicity, it is very usually the example that is discussed when introducing the generation of new directions of motion.

Geometric control analysis

Figure 9.1 shows the basic notation that will be used in the state space analysis below, showing both states (x_1, x_2 and θ) and the inputs (u_1 and u_2). Figure 9.2 shows the parallel parking a scheme of the problem of parallel parking: motion is needed in a direction to which there is no direct control authority. The green arrow shows the desired motion, that doesn't correspond to the inputs that are provided, the blue and red arrows. In this analysis, we will prove that the green arrow is a Lie product of the blue arrow (used to move forward and back) and the red arrow (the steering of the vehicle).

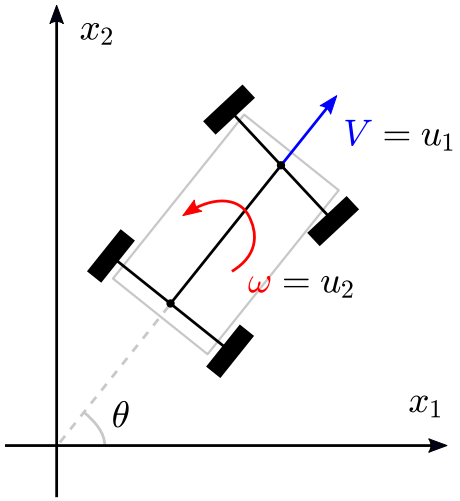

Figure 9.1: Scheme of the kinetic car.

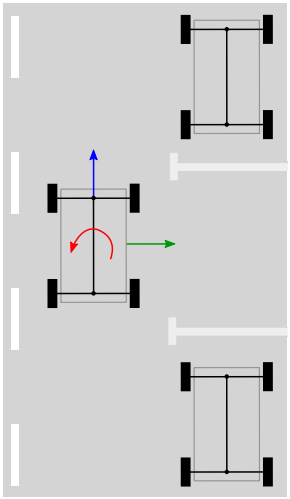

Figure 9.2: Scheme of the parallel parking problem.

The system defined is considered to be driftless, meaning that is drift function $f(x(t))$ is 0 (see eq. 2.29). This basically means that the evolution of the states will not depend on the state at a given time, but will only depend on the control inputs. Considering as inputs $u_1 = V$ and $u_2 = \omega$ and having as states x_1, x_2 and θ, as figure 9.1 suggests, the system will follow the expression:

$$\begin{pmatrix} \dot{x}_1 \\ \dot{x}_2 \\ \dot{\theta} \end{pmatrix} = \underbrace{\begin{pmatrix} \cos\theta \\ \sin\theta \\ 0 \end{pmatrix}}_{g_1} u_1 + \underbrace{\begin{pmatrix} 0 \\ 0 \\ 1 \end{pmatrix}}_{g_2} u_2 \tag{9.1}$$

The compacted g-matrix has rank 2 and three rows, which implies that, with only those two controls there is no full authority in all the states. As in most cases, there aren't as many controls as states, due to the physical complexity of creating additional actuators that could cover the whole rank. In order to try to solve this lack of control, we compute the Lie bracket of the available controls:

$$[g_1,\, g_2] = \frac{\partial g_2}{\partial x} g_1 - \frac{\partial g_1}{\partial x} g_2 = \begin{pmatrix} 0 & 0 & 0 \\ 0 & 0 & 0 \\ 0 & 0 & 0 \end{pmatrix} \cdot \begin{pmatrix} \cos\theta \\ \sin\theta \\ 0 \end{pmatrix} - \begin{pmatrix} 0 & 0 & \sin\theta \\ 0 & 0 & \cos\theta \\ 0 & 0 & 0 \end{pmatrix} \cdot \begin{pmatrix} 0 \\ 0 \\ 1 \end{pmatrix} = \begin{pmatrix} -\sin\theta \\ \cos\theta \\ 0 \end{pmatrix} \tag{9.2}$$

In order to make sure that this vector is always linearly independent with respect to g_1 and g_2, we compute the determinant of the resulting matrix:

$$\det\left(g_1, g_2, [g_1, g_2]\right) = \cos^2\theta - (-\sin^2\theta) = 1, \qquad \forall\,\theta \tag{9.3}$$

As the determinant of this matrix is not 0, the resulting control matrix will be of full rank. Besides, if we consider figure 9.2 above, where $\theta = 90^{\text{o}}$, it is easy to see that the new vector follows the direction of the green arrow, as its value is (1, 0, 0). We have generated a new direction of motion, but how can we move through this arrow? What controls do we have to input to the system?

Motion planning

As already discussed in this thesis, given two vectors X, Y, the flow through its Lie product $[X,\, Y]$ is proportional to the combined flow along X, $-Y$, $-X$ and $-Y$. This means that, in order to move through the green arrow we will have to combine the two controls we have $u_1 = V$ and $u_2 = \omega$ alternating their sign.

Figure 9.3 shows a proposed control history in order to attain motion in the Lie direction. It consists of first moving forward, then steering right, moving backwards and finally steering left. The more this cycle is repeated, the more motion is obtained through this direction. By decreasing the value of ε, the motion is obtained faster.

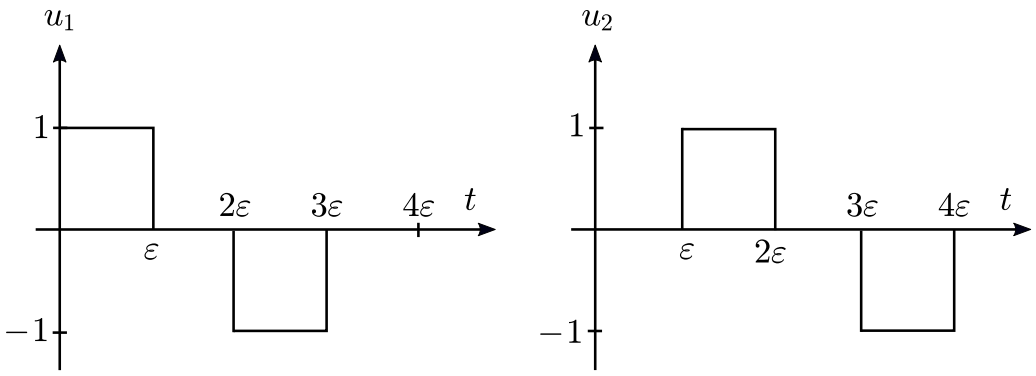

Figure 9.3: Motion planning strategy in order to get motion in not actuated directions.

By means of differential geometry concepts, the system has become nonlinearly controllable. There is a direct analogy between parallel parking and the LIBRA mechanism of rolling at stall: in both cases, motion is needed through a direction in which there is no control authority (due to a lack of actuators in the first case and due to a loss of sensitivity of one of the control surfaces in the second case). By oscillating the value of the available controls with a 90^{o}-phase between them, this lack of control is overcome.

Although making rectangular pulses is the optimal way of achieving this motion in terms of energy, sometimes such sharp inputs will not be able to be produced. This is why, in the LIBRA mechanism, sinusoidal inputs are used instead, as they are much more easier to implement in the small-scale aircraft model that is tested in the wind tunnel.

Chapter 10

First order Lie brackets

In this section, we are reproducing the mathematical expansions of the first order Lie brackets of the drift and the different controls and of the controls themselves, as they appear in the bibliography. In the first section we will recall the different functions and in the second we will present the Lie brackets.

10.1 Drift and control vector fields

After rearranging the equations of motion, the drift vector field $f(x)$ is found which includes the uncontrolled aerodynamic and propulsive loads, as well as the control input vector fields g_i's associated with the four control inputs δ_e; δ_a; δ_r; and δ_t:

$$f(x) = \begin{bmatrix} RV - QW - g\sin\theta + \dfrac{qS\bar{c}QC_{X_Q}(\alpha)}{2mV_T} + \dfrac{qSC_X(\alpha)}{m} + \dfrac{X_{T_0}}{m} \\ -RU + PW + g\sin\phi\cos\theta + \dfrac{qS}{m}C_Y(\beta) + \dfrac{qSbP}{2mV_T}C_{Y_p}(\alpha) + \dfrac{qSbR}{2mV_T}C_{Y_r}(\alpha) \\ QU - PV + g\cos\phi\cos\theta + \dfrac{qS\bar{c}QC_{Z_Q}(\alpha)}{2mV_T} + \dfrac{qSC_Z(\alpha)}{m} + \dfrac{Z_{T_0}}{m} \\ Q(C_1R + C_2P) + C_3\left(qSbC_{\mathcal{L}}(\alpha;\beta) + \dfrac{qSbP}{2V_T}C_{\mathcal{L}P}(\alpha) + \dfrac{qSbR}{2V_T}C_{\mathcal{L}R}(\alpha)\right) \\ +C_4\left(qSbC_N(\alpha;\beta) + \dfrac{qSbP}{2V_T}C_{N_P}(\alpha) + \dfrac{qSbR}{2V_T}C_{N_R}(\alpha)\right) \\ C_5PR - C_6(P^2 - R^2) + C_7\left(qS\bar{c}C_M(\alpha) + \dfrac{qS\bar{c}Q}{2V_T}C_{M_Q}(\alpha) + M_{T_0}\right) \\ Q(C_8P - C_2R) + C_4\left(qSbC_{\mathcal{L}}(\alpha;\beta) + \dfrac{qSbPC_{\mathcal{L}_P}(\alpha)}{2V_T} + \dfrac{qSbRC_{\mathcal{L}_R}(\alpha)}{2V_T}\right) \\ +C_9\left(qSbC_N(\alpha;\beta) + \dfrac{qSbPC_{N_P}(\alpha)}{2V_T} + \dfrac{qSbRC_{N_R}(\alpha)}{2V_T}\right) \\ P + \tan\theta\,(Q\sin\phi + R\cos\phi) \\ Q\cos\phi - R\sin\phi \\ \sec\theta\,(Q\sin\phi + R\cos\phi) \end{bmatrix} \tag{10.1}$$

The control input vector fields are:

$$g_{\delta_e} = \begin{bmatrix} \dfrac{qSC_{X_{\delta_e}}(\alpha)}{m} & 0 & \dfrac{qSC_{Z_{\delta_e}}(\alpha)}{m} & 0 & C_7qS\bar{c}C_{M_{\delta_e}}(\alpha) & 0 & 0 & 0 & 0 \end{bmatrix}^T \tag{10.2}$$

$$g_{\delta_t} = \begin{bmatrix} \dfrac{X_{\delta_t}}{m} & 0 & \dfrac{Z_{\delta_t}}{m} & 0 & C_7M_{\delta_t} & 0 & 0 & 0 & 0 \end{bmatrix}^T \tag{10.3}$$

and:

$$g_{\delta_a} = \begin{bmatrix} 0 \\ \frac{qSC_{Y_{\delta_a}}(\beta)}{m} \\ 0 \\ qSb\left(C_3 C_{\mathcal{L}_{\delta_a}}(\alpha,\beta) + C_4 C_{N_{\delta_a}}(\alpha,\beta)\right) \\ 0 \\ qSb\left(C_4 C_{\mathcal{L}_{\delta_a}}(\alpha,\beta) + C_9 C_{N_{\delta_a}}(\alpha,\beta)\right) \\ 0 \\ 0 \\ 0 \end{bmatrix} \quad (10.4) \qquad g_{\delta_r} = \begin{bmatrix} 0 \\ \frac{qSC_{Y_{\delta_r}}(\beta)}{m} \\ 0 \\ qSb\left(C_3 C_{\mathcal{L}_{\delta_r}}(\alpha,\beta) + C_4 C_{N_{\delta_r}}(\alpha,\beta)\right) \\ 0 \\ qSb\left(C_4 C_{\mathcal{L}_{\delta_r}}(\alpha,\beta) + C_9 C_{N_{\delta_r}}(\alpha,\beta)\right) \\ 0 \\ 0 \\ 0 \end{bmatrix} \quad (10.5)$$

where the state is $x = \begin{bmatrix} u, & v, & w, & p, & q, & r, & \phi, & \theta, & \psi \end{bmatrix}$

10.2 First order Lie brackets

In this section we will present the results that were the motivation for the LIBRA mechanism, also from the bibliography:

$$[f, g_{\delta_a}] =$$

$$\begin{bmatrix} 0 \\ -\frac{q^2S^2C_{Y_{\delta_a}}(\beta)C'_Y(\beta)}{m^2\sqrt{U_0^2+W_0^2}} + \frac{q^2S^2C_Y(\beta)C'_{Y_{\delta_a}}(\beta)}{m^2\sqrt{U_0^2+W_0^2}} - qSb\left(C_3 C_{\mathcal{L}_{\delta_a}}(\alpha,\beta) + C_4 C_{N_{\delta_a}}(\alpha,\beta)\right)\left(W_0 + \frac{qSbC_{Y_p}(\alpha)}{2m\sqrt{U_0^2+W_0^2}}\right) \\ -qSb\left(C_4 C_{\mathcal{L}_{\delta_a}}(\alpha,\beta) + C_9 C_{N_{\delta_a}}(\alpha,\beta)\right)\left(\frac{qSbC_{Y_r}(\alpha)}{2m\sqrt{U_0^2+W_0^2}} - U_0\right) \\ 0 \\ \frac{q^2S^2bC_Y(\beta)}{m}\left(\frac{C_3\frac{\partial C_{\mathcal{L}_{\delta_a}}(\alpha,\beta)}{\partial\beta}}{\sqrt{U_0^2+W_0^2}} + \frac{C_4\frac{\partial C_{N_{\delta_a}}(\alpha,\beta)}{\partial\beta}}{\sqrt{U_0^2+W_0^2}}\right) - \frac{qSC_{Y_{\delta_a}}(\beta)}{m}\left(\frac{C_3 qSb\frac{\partial C_{\mathcal{L}}(\alpha,\beta)}{\partial\beta}}{\sqrt{U_0^2+W_0^2}} + \frac{C_4 qSb\frac{\partial C_N(\alpha,\beta)}{\partial\beta}}{\sqrt{U_0^2+W_0^2}}\right) \\ -qSb\left(C_3 C_{\mathcal{L}_{\delta_a}}(\alpha,\beta) + C_4 C_{N_{\delta_a}}(\alpha,\beta)\right)\left(\frac{C_3 qSbC_{\mathcal{L}_P(\alpha)}}{2\sqrt{U_0^2+W_0^2}} + \frac{C_4 qSbC_{N_P(\alpha)}}{2\sqrt{U_0^2+W_0^2}}\right) + \\ -qSb\left(C_4 C_{\mathcal{L}_{\delta_a}}(\alpha,\beta) + C_9 C_{N_{\delta_a}}(\alpha,\beta)\right)\left(\frac{C_3 qSbC_{\mathcal{L}_R(\alpha)}}{2\sqrt{U_0^2+W_0^2}} + \frac{C_4 qSbC_{N_R(\alpha)}}{2\sqrt{U_0^2+W_0^2}}\right) \\ 0 \\ \frac{q^2S^2bC_Y(\beta)}{m}\left(\frac{C_4\frac{\partial C_{\mathcal{L}_{\delta_a}}(\alpha,\beta)}{\partial\beta}}{\sqrt{U_0^2+W_0^2}} + \frac{C_9\frac{\partial C_{N_{\delta_a}}(\alpha,\beta)}{\partial\beta}}{\sqrt{U_0^2+W_0^2}}\right) - \frac{qSC_{Y_{\delta_a}}(\beta)}{m}\left(\frac{C_4 qSb\frac{\partial C_{\mathcal{L}}(\alpha,\beta)}{\partial\beta}}{\sqrt{U_0^2+W_0^2}} + \frac{C_9 qSb\frac{\partial C_N(\alpha,\beta)}{\partial\beta}}{\sqrt{U_0^2+W_0^2}}\right) \\ -qSb\left(C_3 C_{\mathcal{L}_{\delta_a}}(\alpha,\beta) + C_4 C_{N_{\delta_a}}(\alpha,\beta)\right)\left(\frac{C_4 qSbC_{\mathcal{L}_P(\alpha)}}{2\sqrt{U_0^2+W_0^2}} + \frac{C_9 qSbC_{N_P(\alpha)}}{2\sqrt{U_0^2+W_0^2}}\right) + \\ -qSb\left(C_4 C_{\mathcal{L}_{\delta_a}}(\alpha,\beta) + C_9 C_{N_{\delta_a}}(\alpha,\beta)\right)\left(\frac{C_4 qSbC_{\mathcal{L}_R(\alpha)}}{2\sqrt{U_0^2+W_0^2}} + \frac{C_9 qSbC_{N_R(\alpha)}}{2\sqrt{U_0^2+W_0^2}}\right) \\ -qSb\left(C_3 C_{\mathcal{L}_{\delta_a}}(\alpha,\beta) + C_4 C_{N_{\delta_a}}(\alpha,\beta)\right) - \frac{qSbW_0\left(C_4 C_{\mathcal{L}_{\delta_a}}(\alpha,\beta) + C_9 C_{N_{\delta_a}}(\alpha,\beta)\right)}{U_0} \\ 0 \\ -qSb\sqrt{\frac{W_0^2}{U_0^2}+1}\left(C_4 C_{\mathcal{L}_{\delta_a}}(\alpha,\beta) + C_9 C_{N_{\delta_a}}(\alpha,\beta)\right) \end{bmatrix} \quad (10.6)$$

$$[f, g_{\delta_e}] =$$

$$\begin{bmatrix}
\frac{q^2S^2W_0C_{X_{\delta_e}}(\alpha)C'_X(\alpha)}{m^2U_0^2\left(\frac{W_0^2}{U_0^2}+1\right)} - \frac{q^2S^2C_{Z_{\delta_e}}(\alpha)C'_X(\alpha)}{m^2U_0\left(\frac{W_0^2}{U_0^2}+1\right)} - C_7qS\bar{c}C_{M_{\delta e}}(\alpha)\left(\frac{qS\bar{c}C_{X_Q}(\alpha)}{2m\sqrt{U_0^2+W_0^2}} - W_0\right) \\
0 \\
\frac{q^2S^2W_0C_{X_{\delta_e}}(\alpha)C'_Z(\alpha)}{m^2U_0^2\left(\frac{W_0^2}{U_0^2}+1\right)} - \frac{q^2S^2C_{Z_{\delta_e}}(\alpha)C'_Z(\alpha)}{m^2U_0\left(\frac{W_0^2}{U_0^2}+1\right)} - C_7qS\bar{c}C_{M_{\delta e}}(\alpha)\left(U_0 + \frac{qS\bar{c}C_{Z_Q}(\alpha)}{2m\sqrt{U_0^2+W_0^2}}\right) \\
-\frac{qSC_{Z_{\delta_e}}(\alpha)}{m}\left(\frac{C_3qSb\frac{\partial C_{\mathcal{L}}(\alpha,\beta)}{\partial\alpha}}{U_0\left(\frac{W_0^2}{U_0^2}+1\right)} + \frac{C_4qSb\frac{\partial C_N(\alpha,\beta)}{\partial\alpha}}{U_0\left(\frac{W_0^2}{U_0^2}+1\right)}\right) - \frac{qSC_{X_{\delta_e}}(\alpha)}{m}\left(-\frac{C_3qSbW_0\frac{\partial C_{\mathcal{L}}(\alpha,\beta)}{\partial\alpha}}{U_0^2\left(\frac{W_0^2}{U_0^2}+1\right)} - \frac{C_4qSbW_0\frac{\partial C_N(\alpha,\beta)}{\partial\alpha}}{U_0^2\left(\frac{W_0^2}{U_0^2}+1\right)}\right) \\
\frac{C_7q^2S^2\bar{c}W_0C_{X_{\delta_e}}(\alpha)C'_M(\alpha)}{mU_0^2\left(\frac{W_0^2}{U_0^2}+1\right)} + \frac{C_7^2q^2S^2\bar{c}^2C_{M_{\delta_t}}(\alpha)C_{M_Q}(\alpha)}{2\sqrt{U_0^2+W_0^2}} - \frac{C_7q^2S^2\bar{c}C_{Z_{\delta_e}}(\alpha)C'_M(\alpha)}{mU_0\left(\frac{W_0^2}{U_0^2}+1\right)} \\
-\frac{qSC_{Z_{\delta_e}}(\alpha)}{m}\left(\frac{C_4qSb\frac{\partial C_{\mathcal{L}}(\alpha,\beta)}{\partial\alpha}}{U_0\left(\frac{W_0^2}{U_0^2}+1\right)} + \frac{C_9qSb\frac{\partial C_N(\alpha,\beta)}{\partial\alpha}}{U_0\left(\frac{W_0^2}{U_0^2}+1\right)}\right) - \frac{qSC_{X_{\delta_e}}(\alpha)}{m}\left(-\frac{C_4qSbW_0\frac{\partial C_{\mathcal{L}}(\alpha,\beta)}{\partial\alpha}}{U_0^2\left(\frac{W_0^2}{U_0^2}+1\right)} - \frac{C_9qSbW_0\frac{\partial C_N(\alpha,\beta)}{\partial\alpha}}{U_0^2\left(\frac{W_0^2}{U_0^2}+1\right)}\right) \\
0 \\
-C_7qS\bar{c}C_{M_{\delta e}}(\alpha) \\
0
\end{bmatrix} \tag{10.7}$$

$$[f, g_{\delta_r}] =$$

$$\begin{bmatrix}
0 \\
-\frac{q^2S^2C_{Y_{\delta_r}}(\beta)C'_Y(\beta)}{m^2\sqrt{U_0^2+W_0^2}} + \frac{q^2S^2C_Y(\beta)C'_{Y_r}(\beta)}{m^2\sqrt{U_0^2+W_0^2}} - qSb\left(C_3C_{\mathcal{L}_{\delta_r}}(\alpha,\beta) + C_4C_{N_{\delta_r}}(\alpha,\beta)\right)\left(W_0 + \frac{qSbC_{Y_p}(\alpha)}{2m\sqrt{U_0^2+W_0^2}}\right) \\
-qSb\left(C_4C_{\mathcal{L}_{\delta_r}}(\alpha,\beta) + C_9C_{N_{\delta_r}}(\alpha,\beta)\right)\left(\frac{qSbC_{Y_r}(\alpha)}{2m\sqrt{U_0^2+W_0^2}} - U_0\right) \\
0 \\
\frac{q^2S^2bC_Y(\beta)}{m}\left(\frac{C_3\frac{\partial C_{\mathcal{L}_{\delta_r}}(\alpha,\beta)}{\partial\beta}}{\sqrt{U_0^2+W_0^2}} + \frac{C_4\frac{\partial C_{N_{\delta_r}}(\alpha,\beta)}{\partial\beta}}{\sqrt{U_0^2+W_0^2}}\right) - \frac{qSC_{Y_{\delta_r}}(\beta)}{m}\left(\frac{C_3qSb\frac{\partial C_{\mathcal{L}}(\alpha,\beta)}{\partial\beta}}{\sqrt{U_0^2+W_0^2}} + \frac{C_4qSb\frac{\partial C_N(\alpha,\beta)}{\partial\beta}}{\sqrt{U_0^2+W_0^2}}\right) \\
-qSb\left(C_3C_{\mathcal{L}_{\delta_r}}(\alpha,\beta) + C_4C_{N_{\delta_r}}(\alpha,\beta)\right)\left(\frac{C_3qSbC_{\mathcal{L}_{P(\alpha)}}}{2\sqrt{U_0^2+W_0^2}} + \frac{C_4qSbC_{N_{P(\alpha)}}}{2\sqrt{U_0^2+W_0^2}}\right) + \\
-qSb\left(C_4C_{\mathcal{L}_{\delta_r}}(\alpha,\beta) + C_9C_{N_{\delta_r}}(\alpha,\beta)\right)\left(\frac{C_3qSbC_{\mathcal{L}_{R(\alpha)}}}{2\sqrt{U_0^2+W_0^2}} + \frac{C_4qSbC_{N_{R(\alpha)}}}{2\sqrt{U_0^2+W_0^2}}\right) \\
0 \\
\frac{q^2S^2bC_Y(\beta)}{m}\left(\frac{C_4\frac{\partial C_{\mathcal{L}_{\delta_r}}(\alpha,\beta)}{\partial\beta}}{\sqrt{U_0^2+W_0^2}} + \frac{C_9\frac{\partial C_{N_{\delta_r}}(\alpha,\beta)}{\partial\beta}}{\sqrt{U_0^2+W_0^2}}\right) - \frac{qSC_{Y_{\delta_r}}(\beta)}{m}\left(\frac{C_4qSb\frac{\partial C_{\mathcal{L}}(\alpha,\beta)}{\partial\beta}}{\sqrt{U_0^2+W_0^2}} + \frac{C_9qSb\frac{\partial C_N(\alpha,\beta)}{\partial\beta}}{\sqrt{U_0^2+W_0^2}}\right) \\
-qSb\left(C_3C_{\mathcal{L}_{\delta_r}}(\alpha,\beta) + C_4C_{N_{\delta_r}}(\alpha,\beta)\right)\left(\frac{C_4qSbC_{\mathcal{L}_{P(\alpha)}}}{2\sqrt{U_0^2+W_0^2}} + \frac{C_9qSbC_{N_{P(\alpha)}}}{2\sqrt{U_0^2+W_0^2}}\right) + \\
-qSb\left(C_4C_{\mathcal{L}_{\delta_r}}(\alpha,\beta) + C_9C_{N_{\delta_r}}(\alpha,\beta)\right)\left(\frac{C_4qSbC_{\mathcal{L}_{R(\alpha)}}}{2\sqrt{U_0^2+W_0^2}} + \frac{C_9qSbC_{N_{R(\alpha)}}}{2\sqrt{U_0^2+W_0^2}}\right) \\
-qSb\left(C_3C_{\mathcal{L}_{\delta_r}}(\alpha,\beta) + C_4C_{N_{\delta_r}}(\alpha,\beta)\right) - \frac{qSbW_0\left(C_4C_{\mathcal{L}_{\delta_r}}(\alpha,\beta) + C_9C_{N_{\delta_r}}(\alpha,\beta)\right)}{U_0} \\
0 \\
-qSb\sqrt{\frac{W_0^2}{U_0^2}+1}\left(C_4C_{\mathcal{L}_{\delta_r}}(\alpha,\beta) + C_9C_{N_{\delta_r}}(\alpha,\beta)\right)
\end{bmatrix} \tag{10.8}$$

$$[f, g_{\delta_t}] =$$

$$\begin{bmatrix} -C_7 M_{\delta_t}\left(\frac{qS\bar{c}C_{X_Q}(\alpha)}{2m\sqrt{U_0^2+W_0^2}} - W_0\right) + \frac{qSW_0X_{\delta_t}C'_X(\alpha)}{m^2U_0^2\left(\frac{W_0^2}{U_0^2}+1\right)} - \frac{qSZ_{\delta_t}C'_X(\alpha)}{m^2U_0^2\left(\frac{W_0^2}{U_0^2}+1\right)} \\ 0 \\ -C_7 M_{\delta_t}\left(\frac{qS\bar{c}C_{Z_Q}(\alpha)}{2m\sqrt{U_0^2+W_0^2}} - U_0\right) + \frac{qSW_0X_{\delta_t}C'_Z(\alpha)}{m^2U_0^2\left(\frac{W_0^2}{U_0^2}+1\right)} - \frac{qSZ_{\delta_t}C'_Z(\alpha)}{m^2U_0^2\left(\frac{W_0^2}{U_0^2}+1\right)} \\ -\frac{X_{\delta_t}}{m}\left(-\frac{C_3qSbW_0\frac{\partial C_{\mathcal{L}}(\alpha,\beta)}{\partial\alpha}}{U_0^2\left(\frac{W_0^2}{U_0^2}+1\right)} - \frac{C_4qSbW_0\frac{\partial C_N(\alpha,\beta)}{\partial\alpha}}{U_0^2\left(\frac{W_0^2}{U_0^2}+1\right)}\right) - \frac{Z_{\delta_t}}{m}\left(-\frac{C_3qSb\frac{\partial C_{\mathcal{L}}(\alpha,\beta)}{\partial\alpha}}{U_0\left(\frac{W_0^2}{U_0^2}+1\right)} - \frac{C_4qSb\frac{\partial C_N(\alpha,\beta)}{\partial\alpha}}{U_0\left(\frac{W_0^2}{U_0^2}+1\right)}\right) \\ -\frac{C_7^2qS\bar{c}M_{\delta_t}C_{M_Q}(\alpha)}{2\sqrt{U_0^2+W_0^2}} + \frac{C_7qS\bar{c}W_0X_{\delta_t}C'_M(\alpha)}{mU_0^2\left(\frac{W_0^2}{U_0^2}+1\right)} - \frac{C_7qS\bar{c}Z_{\delta_t}C'_M(\alpha)}{mU_0\left(\frac{W_0^2}{U_0^2}+1\right)} \\ -\frac{X_{\delta_t}}{m}\left(-\frac{C_4qSbW_0\frac{\partial C_{\mathcal{L}}(\alpha,\beta)}{\partial\alpha}}{U_0^2\left(\frac{W_0^2}{U_0^2}+1\right)} - \frac{C_9qSbW_0\frac{\partial C_N(\alpha,\beta)}{\partial\alpha}}{U_0^2\left(\frac{W_0^2}{U_0^2}+1\right)}\right) - \frac{Z_{\delta_t}}{m}\left(-\frac{C_4qSb\frac{\partial C_{\mathcal{L}}(\alpha,\beta)}{\partial\alpha}}{U_0\left(\frac{W_0^2}{U_0^2}+1\right)} - \frac{C_9qSb\frac{\partial C_N(\alpha,\beta)}{\partial\alpha}}{U_0\left(\frac{W_0^2}{U_0^2}+1\right)}\right) \\ 0 \\ -C_7 M_{\delta_t} \\ 0 \end{bmatrix} \tag{10.9}$$

$$[g_{\delta_e}, g_{\delta_a}] =$$

$$\begin{bmatrix} 0 \\ 0 \\ 0 \\ \frac{q^2S^2bC_{X_{\delta_e}}(\alpha)}{m}\left(-\frac{C_3W_0\frac{\partial C_{\mathcal{L}_{\delta_a}}(\alpha,\beta)}{\partial\alpha}}{U_0^2\left(\frac{W_0^2}{U_0^2}+1\right)} - \frac{C_4W_0\frac{\partial C_{N_{\delta_a}}(\alpha,\beta)}{\partial\alpha}}{U_0^2\left(\frac{W_0^2}{U_0^2}+1\right)}\right) - \frac{q^2S^2bC_{Z_{\delta_e}}(\alpha)}{m}\left(\frac{C_3\frac{\partial C_{\mathcal{L}_{\delta_a}}(\alpha,\beta)}{\partial\alpha}}{U_0\left(\frac{W_0^2}{U_0^2}+1\right)} + \frac{C_4\frac{\partial C_{N_{\delta_a}}(\alpha,\beta)}{\partial\alpha}}{U_0\left(\frac{W_0^2}{U_0^2}+1\right)}\right) \\ 0 \\ \frac{q^2S^2bC_{X_{\delta_e}}(\alpha)}{m}\left(-\frac{C_4W_0\frac{\partial C_{\mathcal{L}_{\delta_a}}(\alpha,\beta)}{\partial\alpha}}{U_0^2\left(\frac{W_0^2}{U_0^2}+1\right)} - \frac{C_9W_0\frac{\partial C_{N_{\delta_a}}(\alpha,\beta)}{\partial\alpha}}{U_0^2\left(\frac{W_0^2}{U_0^2}+1\right)}\right) - \frac{q^2S^2bC_{Z_{\delta_e}}(\alpha)}{m}\left(\frac{C_4\frac{\partial C_{\mathcal{L}_{\delta_a}}(\alpha,\beta)}{\partial\alpha}}{U_0\left(\frac{W_0^2}{U_0^2}+1\right)} + \frac{C_9\frac{\partial C_{N_{\delta_a}}(\alpha,\beta)}{\partial\alpha}}{U_0\left(\frac{W_0^2}{U_0^2}+1\right)}\right) \\ 0 \\ 0 \\ 0 \end{bmatrix} \tag{10.10}$$

$$[g_{\delta_e}, g_{\delta_r}] =$$

$$\begin{bmatrix} 0 \\ 0 \\ 0 \\ \frac{q^2S^2bC_{X_{\delta_e}}(\alpha)}{m}\left(-\frac{C_3W_0\frac{\partial C_{\mathcal{L}_{\delta_r}}(\alpha,\beta)}{\partial\alpha}}{U_0^2\left(\frac{W_0^2}{U_0^2}+1\right)} - \frac{C_4W_0\frac{\partial C_{N_{\delta_r}}(\alpha,\beta)}{\partial\alpha}}{U_0^2\left(\frac{W_0^2}{U_0^2}+1\right)}\right) - \frac{q^2S^2bC_{Z_{\delta_e}}(\alpha)}{m}\left(\frac{C_3\frac{\partial C_{\mathcal{L}_{\delta_r}}(\alpha,\beta)}{\partial\alpha}}{U_0\left(\frac{W_0^2}{U_0^2}+1\right)} + \frac{C_4\frac{\partial C_{N_{\delta_r}}(\alpha,\beta)}{\partial\alpha}}{U_0\left(\frac{W_0^2}{U_0^2}+1\right)}\right) \\ 0 \\ \frac{q^2S^2bC_{X_{\delta_e}}(\alpha)}{m}\left(-\frac{C_4W_0\frac{\partial C_{\mathcal{L}_{\delta_r}}(\alpha,\beta)}{\partial\alpha}}{U_0^2\left(\frac{W_0^2}{U_0^2}+1\right)} - \frac{C_9W_0\frac{\partial C_{N_{\delta_r}}(\alpha,\beta)}{\partial\alpha}}{U_0^2\left(\frac{W_0^2}{U_0^2}+1\right)}\right) - \frac{q^2S^2bC_{Z_{\delta_e}}(\alpha)}{m}\left(\frac{C_4\frac{\partial C_{\mathcal{L}_{\delta_r}}(\alpha,\beta)}{\partial\alpha}}{U_0\left(\frac{W_0^2}{U_0^2}+1\right)} + \frac{C_9\frac{\partial C_{N_{\delta_r}}(\alpha,\beta)}{\partial\alpha}}{U_0\left(\frac{W_0^2}{U_0^2}+1\right)}\right) \\ 0 \\ 0 \\ 0 \end{bmatrix} \tag{10.11}$$

$$[g_{\delta_e}, g_{\delta_t}] = \begin{bmatrix} \frac{qSW_0X_{\delta_t}C'_{X_{\delta_e}}(\alpha)}{m^2U_0^2\left(\frac{W_0^2}{U_0^2}+1\right)} - \frac{qSZ_{\delta_t}C'_{X_{\delta_e}}(\alpha)}{m^2U_0\left(\frac{W_0^2}{U_0^2}+1\right)} \\ 0 \\ \frac{qSW_0X_{\delta_t}C'_{Z_{\delta_e}}(\alpha)}{m^2U_0^2\left(\frac{W_0^2}{U_0^2}+1\right)} - \frac{qSZ_{\delta_t}C'_{Z_{\delta_e}}(\alpha)}{m^2U_0\left(\frac{W_0^2}{U_0^2}+1\right)} \\ 0 \\ \frac{C_7qS\bar{c}W_0X_{\delta_t}C'_{M_{\delta_e}}(\alpha)}{mU_0^2\left(\frac{W_0^2}{U_0^2}+1\right)} - \frac{C_7qS\bar{c}Z_{\delta_t}C'_{M_{\delta_e}}(\alpha)}{mU_0\left(\frac{W_0^2}{U_0^2}+1\right)} \\ 0 \\ 0 \\ 0 \\ 0 \end{bmatrix} \tag{10.12}$$

$$[g_{\delta_a}, g_{\delta_r}] = \begin{bmatrix} 0 \\ \frac{q^2S^2C_{Y_{\delta_a}}(\beta)C'_{Y_{\delta_r}}(\beta)}{m^2\sqrt{U_0^2+W_0^2}} - \frac{q^2S^2C_{Y_{\delta_r}}(\beta)C'_{Y_{\delta_a}}(\beta)}{m^2\sqrt{U_0^2+W_0^2}} \\ 0 \\ \frac{q^2S^2bC_{Y_{\delta_a}}(\beta)}{m}\left(\frac{C_3\frac{\partial C_{\mathcal{L}_{\delta_r}}(\alpha,\beta)}{\partial\beta}}{\sqrt{U_0^2+W_0^2}} + \frac{C_4\frac{\partial C_{N_{\delta_r}}(\alpha,\beta)}{\partial\beta}}{\sqrt{U_0^2+W_0^2}}\right) - \frac{q^2S^2bC_{Y_{\delta_r}}(\beta)}{m}\left(\frac{C_3\frac{\partial C_{\mathcal{L}_{\delta_a}}(\alpha,\beta)}{\partial\beta}}{\sqrt{U_0^2+W_0^2}} + \frac{C_4\frac{\partial C_{N_{\delta_a}}(\alpha,\beta)}{\partial\beta}}{\sqrt{U_0^2+W_0^2}}\right) \\ 0 \\ \frac{q^2S^2bC_{Y_{\delta_a}}(\beta)}{m}\left(\frac{C_4\frac{\partial C_{\mathcal{L}_{\delta_r}}(\alpha,\beta)}{\partial\beta}}{\sqrt{U_0^2+W_0^2}} + \frac{C_9\frac{\partial C_{N_{\delta_r}}(\alpha,\beta)}{\partial\beta}}{\sqrt{U_0^2+W_0^2}}\right) - \frac{q^2S^2bC_{Y_{\delta_r}}(\beta)}{m}\left(\frac{C_4\frac{\partial C_{\mathcal{L}_{\delta_a}}(\alpha,\beta)}{\partial\beta}}{\sqrt{U_0^2+W_0^2}} + \frac{C_9\frac{\partial C_{N_{\delta_a}}(\alpha,\beta)}{\partial\beta}}{\sqrt{U_0^2+W_0^2}}\right) \\ 0 \\ 0 \\ 0 \end{bmatrix} \tag{10.13}$$

$$[g_{\delta_r}, g_{\delta_t}] = \begin{bmatrix} 0 \\ 0 \\ 0 \\ \frac{qSbX_{\delta_t}}{m}\left(\frac{C_3W_0\frac{\partial C_{\mathcal{L}_{\delta_r}}(\alpha,\beta)}{\partial\alpha}}{U_0^2\left(\frac{W_0^2}{U_0^2}+1\right)} + \frac{C_4W_0\frac{\partial C_{N_{\delta_r}}(\alpha,\beta)}{\partial\alpha}}{U_0^2\left(\frac{W_0^2}{U_0^2}+1\right)}\right) - \frac{qSbZ_{\delta_t}}{m}\left(\frac{C_3\frac{\partial C_{\mathcal{L}_{\delta_r}}(\alpha,\beta)}{\partial\alpha}}{U_0\left(\frac{W_0^2}{U_0^2}+1\right)} + \frac{C_4\frac{\partial C_{N_{\delta_r}}(\alpha,\beta)}{\partial\alpha}}{U_0\left(\frac{W_0^2}{U_0^2}+1\right)}\right) \\ 0 \\ \frac{qSbX_{\delta_t}}{m}\left(\frac{C_4W_0\frac{\partial C_{\mathcal{L}_{\delta_r}}(\alpha,\beta)}{\partial\alpha}}{U_0^2\left(\frac{W_0^2}{U_0^2}+1\right)} + \frac{C_9W_0\frac{\partial C_{N_{\delta_r}}(\alpha,\beta)}{\partial\alpha}}{U_0^2\left(\frac{W_0^2}{U_0^2}+1\right)}\right) - \frac{qSbZ_{\delta_t}}{m}\left(\frac{C_4\frac{\partial C_{\mathcal{L}_{\delta_r}}(\alpha,\beta)}{\partial\alpha}}{U_0\left(\frac{W_0^2}{U_0^2}+1\right)} + \frac{C_9\frac{\partial C_{N_{\delta_r}}(\alpha,\beta)}{\partial\alpha}}{U_0\left(\frac{W_0^2}{U_0^2}+1\right)}\right) \\ 0 \\ 0 \\ 0 \end{bmatrix} \tag{10.14}$$

$$[g_{\delta_a}, g_{\delta_t}] =$$

$$\begin{bmatrix} 0 \\ 0 \\ 0 \\ \frac{qSbX_{\delta_t}}{m}\left(\frac{C_3 W_0 \frac{\partial C_{\mathcal{L}_{\delta_a}}(\alpha,\beta)}{\partial\alpha}}{U_0^2\left(\frac{W_0^2}{U_0^2}+1\right)} + \frac{C_4 W_0 \frac{\partial C_{N_{\delta_a}}(\alpha,\beta)}{\partial\alpha}}{U_0^2\left(\frac{W_0^2}{U_0^2}+1\right)}\right) - \frac{qSbZ_{\delta_t}}{m}\left(\frac{C_3 \frac{\partial C_{\mathcal{L}_{\delta_a}}(\alpha,\beta)}{\partial\alpha}}{U_0\left(\frac{W_0^2}{U_0^2}+1\right)} + \frac{C_4 \frac{\partial C_{N_{\delta_a}}(\alpha,\beta)}{\partial\alpha}}{U_0\left(\frac{W_0^2}{U_0^2}+1\right)}\right) \\ 0 \\ \frac{qSbX_{\delta_t}}{m}\left(\frac{C_4 W_0 \frac{\partial C_{\mathcal{L}_{\delta_a}}(\alpha,\beta)}{\partial\alpha}}{U_0^2\left(\frac{W_0^2}{U_0^2}+1\right)} + \frac{C_9 W_0 \frac{\partial C_{N_{\delta_a}}(\alpha,\beta)}{\partial\alpha}}{U_0^2\left(\frac{W_0^2}{U_0^2}+1\right)}\right) - \frac{qSbZ_{\delta_t}}{m}\left(\frac{C_4 \frac{\partial C_{\mathcal{L}_{\delta_a}}(\alpha,\beta)}{\partial\alpha}}{U_0\left(\frac{W_0^2}{U_0^2}+1\right)} + \frac{C_9 \frac{\partial C_{N_{\delta_a}}(\alpha,\beta)}{\partial\alpha}}{U_0\left(\frac{W_0^2}{U_0^2}+1\right)}\right) \\ 0 \\ 0 \\ 0 \end{bmatrix} \tag{10.15}$$

Chapter 11

Adjustment of the Center of Gravity

In this appendix we will analyze how to accurately determine the center of gravity (CG from now on) of the 3D printed model. We will do it using three different weighing scales properly located and tared.

Origin and axes

In order to locate a point of our aircraft model, we need a 3D Cartesian frame of reference, that consists of a point used as the origin and the direction of the three orthogonal axes x, y and z.

Due to the symmetry of the aircraft, the center of gravity will be located in the symmetry plane of the body, and for the sake of simplicity, we will want our origin to be contained in this plane. Besides, considering where the scales will be located, it has been considered useful choosing the origin to belong to the straight line that connects the trailing edges of the wing tips. By a plane and a perpendicular line, the origin is fully defined.

We will use the conventional notation for the axes of the aircraft in the body frame of reference: x will be contained in the symmetry plane and will be parallel to the fuselage pointing to the tail, y will be parallel to the symmetry plane, in such a way that z will also be contained in the plane of symmetry pointing upwards. Note that, in order to have positive values for all the coordinates of the CG, we have inverted the sense of the axes x and z, as shown in figure 11.1.

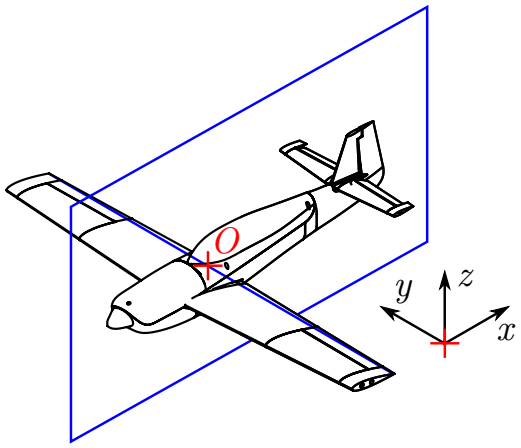

Figure 11.1: Origin and axes that will be used.

Methodology

To determine the 3 coordinates of the CG, we will need two different setups: in the first of them x_{CG} and y_{CG} will be found, while in the second one we will find z_{CG}. For each of the setups we will take up to three measurements and compute the mean in order to minimize the error we might have.

In the firs setup, the distance d_x shown in figure 11.2 will be determined by the Solid Works design of the assembly, due to the complexity of measuring only the x-component of a distance from two points that don't even belong to the same plane. Its value is $d_x = 241.4\,mm$. We will take up to 3 measurements, one at the tail (m_T) and the other two on the trailing edges of the wing tips (m_R for the right wing and m_L for the left one, as seen in figure 11.2). We will have to make sure that the aircraft is not tilted in any direction.

The values m_L and m_R are expected to be equal, due to the symmetry of the body, and if so: $y_{CG} = 0$. The value of x_{CG} will be computed as:

$$x_{CG} = \frac{m_T}{m_T + m_L + m_R}\, d_x \tag{11.1}$$

In the second phase, we will tilt the aircraft by rotating it with respect to its x-axis a certain angle α. The distance D is known to be $556\,mm$ while h is the height difference, that will be tuned in the three different measurements that will be done to improve the accuracy and the angle α will depend on the choice of h.

By the readings of m_L and m_R we will be able to figure out where the CG is, as it is the point at which the two moments cancel each other. The horizontal distance of the CG will be, from the origin we have defined in the previous section:

$$y'_{CG} = \frac{m_L}{m_L + m_R} D\cos\alpha - \frac{D}{2}\cos\alpha \tag{11.2}$$

Finally, the z-coordinate of the CG can be found by applying:

$$z_{CG} = \frac{y'_{CG}}{\sin\alpha} \tag{11.3}$$

Figure 11.2 shows the first setup while figure 11.3 depicts the second one.

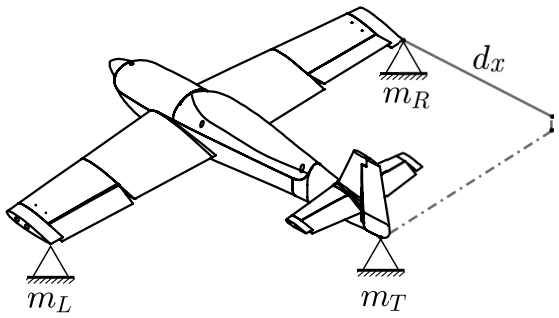

Figure 11.2: Definition of the 3 first points of support in the first setup.

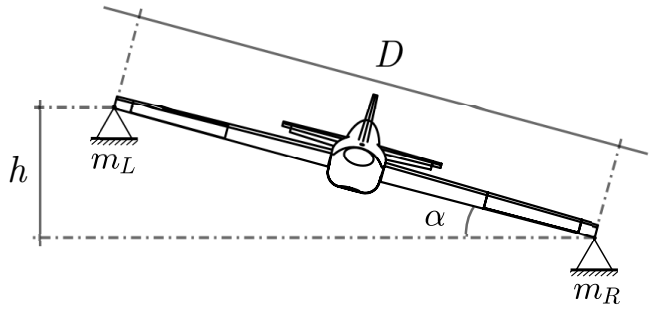

Figure 11.3: Definition of the two last points of support in the second setup.

Results

In this section we present the results of the measures in both two setups, showing in the table 11.1 the value for x_{CG} and in the table 11.2 the value of z_{CG}. As already mentioned, y_{CG} will be considered to be zero as the values of the second and third column of the first table are very similar, and symmetry is observed in the load distribution of the aircraft.

m_T (g)	m_R (g)	m_L (g)	x_{CG} (mm)
34.2	388	385.1	10.23
28.3	390	390.3	8.45
35.1	389.2	387.9	10.43
		$\bar{x}_{CG}$	**9.70**

Table 11.1: Results in the first setup.

m_r (g)	m_l (g)	h (mm)	z_{CG} (mm)
399.4	405.8	95	12.74
364.5	375.2	114	15.45
406.7	399.6	-142	9.27
		$\bar{z}_{CG}$	**12.49**

Table 11.2: Results in the second setup.

Considering the frame of reference used and the derivation of the coordinates, we can conclude that the CG of our body is located in the point $P = (9.7,\ 0,\ 12.49)$.

Chapter 12

Arduino code

In this appendix we're displaying the Arduino code that has been used to deflect the control surfaces:

```
#include <Servo.h>
String angle; //angle of deflection desired
char surface; //decide which surface to be deflected
Servo aileron, elevator, rudder;  // create servo object to control the three surfaces
double transfer; //transfer function of 4 bar mechanism TBD
boolean sign=false;
void setup() {
  Serial.begin(9600);  //clock
  aileron.attach(11);  //the pin for the aileron control
  elevator.attach(10);  //the pin for the elevator control
  rudder.attach(8);  //the pin for the rudder control
  aileron.write(0);
  elevator.write(0);
  rudder.write(0);
}
void loop(){
  if (Serial.available()) //checks if there is an input
  {
    char c = Serial.read();  //gets one byte from serial buffer
    if (c == '-'){
      sign=true;
    }
    else if (isDigit(c) || c== '.')
    {
      angle+=c;
    }
    else if(c==',')
    {
      double deflection = angle.toDouble();  //convert angle into a number (check)
      if(sign){
        deflection*=-1;
        sign=false;
      }
      transfer=2*sin(radians(deflection));
      double n= (asin(transfer)*57296) / 1000;      //the input angle to the servo is equal to the desired output deflection divided by the transfer function
      n+=90;
      if(surface=='a'){
        aileron.write(n);
      }
      if(surface=='e') {
        elevator.write(n);
      }
      if(surface=='r') rudder.write(n);
      angle="";
    }
    else
    {
     surface=c;
     Serial.println(surface);
    }
   }
}
```

Listing 12.1: Arduino code for the aileron and elevator deflections.

Chapter 13

LabView software

In this appendix, we are going to expalin how the data was gathered by the visual tool LabView. This software program, from National Instruments, is specially useful in the real-time processing of signals obtained from electronic devices like sensors. It is a visual tool and, thus, doesn't use any written code but rather block diagrams with the corresponding connections and operations.

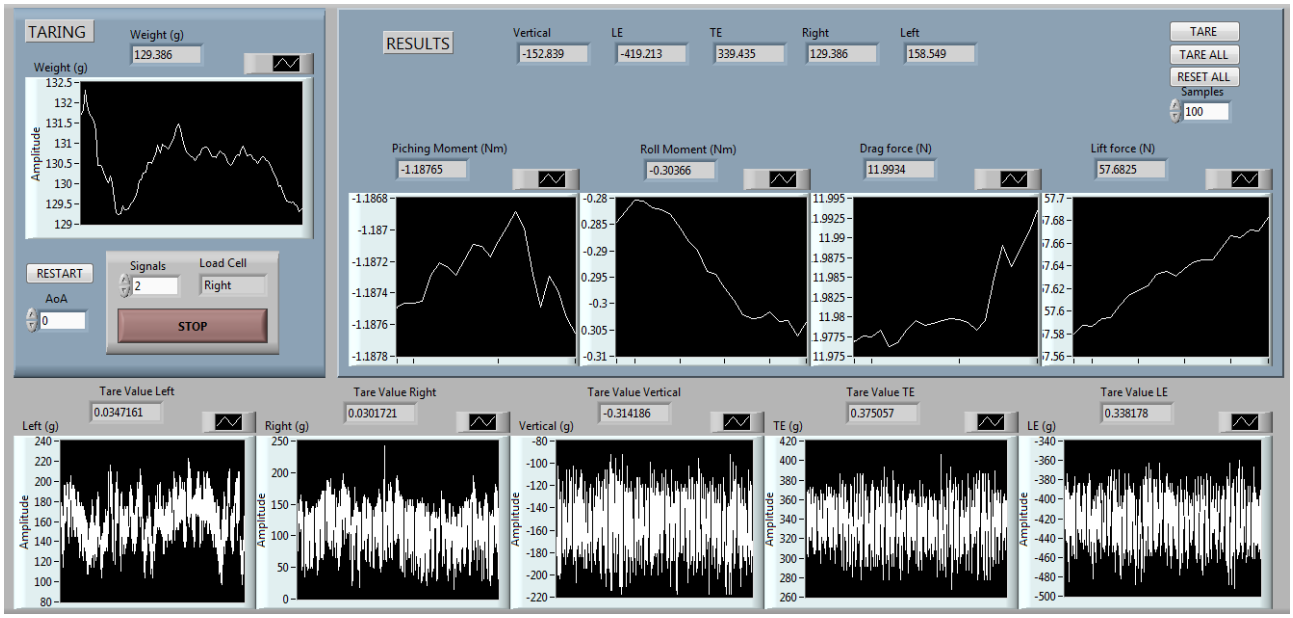

Figure 13.1: LabView software screenshot

Figure 13.1 shows a screenshot of the visual interface that was used in the data acquisition. In this section, we will comment on the different widgets that are shown and how it works.

Taring

The taring can be done to all the 5 load cells at the same time or one by one. In case it is required one by one, the load cell can be selected in the input window labeled as *Signals*. A message box on the right displays the name of the LC we are taring (*Left*, *Right*, *Vertical*, *LE* and *TE*). To tare the load cell in question, the button *TARE* in the upper right corner must be pressed. The button *RESTART*, next to the channel selector restarts the average that is performed to find the taring values.

In case all the load cells must be tared at the same time, the button *TARE ALL* will have to be pressed. The button *RESET ALL* resets all the load cell taring values to 0. The taring values of each load cell are shown above each of the graph charts below, that show the real-time unfiltered readings for the 5 load cells.

Default values are already set for each of the load cells, in order for the procedure not to be repeated each time the load cell system is used. Those values for the taring were obtained without the aircraft being over the mount and were obtained after a long time window, in order to obtain accurate values and minimize the error.

Results

The results are shown in the upper left blue box. The five numeric indicators show the real-time averaged forces that are measured at each load cell in grams. After about 10-15 seconds they converge to a certain value. Those are the values that are gathered in Excel sheets to later be analyzed.

Besides, four additional graph charts show the real-time value of all moments (pitching and rolling) and forces (drag and lift) in N·m and N respectively. They also need as input the angle of attack, that is manually introduced in the numeric control below the *RESTART* button. This is only a reference indicator to see if results will make sense, but hasn't been used actually, as it is considered better having the raw data.

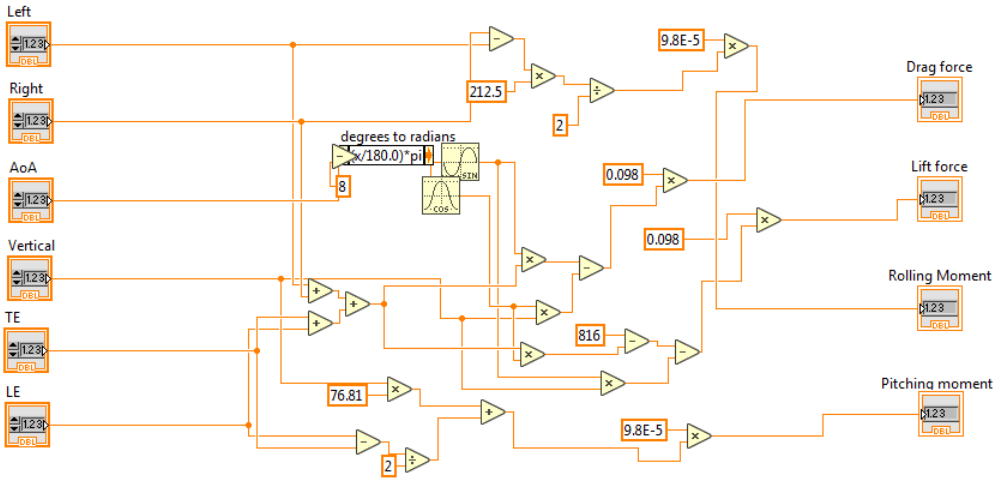

Figure 13.2: Block diagram of the SubVI that computes the forces and moments.

The block diagram that is behind this user interface has been developed following a modular philosophy, in the sense that some operations that had to be done more than one time, like averaging, were defined as blocks, or in the language of LabView, SubVI's. Figure 13.2 shows an example of the block diagram of a SubVI, in this case, the one that computes the forces and moments taking as inputs the four force measurements and the AoA.

Chapter 14

Vibrational stability: Kapitza's pendulum

Introduction to averaging theory

Consider a system whose dynamics satisfy the system of ordinary differential equations that follows:

$$\dot{x} = \varepsilon f(t,\, x,\, \varepsilon), \tag{14.1}$$

being f a T-periodic function in time, and for ε small. We can define the averaged dynamics of the system $\dot{\bar{x}} = \varepsilon \bar{f}(\bar{x})$, where:

$$\bar{f} = \frac{1}{T}\int_0^T f(t,\, x,\, 0)\,\mathrm{dt} \tag{14.2}$$

and the two following conditions hold:

1. If the difference of the initial state with respect to the averaged one is of order ε, there exist two positive-valued constants b and ε^* such that the difference of the state with its averaged value remains of the same order for all time less or equal b/ε and for all ε less or equal ε^*. In mathematical notation, if $x(0) - \bar{x}(0) = \mathcal{O}(\varepsilon)$ then $\exists\, b > 0 \,\&\, \varepsilon^* > 0$ s.t. $x(t) - \bar{x}(t) = \mathcal{O}(\varepsilon)\ \forall t \in \left[0,\, \frac{b}{\varepsilon}\right],\ \forall \varepsilon \in [0,\, \varepsilon^*]$.
2. Being $\bar{x}_0$ an exponentially stable equilibrium point of the averaged dynamics of eq. 14.1 and if $x(0) - \bar{x}(0) = \mathcal{O}(\varepsilon)$, then $\exists\, \varepsilon^*$ s.t. $x(t) - \bar{x}(t) = \mathcal{O}(\varepsilon)\, \forall t,\ \forall \varepsilon \in [0, \varepsilon^*]$. Moreover, the system defined in eq. 14.1 has a unique exponentially stable solution x_T with $\|x_T(t) - \bar{x}_0\| \leq k \cdot \varepsilon$ for some k.

Motion of the Kapitza's pendulum

The governing equation of motion of a pendulum whose support is oscillating in the vertical axis as $y = a \cdot \cos \omega\, t$ is:

$$\ddot{\theta} = \left(\frac{g}{l} + \frac{a\,\omega^2}{l}\cos \omega t\right) \sin \theta, \tag{14.3}$$

where, as figure 14.1 suggests, l is the length of the pendulum, a is the amplitude of the oscillations, and θ is the angle of the pendulum with respect to the vertical axis. Besides, g is the gravity, that points downwards.

The resonant frequency of the pendulum will be $\omega_0 = \sqrt{g/l}$. We will define the parameter ε to be the ratio between the amplitude of the oscillations and the length of the pendulum $\varepsilon \triangleq a/l$ with $\varepsilon \ll 1$. The frequency of the oscillations ω should be much greater than ω_0, and so, the ratio ω_0/ω should be proportional to ε:

$$\frac{\omega_0}{\omega} = \delta \cdot \varepsilon \tag{14.4}$$

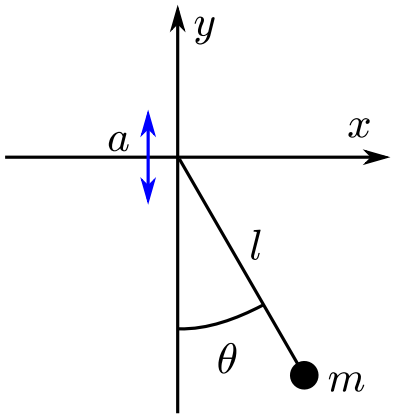

Figure 14.1: Scheme of the Kapitza's pendulum.

for some δ. By substituting in eq. 14.3, we reach:

$$\ddot{\theta} = \omega^2 \left(\frac{g/l}{\omega^2} + \varepsilon \cos \omega t \right) \sin \theta = \omega^2 \left(\delta^2 \varepsilon^2 + \varepsilon \cos \omega t \right) \sin \theta \tag{14.5}$$

In order to be able to apply the averaging theory in the study of the Kapitza's pendulum, we need to arrive at a expression of the form $\dot{x} = \varepsilon f(t, x, \varepsilon)$. To do so, we apply a change of variable, by introducing:

$$\tau = \omega\, t \qquad \rightarrow \frac{d}{dt} = \frac{d}{d\tau} \omega \tag{14.6}$$

And so, eq. 14.5 will be:

$$\frac{d^2\theta}{d\tau^2} = \delta^2 \varepsilon^2 \sin \theta + \varepsilon \cos \tau \sin \theta \tag{14.7}$$

In the state-space representation, by choosing the two states to be $x_1 = \theta$ and $x_2 = \frac{1}{\varepsilon}\theta' - \sin\tau \cdot \sin\theta$, where θ' is the τ-derivative of θ, we would have, as derivatives with respect of τ:

$$\begin{cases} x_1' = \theta' = \varepsilon \left(x_2 + \sin \tau \sin x_1 \right) \\ x_2' = \frac{1}{\varepsilon} \theta'' - \cos\tau \sin\theta - \sin\tau \cos\theta \varepsilon \left(x_2 + \sin\tau \sin x_1 \right) = \varepsilon \left(\delta^2 \sin\theta - \sin\tau \cos\theta x_2 - \sin^2 \tau \cos\theta \sin\theta \right) \end{cases} \tag{14.8}$$

Now, by averaging with respect to τ, we have:

$$\begin{cases} \bar{x}_1' = \varepsilon\, x_2 \\ \bar{x}_2' = \varepsilon \left(\delta^2 \sin x_1 - \dfrac{\cos x_1 \sin x_1}{2} \right) \end{cases} \tag{14.9}$$

Finally, considering $\theta \simeq 0$, and making the approximations $\sin\theta \simeq \theta$ in rad and $\cos\theta \simeq 1$ we linearize and have:

$$\frac{d}{d\tau} \begin{pmatrix} \bar{x}_1 \\ \bar{x}_2 \end{pmatrix} \simeq \varepsilon \begin{pmatrix} x_2 \\ \delta^2\, x_1 - \dfrac{x_1}{2} \end{pmatrix} = \varepsilon \begin{bmatrix} 0 & 1 \\ \delta^2 - \dfrac{1}{2} & 0 \end{bmatrix} \cdot \begin{pmatrix} x_1 \\ x_2 \end{pmatrix} \tag{14.10}$$

For stability, the term $\delta^2 - \frac{1}{2}$ has to be negative, and so, the frequency ω must fulfill $\omega \geq \sqrt{2\,g\,l}/a$.

Design and setup

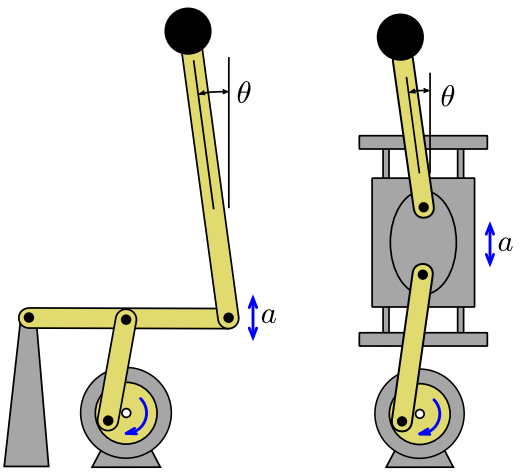

(a) Traditional design (b) New design

Figure 14.2: Kapitza pendulum designs.

The traditional design of the Kapitza's pendulum, shown in fig. 14.2 (a), consists of a fixed motor that transmits its oscillations to the center of a metallic bar that is fixed to one end and holds the pendulum at the other. It is simple to assemble, but strictly speaking, the oscillations of the center of the pendulum are not vertical: they follow the arc of a circumference.

Our approach uses fixed rails instead. By these rails a slider oscillates vertically powered by the motor and holding the pendulum at the same time, see fig. 14.2 (b).

In our study, we wish to compare the response of the pendulum with the frequency varying three of the parameters: the pendulums length l, the amplitude of the oscillations a and the mass m. A total of four different pendula will be manufactured: a reference one and one for each parameter that will be modified.

While for the first two parameters we are expecting the cutoff frequency to differ, in the third of them, that has a different mass, no change is expected with respect to the reference pendulum.

Table 14.1 shows the different parameters chosen for each pendulum. In the reference pendulum the mass consists of two penny coins that have a total mass of 5g, while in the pendulum with different mass two dimes have been used instead, with a total mass of 10g. The crank radius corresponds to the amplitude of the oscillations a and the cutoff frequency is computed as $\omega = \sqrt{2\,g\,l}/a$. Note that, as expected, the cutoff frequency is the same for the two first pendulums.

Pendulum	**Mass** (g)	**Length** (mm)	**Crank radius** (mm)	**Cutoff frequency** $(rad \cdot s^{-1})$
Reference	5	50	10	99
Different mass	10	50	10	99
Different amplitude	5	50	15	66
Different length	5	75	10	121

Table 14.1: Parameters for the different pendulums.

Finally, figure 14.3 shows a scheme of the setup that we will use. Each pendulum will be fed by its motor, whose frequency will be controlled independently by potentiometers. Finally 14.4 shows a photo of the manufactured pendulum set.

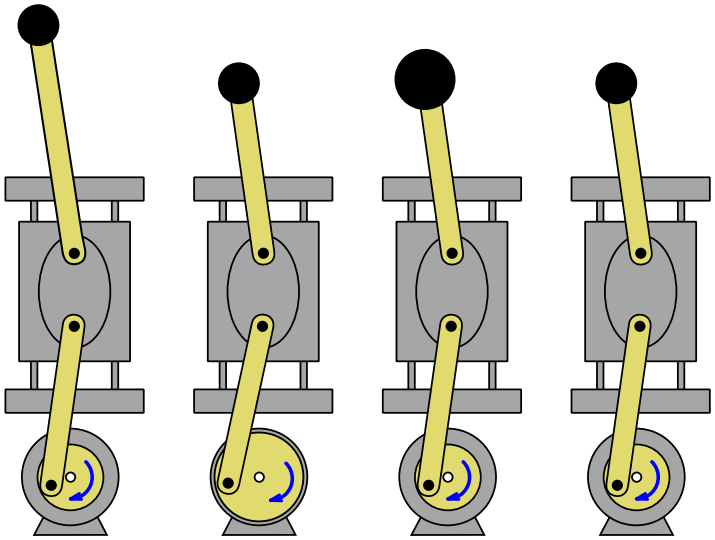

(a) $\neq$ length (b) $\neq$ amplitude (c) $\neq$ mass (d) Reference

Figure 14.3: Experimental setup scheme as assembled.

Figure 14.4: Manufactured Kapitza pendulum set.